

Sanjaya Dhonju Shrestha

Numerical Modelling of Hydraulics and Sediment at the Headworks of Kali Gandaki A Hydropower Plant, Nepal

Master's thesis in Hydropower Development

Supervisor: Nils R ther

July 2020

Sanjaya Dhonju Shrestha

Numerical Modelling of Hydraulics and Sediment at the Headworks of Kali Gandaki A Hydropower Plant, Nepal

Master's thesis in Hydropower Development
Supervisor: Nils R  ther
July 2020

Norwegian University of Science and Technology
Faculty of Engineering
Department of Civil and Environmental Engineering



Abstract

The Kali Gandaki A Hydropower Plant (KGA) has been facing issues related to unfavourable flow conditions at intake and settling basins, thereby hindering the efficient settling of the sediments, as realized from the excessive sediment-induced turbine erosion. With an intention to counteract these issues, investigations were conducted in a physical hydraulic model that recommended design modifications to the existing headworks arrangements based on improved hydraulic performance and qualitative evaluation of flushing efficiency. However, the performance of the settling basins with the modified geometry in relation to suspended sediments is still unresolved. Hence, the present study aims to assess the same, by utilizing the numerical model in SSIIM 1, including sediment concentration distribution and bed deposition pattern.

A 3D numerical model with structured and non-orthogonal grid was used for the simulation. The numerical model (scale of 1:40; as adopted for physical hydraulic model) was first calibrated against the measured velocities at intake and settling basins in the physical hydraulic model. The porosity approach was used to represent the effect of the wire mesh used in physical hydraulic model (representing trash rack in the prototype). The simulations were also tested for two grid resolutions (coarse and fine) and two discretization schemes (Power-Law (POW) scheme and Second Order Upwind (SOU) scheme). The fine grid resolution with porosity of 0.55 and POW scheme produced the best conformity (among the trials made) with the measurements, and hence was opted for the sediment simulation in prototype scale (1:1), obtained by scaling up the geometry of the calibrated numerical model.

Sediment simulation involved four size fractions and was carried out for two different scenarios: without and with bed changes. The former utilized the results from the hydraulic simulation while the latter used the flow field recomputed after the update of the bed. Sensitivity analysis was also considered for different fall velocities corresponding to two different water temperatures (20 °C and 10 °C). The trap efficiencies estimated from the simulations were also compared with those estimated from the analytical methods.

The sensitivity test showed that the reduction in fall velocities (water temperature at 10 °C) mainly influence the trap efficiency for the finer size fractions. Besides, the rate of decrease in sediment concentration and magnitude of the deposits are also reduced. Nevertheless, the trend of reduction in sediment concentration and bed deposition pattern appears similar to the observations made with higher fall velocities (water temperature at 20 °C).

Significant improvement in the trap efficiency of the settling basins is observed with the recommended modifications in comparison to the trap efficiency of the existing structure measured in recent years. The smallest value for overall trap efficiency observed among all the simulations is 60%, which is 19% higher compared to that measured in 2018. However, the simulation time was limited to a single day, and hence the value is expected to decrease with an extended simulation time. Similarly, the simplifications adopted in the geometry, errors due to numerical approximations, possible bugs, inaccuracy of empirical formula for sediment concentration, errors due to not complete convergence in time-dependent computation, etc. further add uncertainties to the results.

Preface

This thesis is a part of my Master's Degree in Hydropower Development at the Department of Civil and Environmental Engineering, Norwegian University of Science and Technology (NTNU). It contains the works carried out from January 2020 to July 2020 under the supervision of Prof. Nils R  ther and co-supervisors Diwash Lal Maskey and Siri Stokseth.

The study attempts to investigate the performance of the settling basins with proposed modifications to the existing headworks at Kali Gandaki A Hydropower Plant (KGA) in terms of suspended sediments by the application of numerical modelling using SSIIM 1. The data required for the study, including photos and videos during physical hydraulic modelling are obtained from Hydro Lab, Nepal. And the field data on sediments are attained from the site office of KGA during the visit to Nepal (June-August, 2019).

I would like to express my sincere gratitude to Prof. Nils R  ther for his great supervision and advice. I am highly indebted to my co-supervisor, Diwash Lal Maskey for his consistent guidance, continuous backing and encouragement throughout the working period especially on using the software.

My gratitude also extends to Norwegian Agency for development Cooperation (NORAD) for providing financial support to pursue my studies at NTNU.

Similarly, I am thankful to Dr. Meg Bahadur Bishwakarma and Dr. Umesh Singh from Hydro Lab. Special thanks to Sanat Kumar Karmacharya for providing a detailed overview of the physical hydraulic model despite his busy schedule.

I would also like to appreciate the support from Sudeep Neupane, Site Engineer at KGA for providing valuable data on sediments and unhesitant responses to the queries regarding the working condition of the plant.

Finally, I wish to thank my friend Nitish Sapkota for assisting me while working with the software when problems were encountered.

Sanjaya Dhonju Shrestha
Trondheim, July 2020

Dedication

This thesis is dedicated to

My son, *Sakhaa*

My sisters, *Sapana* and *Sarita*

My wife, *Niru*

&

My teachers and friends

Contents

Abstract	iii
Preface	v
Dedication	vii
Contents	ix
List of Figures	xiii
List of Tables	xvii
List of Acronyms	xix
List of Symbols and Units	xxi
1 Introduction	1
1.1 Background	1
1.2 Master's Thesis Work	2
1.3 Thesis Structure	2
2 Theory	3
2.1 Sediment Transport	3
2.1.1 Initiation of Motion	3
2.1.2 Particles in Motion	5
2.2 Sediment Handling in Run-of-River Hydropower Plant	6
2.3 Problems due to Sediments	6
2.4 General Layout of Headworks in ROR Hydropower Plants	7
2.5 Strategies for Sediment Handling	7
2.5.1 Intake Location	7
2.5.2 Flow Modification in Front of the Intake	8
2.5.3 Sustaining Peaking Storage	9
2.5.4 Removal of Suspended Sediments from Diverted Water	10
2.5.5 Monitoring and Sediment-Guided Operation	10
2.6 Design of Settling Basin	10
2.6.1 Particle Size to be Excluded	11
2.6.2 Critical Flow Velocity	11
2.6.3 Fall Velocity	11
2.6.4 Trap Efficiency Computation	12
2.6.5 Design Concept of Ideal Basin	15
2.6.6 Real Settling Basin	16
2.6.7 Data Requirements	18
2.6.8 Potential Hydraulic Problems in Settling Basin	19
2.6.9 Sediment Flushing	20
3 Model Studies	21
3.1 Physical Model	21
3.1.1 Basic Principle	21
3.1.2 Model Laws	22
3.1.3 Disadvantages of Physical Model	23
3.2 Numerical Model	23
3.2.1 Grids	24

3.2.2	Spatial Discretization	25
3.2.3	Discretization Schemes	26
3.2.4	Temporal Discretization	27
3.3	Numerical Modelling of Hydraulics	28
3.3.1	Navier-Stokes Equations	28
3.3.2	Turbulence Model	28
3.3.3	The SIMPLE Method	31
3.3.4	Free Surface Algorithms	32
3.3.5	Boundary Conditions	33
3.4	Numerical Modelling of Sediment Transport	34
3.4.1	Bed Load	34
3.4.2	Suspended Load	35
3.4.3	Non-uniform Sediments	35
3.5	Errors and Uncertainties in CFD	36
3.6	Significance of Model Studies in Headworks	36
3.7	Relevant Works	37
4	Kali Gandaki A Hydropower Plant	38
4.1	Introduction	38
4.2	Arrangement of Headworks	39
4.3	Hydrology and Sedimentology	39
4.4	Problems in Existing Headworks	41
4.5	Physical Hydraulic Model Study and Recommendations	42
4.6	Need for Numerical Modelling	44
5	SSIIM	46
5.1	Introduction	46
5.2	Input/Output Files	47
5.3	Theoretical Basis	48
5.3.1	Water Flow Computation	48
5.3.2	Sediment Transport Computation	48
5.4	Limitations	49
6	Hydraulics Simulation	50
6.1	Simulation Case	50
6.2	Simplifications	50
6.3	Grid Generation	51
6.3.1	Defining Components, Inlet and Outlet in SSIIM Model	53
6.4	Model Scale Simulation and Calibration	54
6.4.1	Input Data	54
6.4.2	Input Files	54
6.4.3	Use of the <i>Porosity</i> File	55
6.4.4	Calibration Data	55
6.4.5	Progress and Results	56
6.5	Prototype Scale Simulation	60
6.5.1	Input Data	60
6.5.2	Input Files	60
6.5.3	Results	60
6.6	Problem Encountered	66
7	Sediment Simulation	67
7.1	Input Data	67
7.2	Input Files	68
7.3	Results	68
7.3.1	Simulation without Bed Changes	68

7.3.2	Simulation with Bed Level Changes	70
7.4	Sensitivity Analysis	72
7.4.1	Results	73
7.5	Comparison with Analytical Method	73
7.6	Problem Encountered	73
8	Discussion	75
8.1	Model Scale Simulation	75
8.2	Prototype Scale Simulation	76
8.3	Performance Evaluation	77
9	Conclusion	79
10	Future Works	80
	Bibliography	82
A	Salient Features	85
B	Drawings and SSIIM Model	87
C	Detailed Calculation for Trap Efficiency	93
D	SSIIM Files	98
E	Additional Figures	108
F	Agreement	113

List of Figures

2.1	Forces acting on a particle in a stream	3
2.2	Shields graph for incipient motion	4
2.3	Vertical distribution of sediment concentration for selected values of z	5
2.4	Typical arrangement of principle components of ROR headworks relevant to sediment management.	7
2.5	Section A-A (corresponding to Figure 2.6) showing rotational flow.	8
2.6	Suitability for intake location on idealized schematic river meanders.	8
2.7	Arrangement for off-stream pondage.	9
2.8	Fall velocity of quartz spheres in water and air.	12
2.9	Trap efficiency as a function of λ	13
2.10	Camps diagram for trap efficiency including the effect of turbulence on the fall velocity.	14
2.11	Sumer's relation between λ and β	14
2.12	Variation of k and η_0 with w/u_*	15
2.13	Ideal settling basin.	16
2.14	Schematic illustration of of a typical elongated settling basin; α and β refer to the horizontal and vertical angles of expansions, respectively.	17
2.15	Transition zone with guide walls.	18
2.16	Undesirable hydraulic geometry observed in settling basins.	19
3.1	A typical control volume in Cartesian 2D grid.	26
4.1	Existing headworks of KGA during wet season operation.	38
4.2	Physical hydraulic model of existing headworks.	39
4.3	Discharge and sediment concentration for different years.	40
4.4	Problems in existing headworks at KGA.	41
4.5	Trap efficiencies of existing settling basins in different years, derived from observed sediment concentrations at inlet and outlet of settling basins.	42
4.6	Erosion in runner and facing plates.	42
4.7	Physical hydraulic model with recommended design modifications.	44
6.1	(a) Flow pattern in forebay for $1,200\text{ m}^3/\text{s}$ discharge in the river, with almost no dispersion of dye towards the pool, (b) Schematic representation of the vertical wall considered in numerical model to exclude the pool.	51
6.2	Plan view of simplified geometry (black) considered for numerical simulation laid over the actual geometry with recommended design modifications (light grey) including river portion.	52
6.3	Geodata points for the river portion.	53
6.4	Plan view of grid used in simulation (model scale, coarse grid resolution).	53
6.5	Simulated flow field (top view) with POW scheme; (a) coarse grid resolution and (b) fine grid resolution, (model scale).	56
6.6	Longitudinal profiles with velocity vectors along Bay 1 for simulation with POW scheme; (a) coarse grid resolution and (b) fine grid resolution, (model scale).	57

6.7	Measured and computed velocities at intake in different bays for simulation with POW scheme and different grid resolutions, (model scale).	57
6.8	Vertical profiles of measured and computed velocities in streamwise direction, U_x in settling basins for simulation with POW scheme and different grid resolutions, (model scale).	58
6.9	Longitudinal profiles of measured and computed velocities in streamwise direction, U_x in settling basins at different levels for simulation with POW scheme and different grid resolutions, (model scale).	59
6.10	Simulated flow field (top view) with POW scheme and fine grid resolution, (prototype scale).	61
6.11	Velocity distribution at intake across cross-section (downstream view, prototype scale).	61
6.12	Velocity distribution in different cross-sections (downstream view, prototype scale).	62
6.13	Longitudinal profiles with velocity vectors along each bay for simulation with POW scheme and fine grid resolution, (prototype scale).	62
6.14	Simulated bed shear stress distribution with POW scheme and fine grid resolution, (prototype scale).	63
6.15	Vertical profiles of measured (upscaled) and computed velocities in streamwise direction, U_x in settling basins for simulation with POW scheme and fine grid resolution, (prototype scale).	64
6.16	Longitudinal profiles of measured (upscaled) and computed velocities in streamwise direction, U_x in settling basins at different levels for simulation with POW scheme and fine grid resolution, (prototype scale).	65
6.17	Plan view of grid used in initial simulation (model scale, coarse grid resolution) with different orientation.	66
7.1	Trap efficiencies for each size fraction with respect to the time of computation for simulation without bed changes and water temperature at 20 °C.	69
7.2	Computed depth-averaged concentration for each size fraction along the mid-way of each bay from intake to basin outlet for water temperature at 20 °C.	69
7.3	Computed sum of depth-averaged concentration along the mid-way of each bay from intake to basin outlet for water temperature at 20 °C.	70
7.4	Trap efficiencies for each size fraction with respect to the time of computation for simulation with bed changes and water temperature at 20 °C.	71
7.5	Computed bed level changes along the mid-way in each bay at an interval of 6 hours for simulation with water temperature at 20 °C.	72
7.6	Comparison of trap efficiencies for different particle sizes estimated using different analytical approaches and from simulation, with water temperature at (a) 20 °C and (b) 10 °C.	74
8.1	Comparison of overall trap efficiency estimated from simulation with measured trap efficiency.	77
B.1	Plan view of the recommended modifications by Hydro Lab with measurement points and sections.	88
B.2	Longitudinal section A-A, corresponding to Figure B.1; (a) in prototype with modifications and (b) in SSIIM model.	89
B.3	Longitudinal section B-B, corresponding to Figure B.1; (a) in prototype with modifications and (b) in SSIIM model	90
B.4	Cross-section at SB3, corresponding to Figure B.1; (a) in prototype with modifications and (b) in SSIIM model.	91

B.5	Plan views of SSIIM model at different levels; (a) level 2 showing forebay wall, divide wall and guide walls, (b) level 4 showing the portion of guide walls protruding above 508.00 <i>masl</i> and (c) level 10 showing the piers over forebay wall	92
E.1	Longitudinal profiles with velocity vectors along different bays for simulation with POW scheme and different grid resolutions, (model scale).	108
E.2	Simulated flow field with POW scheme and fine grid resolution, (prototype scale) showing outlets at spillway and settling basin.	109
E.3	Trap efficiencies for each size fraction with respect to the time of computation for simulation without bed changes and water temperature at 10°C.	109
E.4	Trap efficiencies for each size fraction with respect to the time of computation for simulation with bed changes and water temperature at 10°C.	110
E.5	Computed depth-averaged concentration for each size fraction along the mid-way of each bay from intake to basin outlet for water temperature at 10°C.	110
E.6	Computed sum of depth-averaged concentration along the mid-way of each bay from intake to basin outlet for water temperature at 10°C.	111
E.7	Computed bed level changes along the mid-way in each bay at an interval of 6 <i>hours</i> for simulation with water temperature at 10°C.	112

List of Tables

2.1	Operational regimes characteristics of ROR plants.	6
3.1	Scale ratios based on Froude law.	23
4.1	Particle size distribution of suspended sediments.	40
4.2	Model scale ratios used in physical hydraulic model of KGA.	43
4.3	Simulated flows in physical hydraulic model.	43
4.4	Trap efficiencies estimated using different analytical approaches for water temperature at 20 °C.	44
6.1	Gate operating conditions for 1,200 m ³ /s.	50
7.1	Sediment parameters used for simulation.	68
A.1	Salient Features of KGA.	85
C.1	Input parameters for calculation of trap efficiency of settling basin.	93
C.2	Trap efficiency computation by Hazen’s method, (20 °C).	93
C.3	Trap efficiency computation by Velikanov’s method, (20 °C).	94
C.4	Trap efficiency computation by Camp’s method, (20 °C).	94
C.5	Trap efficiency computation by Vetter’s method, (20 °C).	94
C.6	Trap efficiency computation by Sumer’s method, (20 °C).	94
C.7	Trap efficiency computation by Garde et al. method, (20 °C).	94
C.8	Trap efficiency computation by Raju et al. method, (20 °C).	95
C.9	Trap efficiencies estimated using different analytical approaches for water temperature at 10 °C.	95
C.10	Trap efficiency computation by Hazen’s method, (10 °C).	95
C.11	Trap efficiency computation by Velikanov’s method, (10 °C).	96
C.12	Trap efficiency computation by Camp’s method, (10 °C).	96
C.13	Trap efficiency computation by Vetter’s method, (10 °C).	96
C.14	Trap efficiency computation by Sumer’s method, (10 °C).	96
C.15	Trap efficiency computation by Garde et al. method, (10 °C).	96
C.16	Trap efficiency computation by Raju et al. method, (10 °C).	97

List of Acronyms

1D	One-dimensional.
2D	Two-dimensional.
3D	Three-dimensional.
ADV	Acoustic Doppler Velocimeter.
ASM	Algebraic Stress Model.
c/c	centre to centre.
CFD	Computational Fluid Dynamics.
CFL	Courant-Friedrich-Lewy.
DNS	Direct Numerical Simulation.
ERCOTAC	European Research Community on Flow, Turbulence and Combustion.
FOU	First Order Upwind.
KGA	Kali Gandaki A Hydropower Plant.
LES	Large Eddy Simulation.
NEA	Nepal Electricity Authority.
POW	Power-Law.
PSD	Particle Size Distribution.
QUICK	Quadratic Upwind Interpolation for Convective Kinetics.
RANS	Reynolds-averaged Navier-Stokes.
ROR	Run-of-River.
RSM	Reynolds Stress Model.
SIMPLE	Semi-Implicit Method for Pressure Linked Equations.
SOU	Second Order Upwind.
SSIIM	Sediment Simulation In Intakes with Multiblock option.
TSC	Transient Sediment Computation.
USBR	United States Bureau of Reclamation.
VOF	Volume of Fluid.

List of Symbols and Units

Symbols

α	Bed sloping angle [$^{\circ}$]
α	Horizontal expansion angle [$^{\circ}$]
β	Vertical expansion angle [$^{\circ}$]
ΔQ	Continuity defect [m^3/s]
Δt	Time-step [s]
Δx	Cell size [m]
Δz	Change in water level [m]
Δ	Bed form height [m]
δ_{ij}	Kronecker delta [—]
η	Trap efficiency [—, %]
η_0	Limiting efficiency [%]
Γ	Diffusion coefficient [m^2/s]
γ	Specific of water [kN/m^3]
γ_s	Specific weight of sediment [kN/m^3]
κ	von Kármán constant [—]
λ	Bed form length [m]
λ_e	Linear interpolation factor [—]
μ	Dynamic viscosity of water [Ns/m^2]
ν	Kinematic viscosity of water [m^2/s]
ν_T	Turbulent or Eddy viscosity [m^2/s]
ω	Turbulence frequency [$1/s$]
ϕ	Face value of the general property
ρ or ρ_w	Density of water [kg/m^3]
ρ_s	Density of sediment [kg/m^3]
σ	Courant number [—]
τ	Bed shear stress [N/m^2]
τ^*	Shield's parameter [—]
τ_c	Critical shear stress [N/m^2]
ε	Dissipation rate [m^2/s^3]
ξ	Parameter to modify Shield's parameter in hiding/exposure formula [—]
A	Cross-sectional area [m^2]

List of Symbols and Units

a	Reference level for reference concentration c_a [m]
a	Reference level in van Rijn's formula [m]
A_k	Cell surface area in direction k [m^2]
A_s	Basin area [m^2]
A_z	Horizontal projected area [m^2]
B	Width of the basin [m]
b	Width of the approach channel [m]
c or C	Sediment concentration [ppm , kg/m^3 , m^3/m^3]
c_a	Reference concentration [ppm , kg/m^3 , m^3/m^3]
C_D	Drag coefficient [–]
C_L	Lift coefficient [–]
C_p	Camp number [–]
c_{bed}	Concentration of suspended load at bed [ppm , kg/m^3 , –]
d	Particle size [m]
d_{50}	Average sediment particle diameter [m]
d_{90}	particle diameter corresponding to 90% cumulative percentile [m]
d_{cr}	Limit particle size [mm]
F	Flux [kg/s]
F	Force [N]
F	Volume fraction occupied by water [–]
f	Reduction factor [–]
Fr	Froude number [–]
g	Acceleration due to gravity [m/s^2]
h	Flow depth in the approach channel [m]
h or D	Flow depth [m]
I	Hydraulic gradient [–]
k	Turbulent kinetic energy [m^2/s^2]
k_s	Roughness height [m]
L	Distance to the water surface [m]
L	Length of the basin [m]
L	Length scale [m]
l_m	Mixing length [m]
M	Manning-Stricklers roughness coefficient [$m^{1/3}/s$]
m	Mass [kg]
n	Manning's roughness coefficient [$s/m^{1/3}$]
P	Pressure [N/m^2]
P	Wetted perimeter [m]
P_k	Production of turbulence [m^2/s^3]
Pe	Peclet number [–]

Q	Discharge [m^3/s]
q_b or q_s	Sediment transport rate per unit width [$kg/s/m$]
R	Hydraulic radius [m]
R^*	Particle Reynolds number [—]
Re	Reynolds number [—]
Sc	Schmidt number [—]
t	Time [s]
T_r	Retention time [s]
T_s	Settling time [s]
U	Velocity [m/s]
$u(t)$	Fluctuating velocity [m/s]
U^t	Instantaneous velocity [m/s]
u_*	Shear velocity [m/s]
U_{cr}	Critical velocity [m/s]
V	Volume [m^3]
w	Fall velocity [m/s]
x, y, z	Spatial variables [m]
y	Distance from wall to cell centre [m]
y	Vertical distance above the bed [m]
z	Rouse number [—]
z	Water surface elevation [m]

Subscripts and Superscripts

'	Index for corrected variables
*	Index for uncorrected variables
a	Air
b	Bottom
D	Drag
$E W N S$	Cardinal directions; East, West, North and South, respectively
$e w n s$	Cardinal directions; East, West, North and South, respectively
G	Gravity
i	Arbitrary index number
$i j k$	Nodal point indexes
L	Lift
m	Model
p	Prototype
R	Frictional resistance
r	Model-to-prototype ratio
s	Sediment

List of Tables

<i>t</i>	Top
<i>w</i>	Water
<i>c</i> or <i>c_{cr}</i>	Critical
<i>in</i>	Inlet
<i>n+1</i>	New time level
<i>n</i>	Current time level
<i>out</i>	Outlet

Units

$^{\circ}\text{C}$	Degree Celcius
$^{\circ}$	Degree
<i>GWh</i>	Gigawatt hour
<i>Hz</i>	Hertz
kg/m^3	Kilogram per cubic meter
kg/s	Kilogram per second
<i>km</i>	Kilometer
<i>kV</i>	Kilovolt
<i>m</i>	Meter
m/s	Meter per second
m/s^2	Meter per square second
m^2	Square meter
m^3/s	Cubic meter per second
<i>masl</i>	Meter above sea level
<i>mm</i>	Millimeter
Mm^3	Million cubic meter
<i>Mt/yr</i>	Million tons per year
<i>MVA</i>	Mega Volt-Ampere
<i>MW</i>	Megawatt
N/m^2	Newton per square meter
Ns/m^2	Newton second per square meter
<i>ppm</i>	Parts per million
<i>rpm</i>	Revolution per minute
<i>s</i>	Second
<i>sq.km</i>	Square kilometer

Chapter 1

Introduction

1.1 Background

Owing to the steep gradient in the Himalayas, high heads are available within a short reach, including abundant water availability, which provides a tremendous potential for hydropower in the region. Besides, steep terrain, fragile geology and intense rainfall also account for extremely high sediment conveyance in the Himalayan rivers (considered to be the highest in the world) posing a threat to many hydropower projects causing severe turbine abrasion, loss of revenue for maintenance and loss in energy production due to diminished turbine efficiency (Pradhan, 2004). Moreover, slope instabilities, land erosion and flooding caused by heavy rain are the inherent natural features in these basins, which further add the sediment loads in the river (Pandit, 2009). Himalayan rivers with such characteristics, constitute a major challenge regarding sediment handling at headworks.

Unlike reservoir projects, Run-of-River (ROR) plants have very less or no room to accommodate the incoming sediments before intake thereby, the plants are challenged by high sediment loads right from the early days in their operation (Annandale et al., 2016, ch. 8). In order to reduce the sediment-induced problems, settling basins are generally constructed in ROR plants before the flow is fed into the turbine to limit the sediment exposure of hydromechanical equipments. Sediment-induced wear being one of the main reasons for decrease in turbine efficiency, the role of settling basin can be vital. A well performing settling basin also helps in uninterrupted power generation during wet season with high amount of sediments (Biswhwakarma, 2015).

The 144 MW Kali Gandaki A Hydropower Plant (KGA), owned and operated by Nepal Electricity Authority (NEA), is a peaking ROR type project located in Western Nepal. The headworks has been facing problems related to unfavourable hydraulics at intake and settling basins and frequent choking of intake trash rack. Recirculation flows are observed in both sides of the forebay. Also, flow is not evenly distributed at the intake. The effect of concentrated approach flow, due to a very short transition between intake and settling basins, extends even inside the settling basins creating recirculation and formation of eddies, which are unfavourable to settle suspended sediments. Pertaining to uneven distribution of flow into the settling basins, the recirculating flow and formation of eddies, settling basins are not performing at their best. These have caused excessive sediment-induced turbine erosion far more than expected causing high operation and maintenance cost.

With an intention to improve the overall headworks hydraulic performance along with the flow patterns in the settling basins, a physical hydraulic model was built at 1:40 scale and tested at Hydro Lab, Nepal. The study was primarily focused on hydraulics within and nearby the intake area to achieve a satisfactory performance in terms of improved approach flow and flow distribution at intakes, handling of floating debris, flow patterns at inlet, main basin and outlet of the settling basins through modifications to existing headworks arrangement. The study has recommended

design modifications based on improved hydraulic performance and qualitative flushing test with sediments. However, the performance of the settling basins with modifications in terms of suspended sediment handling is still unsolved and hence is the purpose of the current work.

1.2 Master's Thesis Work

The main objective of this thesis is to investigate the performance of the settling basins of KGA with proposed modifications from the physical hydraulic modelling with respect to suspended sediments, utilizing the numerical model. SSIIM 1 is used for the numerical simulation with limited use of SSIIM 2 for coordinates extraction.

The work consists of:

- Literature study of sediment handling techniques at the headworks of ROR hydropower plant and analytical approaches for trap efficiency estimation.
- Literature study of model studies and relevant works with regard to modelling suspended sediment transport.
- Numerical modelling of hydraulics and calibration of the numerical model in model scale, against the velocity measurements from physical hydraulic model test performed at Hydro Lab.
- Numerical modelling of hydraulics and suspended sediments transport at intake and settling basins in prototype scale.
- Discussion on findings together with the evaluation of the performance of settling basins with modifications.
- Conclusion and proposal for future work.

1.3 Thesis Structure

This thesis contains ten main chapters. Chapter 1 presents the background for the master's thesis and objectives of the study. Chapter 2 contains an introduction to sediment transport theory, methods of sediment handling in ROR plants and overview on headworks, including design of settling basin, analytical approaches for trap efficiency estimation and potential hydraulic problems. Chapter 3 includes general theories on physical and numerical model along with the relevant works pertaining to sediment transport in headworks. Chapter 4 contains the information about the case, i.e., Kali Gandaki A Hydropower Plant (KGA), the problems in the existing design, recommendations from the physical hydraulic model and the need for numerical modelling. Chapter 5 describes the SSIIM software with a focus on SSIIM 1, which is used to simulate the case under consideration. Whereas, Chapters 6 and 7 present the procedures, considerations for simulations and results, for hydraulics and sediments, respectively. Chapter 8 contains the discussion on the simulation results and the evaluation of the performance of the settling basins with recommended design modifications. Chapter 9 includes the conclusion of the work and the last chapter, Chapter 10 comprises the suggestions for future work possibilities.

Chapter 2

Theory

2.1 Sediment Transport

The flowing water has a natural ability to transfer sediments for a given hydraulic and sediment properties. Sediments represent tiny particles like gravel, sand, silt and clay formed predominantly by the mechanical decomposition of rock.

2.1.1 Initiation of Motion

The forces acting on a particle resting on the bed, where the flow velocity is U are shown in Figure 2.1. These forces include gravity force F_G , drag force F_D , lift force F_L and friction force F_R , and they determine the stability of the particle (Olsen, 2017, ch. 9).

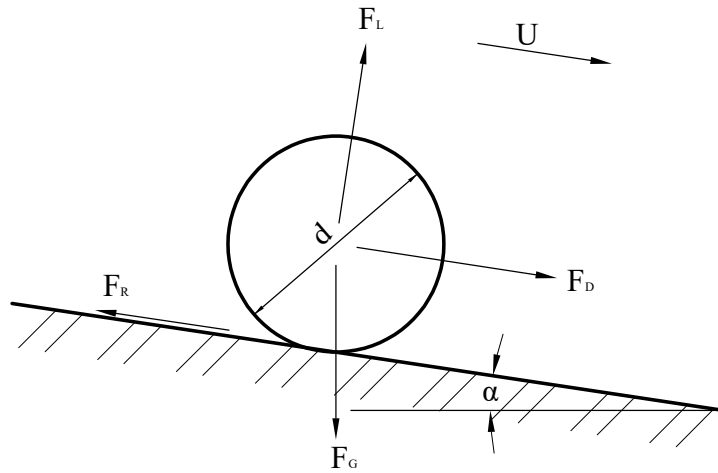


Figure 2.1: Forces acting on a particle in a stream (modified from Olsen, 2017, ch. 9).

For a particle with diameter d , the forces may be expressed as:

$$F_G = mg = \frac{\pi}{6}d^3(\rho_s - \rho_w)g = k_1(\rho_s - \rho_w)gd^3 \quad (2.1)$$

$$F_D = \frac{\pi}{8}C_D\rho_wU^2d^2 = \frac{\pi}{8}C_D\rho_w(IM^2R^{4/3})^2d^2 = \frac{\pi}{8}C_D\rho_w\left(\frac{\tau}{\rho_wgR}M^2R^{4/3}\right)^2d^2 \approx k_2\tau d^2 \quad (2.2)$$

$$F_L = \frac{\pi}{8}C_L\rho_wU^2d^2 \approx k_3\tau d^2 \quad (2.3)$$

$$F_R = (F_G - F_L) \tan \alpha \quad (2.4)$$

where, k_1 , k_2 and k_3 are the constant terms, m is the mass, g is the acceleration due to gravity, ρ_w and ρ_s are, respectively, the densities of water and sediment, C_D is the drag coefficient, I is the hydraulic gradient, M is the Manning-Stricklers friction coefficient, R is the hydraulic radius, τ is the bed shear stress, C_L is the lift coefficient, α is the angle between horizontal and the bed. Channel is assumed to be wide such that hydraulic radius is approximately equal to flow depth.

For force equilibrium along the direction of the bed, $F_R = F_D$. Using Equations (2.1) to (2.4) gives:

$$(k_1(\rho_s - \rho_w)gd^3 - k_3\tau d^2) \tan \alpha = k_2\tau d^2 \quad (2.5)$$

Replacing τ with critical shear stress, τ_c for equilibrium, and solving Equation (2.5) for particle diameter:

$$d = \frac{\tau_c}{g(\rho_s - \rho_w) \left[\frac{k_1 \tan \alpha}{k_2 + k_3 \tan \alpha} \right]} = \frac{\tau_c}{g(\rho_s - \rho_w)\tau^*} \quad (2.6)$$

where, τ^* is the *Shield's parameter*. Shields expressed the parameter as the function of particle Reynolds number, R^* (Equation 2.7), which represents the ratio of particle diameter and thickness of viscous sub-layer, and the parameter can be found using Shields graph (Figure 2.2).

$$R^* = \frac{u_* d}{\nu} = \frac{d}{\nu/u_*} = \frac{\text{particle diameter}}{\text{thickness of viscous sub-layer}} \quad (2.7)$$

where, u_* is the shear velocity and ν is the kinematic viscosity of water.

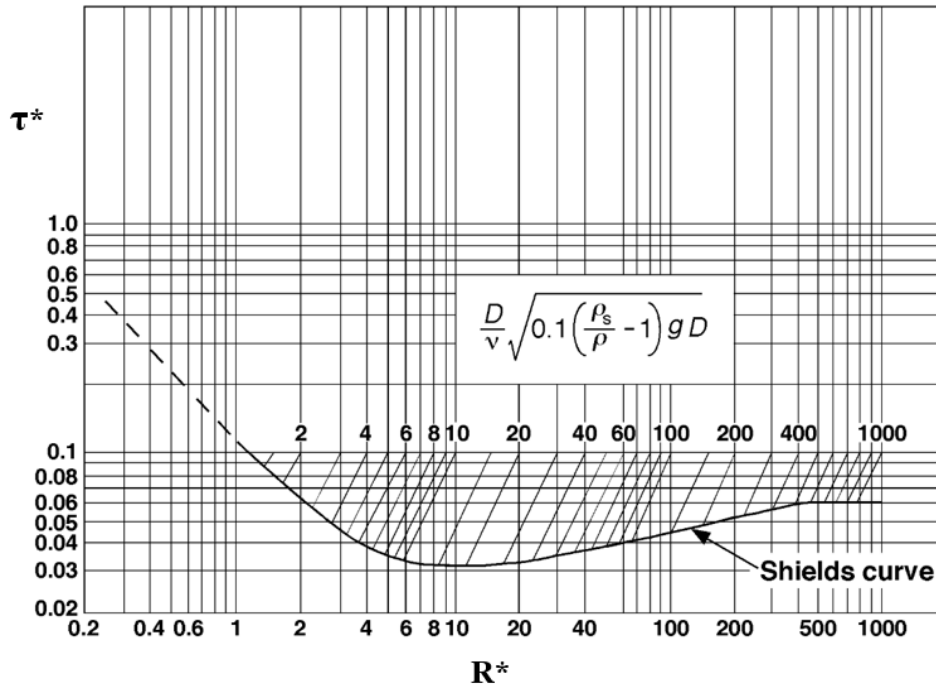


Figure 2.2: Shields graph for incipient motion (modified from USBR, 2006).

Shields graph may be used either to determine the particle size that is not movable for a known bed shear stress or to calculate the critical shear stress necessary to bring the particle of a definite size in motion.

2.1.2 Particles in Motion

Sediments are brought to motion when the bed shear stress surpasses a critical value. The movement of sediments may occur along the bed or in suspension based on the turbulence in water and grain size. Sediments can be classified as *bed load* and *suspended load* depending on the transport mechanism.

Bed load comprises particles that move close to the bed by rolling, sliding or saltation. While suspended load is composed of finer particles, which are light enough to be conveyed in suspension by the turbulence without frequent contact with the bed. There is yet another distinction called *wash load*, which refers to the particles washed away with the flow over a long distance with no interaction between bed sediments and has no morphological significance (Wang, Lee et al., 2015, ch. 1).

The *Hunter Rouse* parameter or *Rouse number*, z (Equation 2.8), is often employed to dictate the mode of transport and to evaluate the vertical distribution of suspended load concentration through concentration profiles, as shown in Figure 2.3. Rouse number is a dimensionless number expressed as:

$$z = \frac{w}{\kappa u_*} \quad (2.8)$$

where, w is the fall velocity, κ is the von Kármán constant equal to 0.4. According to Hearn (2008, ch. 12), the dominant transport process is mainly the bed load for $z \geq 2.5$, partly suspended load (50% suspension) for $2.5 > z \geq 1.2$, exclusively the suspended load for $1.2 > z \geq 0.8$ and wash load for $z < 0.8$. According to Julien (2010, ch. 10), for $z > 2.5$, sediment is dominantly transported as bed load in a thin layer near the bed. As the Rouse number reduces, an increasing portion of sediment is carried as suspended load, and sediment transport in suspension becomes significant mostly for $z < 2.5$. Likewise, Wang and Dittrich (1992) concluded that sediment transport with $z < 0.06$ should be regarded as wash load and with $z > 0.1$ as bed load.

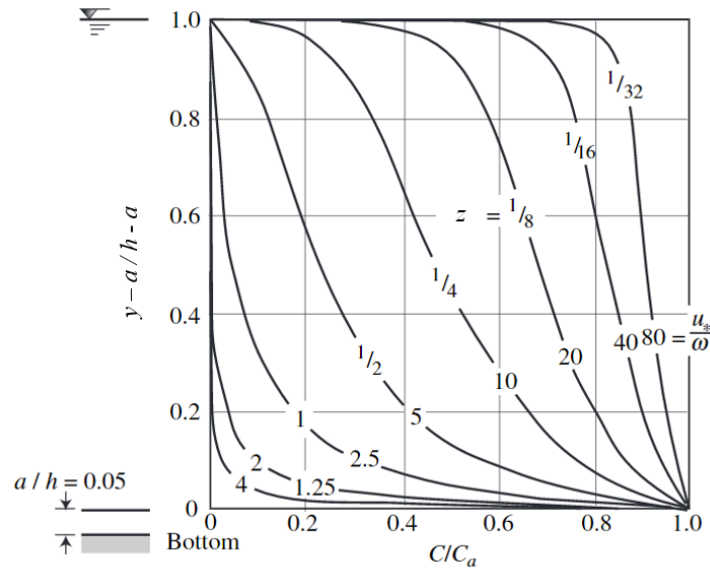


Figure 2.3: Vertical distribution of sediment concentration for selected values of z (modified from Julien, 2010).

The concentration profiles in Figure 2.3 are derived from Equation (2.9).

$$\frac{c(y)}{c_a} = \left(\frac{h-y-a}{y} \frac{a}{h-a} \right)^z \quad (2.9)$$

where, $c(y)$ is the sediment concentration at y distance above the bed, h is the flow depth and a

often set as 5% of h (Olsen, 2017, ch. 9) is the distance above the bed for reference concentration, c_a . Low values of z refer to higher turbulence compared to fall velocity so that the distribution of the sediments becomes progressively uniform across the flow depth. For high values of z , i.e., lower turbulence compared to fall velocity, the sediments move along the bed.

2.2 Sediment Handling in Run-of-River Hydropower Plant

Run-of-River (ROR) hydropower plant produces power from daily available flow of the river, with or without limited operational pondage or peaking storage for daily regulation of the flow. The pondage, especially during dry seasons, permits the plant to store water during off-peak hours, which can be utilized to operate at full capacity during peak hours to derive the benefit of price variances between peak and off-peak energy.

ROR plants basically operate under three streamflow-dependent operational regimes as indicated in Table 2.1.

Table 2.1 Operational regimes characteristics of ROR plants (Annandale et al., 2016, ch. 8).

Streamflow	Operation
< Design + environmental flow (very low sediment and floating debris)	All water diverted to power generation + environmental flow. Sluicing of sediments in front of intake as required.
> Design + environmental flow	Continuous discharge over a fixed weir and sluicing of excess water and sediment
> Maximum operational flow (substantial sediment and floating debris)	Intake out of service due to high amount of sediment and debris

The sediment concentration is generally limited during low flows with insignificant problems, except in sand-bed rivers. While during high discharges, both sediment concentration and suspended sediments captured by the intake tend to increase. Therefore, designers and operators should be more careful on intake performance during high flows.

2.3 Problems due to Sediments

ROR plants have very less or no room to accommodate the incoming sediments before intake. Consequently, the plants are challenged by high sediment loads right from the early days in their operation. The presence of sediments in diverted water decreases the conveyance capacity and damages the underwater hydromechanical equipment like turbine, valves, governors, etc. by their abrasive nature. The continuous wear and tear caused by the sediment reduce the efficiency of the plant significantly, which demands a high cost for frequent maintenance accompanied by substantial revenue losses during outages for maintenance. Annual operation and maintenance cost of plants with sediment problems can be upto 5% of the capital cost compared to 1.5% in plants with less sediment (Naidu, 1997, as cited in Pandit, 2009). Operating the plant with less efficient turbines further diminishes the revenue.

Moreover, ROR plants are often located in mountainous regions, at head reaches of perennial streams where the high stream relief causes significant hydraulic head over a comparatively short distance. Hence, a ROR may operate under heads ranging from few meters to over a thousand meters and the severity of the turbine abrasion by the sediment grows as a function of increased operational head (Nozaki, 1990, as cited in Annandale et al., 2016, ch. 8). In addition, these areas can be exposed to landslides, debris flow and glacial lake outburst floods, which can possibly add the sediments in the catchment.

2.4 General Layout of Headworks in ROR Hydropower Plants

ROR headworks comprises a weir or dam in the river for providing additional head and sufficient submergence for the intake, sluice gates for flushing accumulated sediments, an intake structure with trash rack for passing flow with minimal capture of sediment and floating trash, and settling basins to trap and exclude suspended sediments from water before it hits the turbine runner. A typical arrangement of a ROR hydropower headworks' components is shown in Figure 2.4. The function of ROR headworks is to extract required design discharge through the intake while allowing safe passage of the design flood, avoiding accumulation of sediment in front of intake, water borne debris and ice, and minimizing entrainment through the intake of suspended sediments and air, where applicable.

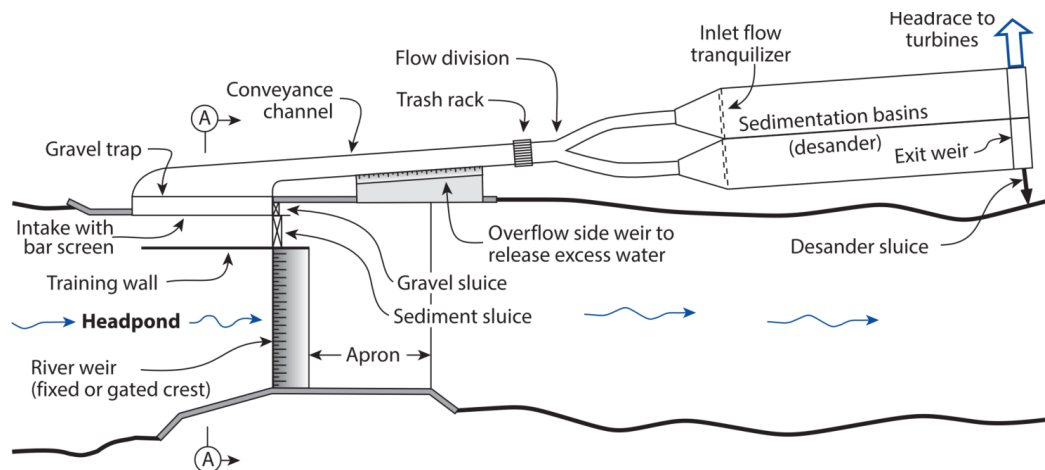


Figure 2.4: Typical arrangement of principle components of ROR headworks relevant to sediment management (Annandale et al., 2016, ch. 8).

Usually, diverted water passes first through a gravel trap at intake followed by settling basin to exclude sand and silt particles before being released for power generation. Sediments settled are then flushed from the settling basin either continuously or by intermittent flushing.

2.5 Strategies for Sediment Handling

Hydropower plants can last for a very long period; there exist several plants, been in operation for more than a century. Hence, the design should take into account the stream behaviour and sediment passage, together with erosion and deposition patterns that are likely to occur over many years and also during extreme events, for successful functioning over extended periods. For a small portion of the annual high flow diverted, placing the intake in the natural scour region at a curve in the river may suffice without any need for additional sediment handling components. While in case the diverted water exceeds around 40% of the mean annual flow, or in sand-bed rivers, active sediment management should be incorporated for intake design, including the requirement for gated structures capable of periodic sediment sluicing away from the intake (ASCE, 1995, as cited in Annandale et al., 2016, ch. 8).

2.5.1 Intake Location

A suitable geomorphic location for an intake can reduce the abstraction of sediments and produce a scour action that can keep the intake free of bed material accumulation. In a natural river, secondary currents are present that guide water and sediments from one bank to another, thereby creating zones of erosion and deposition. These effects are more distinct in river bends; erosion occurs at

the exterior of bends while deposition occurs at the interior. Secondary currents are also responsible for variation in sediment concentration within the cross-section such that the concentration near riverbed is generally greater than at the surface. When the current hits the outer bank of the bend, surface water laden with lesser sediment plunges and creates a rotational current eroding the toe of the outer bank as shown in Figure 2.5. The scoured bed material is carried and dumped by the current at the inner bank as the current crosses the riverbed.

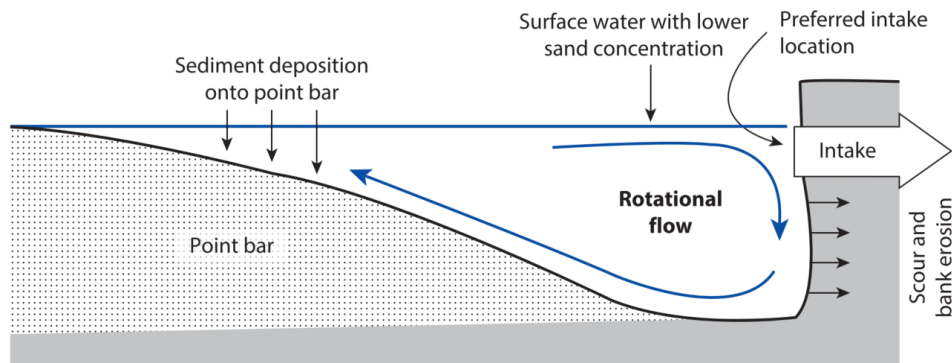


Figure 2.5: Section A-A (corresponding to Figure 2.6) showing rotational flow (Annandale et al., 2016, ch. 8).

Due to the rotational current, the sediment concentration entering an intake placed at the outer bank is less as water from the surface is drawn, and also scouring avoids any accumulation of sediments. In contrast, the inner bank will have higher sediment concentration and deposition of bed materials that can ultimately block the intake. So, intake on the outer bank is generally preferred for locating intake from the viewpoint of sediment management. The suitability for intake location is shown in Figure 2.6.

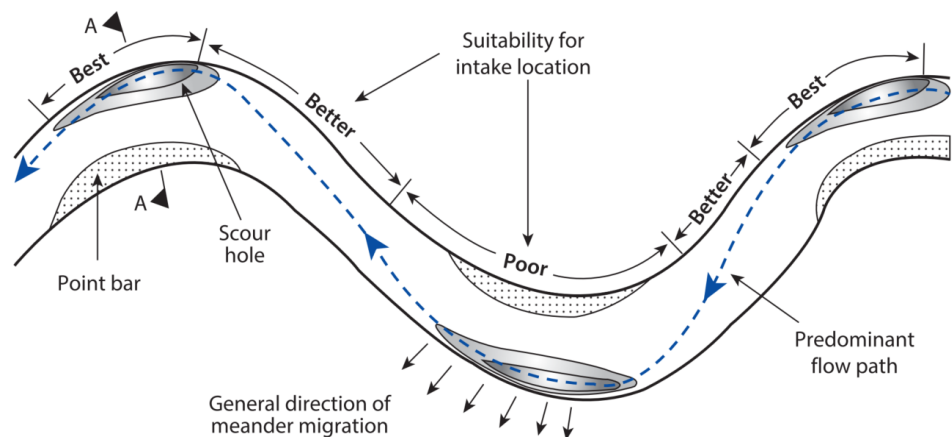


Figure 2.6: Suitability for intake location on idealized schematic river meanders (Annandale et al., 2016, ch. 8).

2.5.2 Flow Modification in Front of the Intake

In case the river geometry does not offer appropriate hydraulic conditions in front of the intake, a favourable flow pattern with improved secondary current may be attained by adjusting intake alignment, by operating gates, or by river training structures.

Orienting intake away from the flow can create eddies that may lift sediment into the intake while orienting intake slightly into the flow can reduce coarser sediment concentration by creating rotational flow. Similarly, for the gated weirs, the flow pattern may be enhanced by modifying gate

operation sequences as the river discharge changes. However, physical modelling is normally suggested to investigate these aspects of design and their impacts on sediment entrainment into the intake (Annandale et al., 2016, ch. 8).

2.5.3 Sustaining Peaking Storage

As mentioned in Section 2.2, ROR plants operate at rated capacity during wet season, while during dry season, pondage (if available) can make it possible to operate at full capacity during peak hours by utilizing water stored during off-peak hours or else they should operate at partial capacity. Peaking storage predominantly for high-head plants are valuable as additional revenue can be generated out of price difference between peak and off-peak energy. Furthermore, the need for peaking storage capacity is more in the scenario of blooming intermittent renewable energy sources like photo-voltaic and wind.

The peaking storage capacity in an on-stream reservoir may be lost by coarse bed materials brought along with the stream. The capacity can be sustained by measures, which include flushing, sluicing, dredging, mechanical excavation and sediment bypass tunnel. The maintenance of daily peaking storage with smaller volume is more economically feasible compared to that of larger volumes meant for seasonal regulation. Similarly, in case of a narrow reservoir, sluicing or flushing can effectively maintain pondage capacity. While for wider reservoirs, drawdown sluicing may be required to minimize sediment deposition during high sediment influx, as is done in some Himalayan ROR plants during monsoon (Annandale et al., 2016, ch. 7).

Bypass tunnel can create a sediment trap in the storage area itself, that decreases sediments and hydraulic load during power production. The strategy of bypass tunnel equipped with well-planned operating rule may even eliminate the need of settling basins, which can be an economic choice to substitute expensive underground basins (Annandale et al., 2016, ch. 7).

For off-stream storage, desander may be placed in series with or parallel to the pondage as shown in Figure 2.7. If the diverted flow passes through a desander followed by off-stream pondage, more amount of sediments will be trapped thereby reducing the possible wearing of turbines. Trapped sediments may be removed through a bypass or by dredging. While in case the off-stream storage parallel to the desander, storage is only used during low discharges when the sediment inflow is less without much implications for sediment removal.

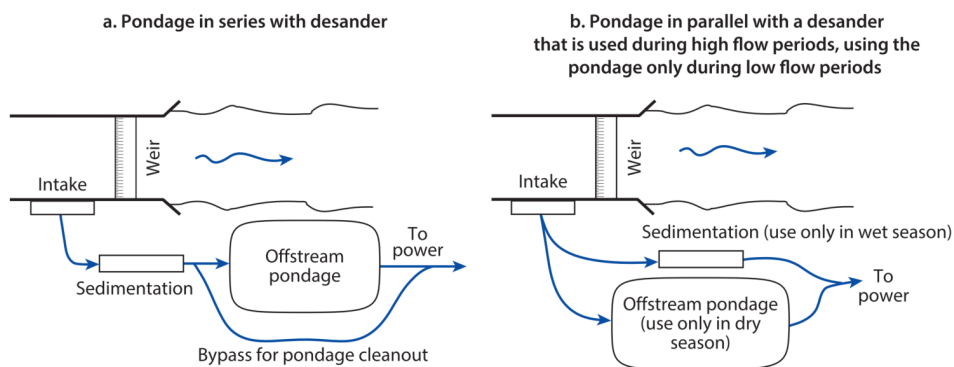


Figure 2.7: Arrangement for off-stream pondage (Annandale et al., 2016, ch. 8).

2.5.4 Removal of Suspended Sediments from Diverted Water

Settling Basin

Settling basins, also known as desanders or desilting basins or sedimentation basins are commonly used to exclude suspended loads greater than specific size (typically sand-size particles exceeding 0.15-0.20 mm, Annandale et al. 2016, ch. 8) from the diverted water. Usually, these structures are rectangular concrete basins meant for settling sands through energy dissipation by retarding the flow enough to settle out suspended particles under the action of gravity, achieved by increasing the flow area. However, in places with space limitations, underground chambers excavated along the headrace tunnel can serve for the purpose. Further details, including hydraulic design, hydraulic problems and flushing systems are discussed in Section 2.6.

Vortex Desander

Unlike common settling basin, circular vortex desander utilizes gravity and centrifugal acceleration to isolate sediment particles from the flow. A high velocity flow is fed tangentially into a cylindrical body creating a swirling motion. Particles denser than the fluid are flushed out through the orifice at bottom continuously. Vortex desanders have been used successfully for years in grit removal, wastewater treatment with limited application in hydropower plants so far. Vortex settling basin performed more efficiently compared to conventional settling basin as observed by Dhillon (1996, as cited Pandit, 2009).

2.5.5 Monitoring and Sediment-Guided Operation

Operational records of the performance measurements can be utilized for optimizing the performance of the headworks. Operational records may include the number of days with problems at headworks, which led to lowered water delivery, inflow and outflow concentration of suspended sediments, trap efficiency of basin, river water levels to verify the agreement with planned operation rule, sediment level in the basin before flushing, etc.

Sediment-guided operation refers to tuning the plant operation that suits the sediment load in real-time to decrease the impacts of sediments. Plant production may be decreased during flood events with high sediment volume to decrease hydraulic loading rate into the basin so that they perform efficiently or shut down temporarily to prevent damage. Operating a plant during periods when cost of damage outweighs the income from power generation is not healthy for the plant. Moreover, substantial revenues will be lost due to lowered efficiency of the turbine from abrasion damage. High discharges during plant shut down should be rather employed to flush accumulated sediment from the headpond. This approach requires real-time monitoring of sediment concentration and synchronization with the power dispatch center for balancing the grid.

Apart from reducing sediment exposure through aforementioned techniques, using improved turbine technology, including silt-friendly turbines together with efficient refurbishment and maintenance program can curtail the overall investment and operational costs of the plant (Pradhan, 2004). Also, it is of prime importance to take care of the possible abrasion of components while passing down the bed loads downstream. The vulnerable components include the sill and invert of outlets for passing sediments and appurtenant gate structures, upstream end of piers and guide walls, upper surface of undersluices. The potential wear can be reduced by providing high-strength sacrificial concrete layer without reinforcement or use of steel linings. Arrangements for placing stoplogs should be well ensured during design so that the affected area can be dewatered and refurbished during low flows (Annandale et al., 2016, ch. 8).

2.6 Design of Settling Basin

Settling basins are meant for reducing the mean particle size and total suspended sediment load in the diverted flow going to the turbine. The transit velocity of water in the basin is decreased

utilizing enlarged section so that the bed shear stress and turbulence are decreased, and gravity force becomes dominant thereby settling out the suspended sediments. The transit velocity is commonly in the range of 0.1 to 0.4 m/s ; however, at the planning phase, transit velocity of 0.2 m/s is generally adopted (Lysne et al., 2003, ch. 9).

2.6.1 Particle Size to be Excluded

As suggested by Støle (1993), it is economical to exclude most particles exceeding 0.15 to 0.30 mm , considering the turbine wear and generation losses. Nevertheless, the sensitivity of the turbine abrasion increases with the increase of the operational head, so the elimination of the particles should comply accordingly. Mosonyi (1991) prescribes removal of particles above 0.2 to 0.5 mm for medium head plants (15 - 50 m of head) and 0.1 to 0.2 mm for high head plants (50 - 250 m of head). The author further mentions, for very high heads of several hundred meters, removing particles as tiny as 0.01 to 0.05 mm only, may prevent the turbine abrasion. However, it is impractical to design a settling basin capable of removing all the incoming suspended sediments from economic perspective. Moreover, the fall velocities of silt and clay are very small compared to the turbulence in the settling basin (Lysne et al., 2003, ch. 9). Therefore, a trade-off between sediment trapping against the potential abrasion of hydromechanical equipment, maintenance costs and other related losses should be analyzed to decide the reference size of the particles for designing the settling basin that yields the optimum efficiency at a minimal cost.

2.6.2 Critical Flow Velocity

The transit velocity in the basin should not exceed the critical flow velocity to prevent the settled sediment particles from being scoured by the flow. Critical flow velocity, U_{cr} for incipient motion of the particles at the bed as prescribed by Camp (as cited in Mosonyi, 1991) is given below:

$$U_{cr} = a\sqrt{d_{cr}} \quad (2.10)$$

where, d_{cr} is the limit particle size (has to be in mm), while the constant:

$$\begin{aligned} a &= 51, & \text{for } d_{cr} < 0.1 \text{ mm,} \\ a &= 44, & \text{for } 0.1 < d_{cr} < 1 \text{ mm, and} \\ a &= 36, & \text{for } d_{cr} > 1 \text{ mm} \end{aligned}$$

2.6.3 Fall Velocity

Fall velocity of a particle is an important parameter of a sediment particle in relation to its motion. The flow attempts to scour and transfer the particles, while the downward motion counteracts against this effect (Lysne et al., 2003, ch. 9). It characterizes the ability of differently sized particles to fall under gravity in quiescent water (Avery, 1989). A sediment particle travels in suspension provided the vertical component of hydraulic turbulence exceeds the fall velocity (Morris and Fan, 1998, ch. 5). Fall velocity, w for particle Reynolds number less than 1 is given by (Stoke's law):

$$w = \frac{gd^2(\rho_s - \rho)}{18\mu} \quad (2.11)$$

While the fall velocity over the entire range of the Reynolds number is given by:

$$w = \left[\frac{4gd}{3C_D} \times \frac{\gamma_s - \gamma}{\gamma} \right]^{0.5} \quad (2.12)$$

where, g is the gravitational acceleration, μ is the dynamic viscosity of water, d is the particle size, ρ_s and ρ represent the densities of sediment and water, respectively, γ_s and γ represent the specific weights of sediment and water, respectively and C_D is the drag coefficient.

Rubey (Morris and Fan, 1998, ch. 5) devised a simplified equation to estimate fall velocity that works over the entire range of particle diameters, which is expressed as:

$$w = \frac{[1636(\rho_s - \rho)d^3 + 9\mu^2]^{0.5} - 3\mu}{500d} \quad (2.13)$$

The fall velocity of a particle prominently depends upon particle size, submerged weight, particle shape in a stream flow. However, it is also affected by temperature, and viscosity (Lysne et al., 2003, ch. 9). Figure 2.8 shows the fall velocity of quartz spheres in water and air for different temperatures.

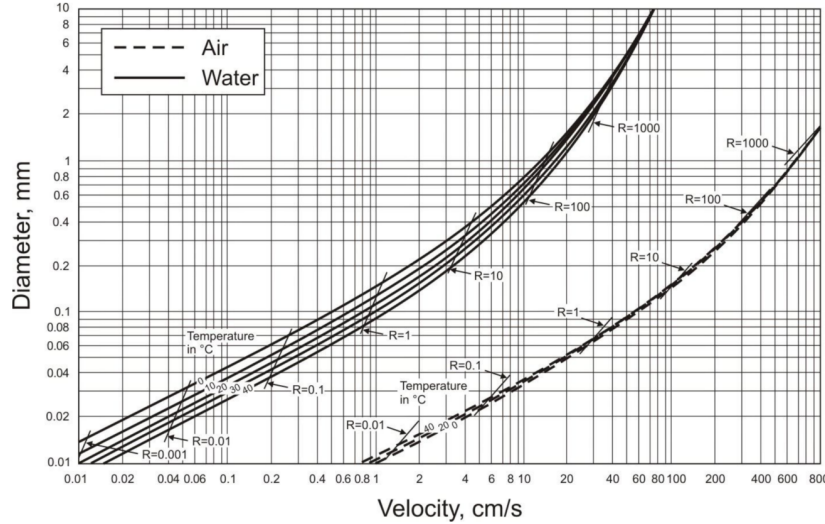


Figure 2.8: Fall velocity of quartz spheres in water and air (Lysne et al., 2003, ch. 9).

2.6.4 Trap Efficiency Computation

The trap efficiency is commonly used to quantify the functionality and performance of the desander. Higher the trap efficiency, better is the performance (Paschmann, 2018). It is an important criterion in designing and estimating the sediment concentration hitting the turbines, (Olsen and Kjellesvig, 1999). The trap efficiency of a settling basin, η is the decrease in sediment concentration, C from the inlet to outlet given by (Nøvik et al., 2014):

$$\eta = \frac{C_{in} - C_{out}}{C_{in}} \times 100\% \quad (2.14)$$

The trap efficiency of a settling basin is chiefly the function of basin shape and size. Several methods are available for computation of trap efficiency of the settling basin. Some of the methods used are mentioned below:

1. Hazen's Method (1904)

Hazen's method (as cited in Avery, 1989) takes into account the effect of both turbulence and imperfect flow distribution, which prevail in real cases. The formula proposed by Hazen is given by:

$$\eta = 1 - \left[1 + \frac{mwA_s}{Q} \right]^{-1/m} \quad (2.15)$$

where, m is the performance parameter varying from $m = 0$ for "best" basin and $m = 1$ for "very poor" basins, w is the fall velocity, A_s is the basin surface area and Q is the discharge. The drawback of this method is that several physical effects are represented by a single

parameter, m . If possible, it is advisable to consider each effect separately.

2. Velikanov's Method (1936)

Trap efficiency is calculated using Velikanov graph shown in Figure 2.9, in which trap efficiency, η is expressed as the function of coefficient, λ . The coefficient λ is given by the following relation (Sinha and Singh, 2019):

$$\lambda = \sqrt{\frac{7.51w^2L}{U^2(D^{1/2} - 0.2)^2}} \quad (2.16)$$

where, U is the flow velocity, L is the basin length and D is the flow depth.

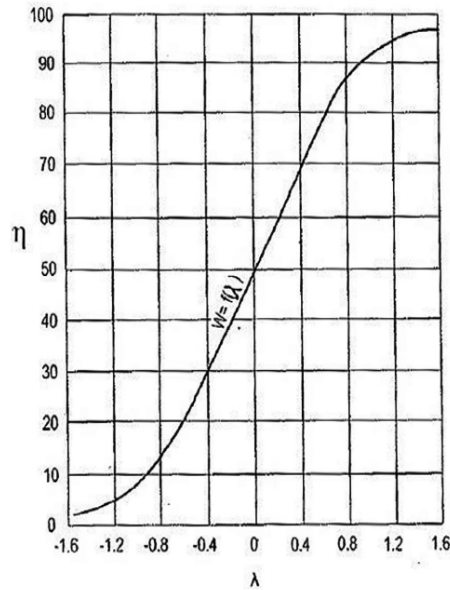


Figure 2.9: Trap efficiency as a function of λ (Sinha and Singh, 2019).

3. Camp's Method (1946)

Camp's method is based on the classic approach to design settling basin, based on the findings of Dobbins (1944, as cited in Avery, 1989). Fluid velocity and turbulent mixing coefficient are assumed to be constant throughout the fluid. The trap efficiency is derived as the relation:

$$\eta = f \left\{ \frac{wA_s}{Q}, \frac{w}{u_*} \right\} \quad (2.17)$$

where, u_* is the shear velocity. The trap efficiency is found from the Figure 2.10, for the computed values of w/u_* and wA_s/Q .

4. Vetter's Method (1940)

Vetter's method (as cited in Avery, 1989) is a simplified version of Hazen's method (Equation 2.15), assuming best performance ($m=0$) given by the following relation:

$$\eta = 1 - e^{-\left(\frac{wA_s}{Q}\right)} \quad (2.18)$$

Equation (2.18) is virtually identical to equation proposed by USBR (Vanoni, 1975, as cited in Sinha and Singh, 2019).

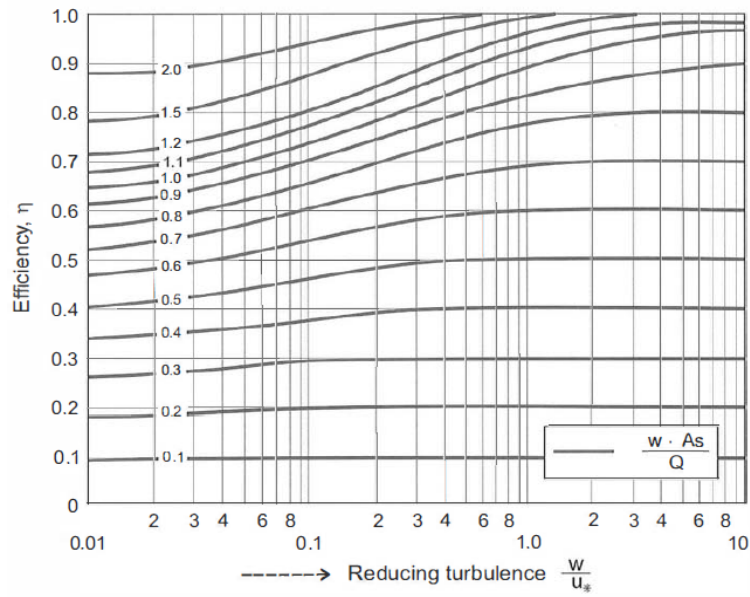


Figure 2.10: Camps diagram for trap efficiency including the effect of turbulence on the fall velocity (Camp, 1946, as cited in Lysne et al., 2003, ch. 9).

5. Sumer’s Method (1977)

Sumer (1977, as cited in Garde et al., 1990) proposed the following relation, where η is expressed as a fraction and is related to w/u_* as per the graph shown in Figure 2.11:

$$\ln(1 - \eta) = \frac{-\lambda u_* L}{15UD} \tag{2.19}$$

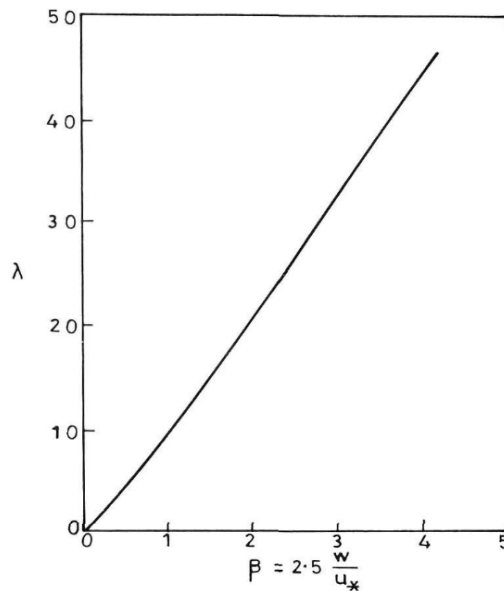


Figure 2.11: Sumer’s relation between λ and β (Sumer, 1977, as cited in Garde et al., 1990).

where, λ is a dimensionless number, $\beta = 2.5w/u_*$ is the velocity parameter. It should be noted that Figure 2.11 is valid for β less than 4, i.e., $w/u_* < 1.6$, and so for higher values, Sumer’s method may not be precisely applicable (Sinha and Singh, 2019).

6. Garde et al. (1990)

According to Garde et al. (1990), Camp, Dobbins, Sumer and USBR methods of computation of efficiency of settling basin are not satisfactory, in case of fine sediments. The efficiency of basin is represented by following exponential relation based on L/D and w/u_* :

$$\eta = \eta_0(1 - e^{-kL/D}) \quad (2.20)$$

where, η_0 is the limiting efficiency and k is the coefficient. The values of η_0 and k are determined from the mean curves and their variation based on w/u_* (Figure 2.12). These parameters tend to become independent of w/u_* for $w/u_* > 2.2$.

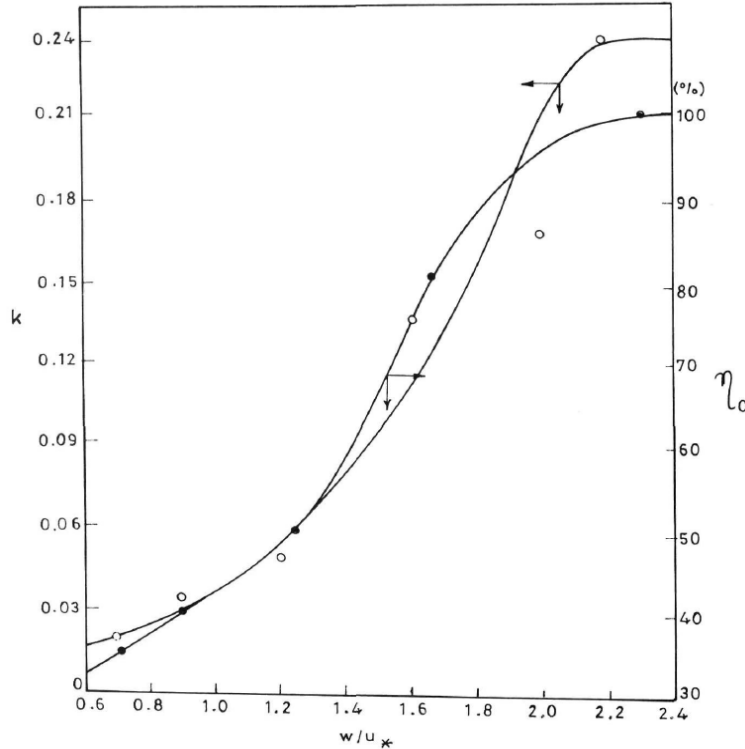


Figure 2.12: Variation of k and η_0 with w/u_* (Garde et al., 1990).

7. Raju et al. (1999)

According to Raju et al. (1999), existing empirical methods for computing efficiency, viz. Camp, Dobbins, Sumer, USBR and Garde et al. did not produce satisfactory results, particularly for fine non-cohesive sediments when $w/u_* < 0.4$. A new relation was developed for entire range of $w/u_* < 2.5$ given below:

$$\eta = 11.7(w/U)^{0.81}(LB/bh)^{0.23}(D^{1/6}/n\sqrt{g})^{0.98} \quad \text{for } w/u_* < 2.5 \quad (2.21)$$

where, B is the basin width, b is the width of approach channel, h is the flow depth in approach channel and n is the Manning's roughness coefficient. For $w/u_* > 2.5$, the efficiency was found to be 100%.

2.6.5 Design Concept of Ideal Basin

Figure 2.13 represents the definition sketch of an ideal settling basin based on the theory of sedimentation developed by Hazen (as cited in Avery, 1989). It assumes that flow and suspended particles at inlet are distributed uniformly (plug flow), the flow has no turbulence and the deposited particles do not get resuspended.

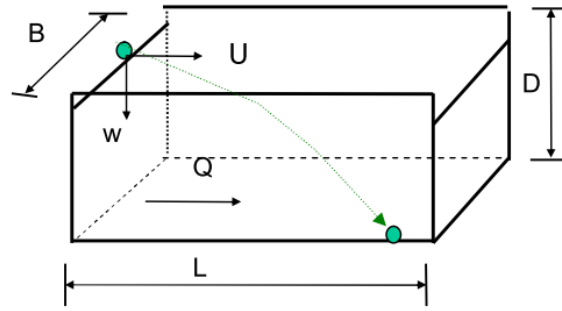


Figure 2.13: Ideal settling basin (Biswhwakarma, 2015).

Consider a particle entering the basin as depicted in Figure 2.13.

$$\text{Settling time, } T_s = D/w \quad (2.22)$$

$$\text{Retention time, } T_r = L/U \quad (2.23)$$

For quiescent settling, all particles of fall velocity, w are deposited when settling time equals retention time, i.e.,

$$\begin{aligned} D/w &= L/U \\ &= LA/Q \quad \because UA = Q \\ &= LBD/Q \quad \because A = BD \\ \implies w &= Q/(BL) \\ &= Q/A_s \quad \because A_s = LB \end{aligned}$$

where, L is the length of basin, B is the width of basin, D is the depth of flow, A is the cross-sectional area, A_s is the basin surface area and Q is the discharge. In general, for both ideal and real basins, the ratio wA_s/Q can be considered as a dimensionless parameter of the physical capacity of a basin with surface area, A_s to settle particles of fall velocity, w for both ideal and real basins (Avery, 1989).

2.6.6 Real Settling Basin

For efficient removal of the suspended sediments, the hydraulic design of the settling basin must ensure the following (Lysne et al., 2003, ch. 9):

- Uniform flow distribution among parallel settling basins for different discharges
- Uniform flow distribution within each basin for different discharges
- Efficient exclusion of deposited sediments during flushing operation

The typical arrangement of commonly used settling basin is shown in Figure 2.14. It consists of inlet channel, transition zone and settling zone or basin.

Settling Zone

Settling zone or basin is the main part where the settling of suspended sediment is supposed to occur. The hydraulic dimensions of the settling basin is chiefly governed by the fall velocity of the particles intended to be excluded and required degree of trapping of sediments (Pandit, 2009). Equations and graphs in Section 2.6.4 can be employed to determine the size of the basin for a chosen limit particle size. Various combinations of length, width and depth are considered to attain the intended basin trap efficiency and the optimal combination is implemented (Biswhwakarma, 2015). However, several recommendations regarding the basin dimensions exist for some practical reasons.

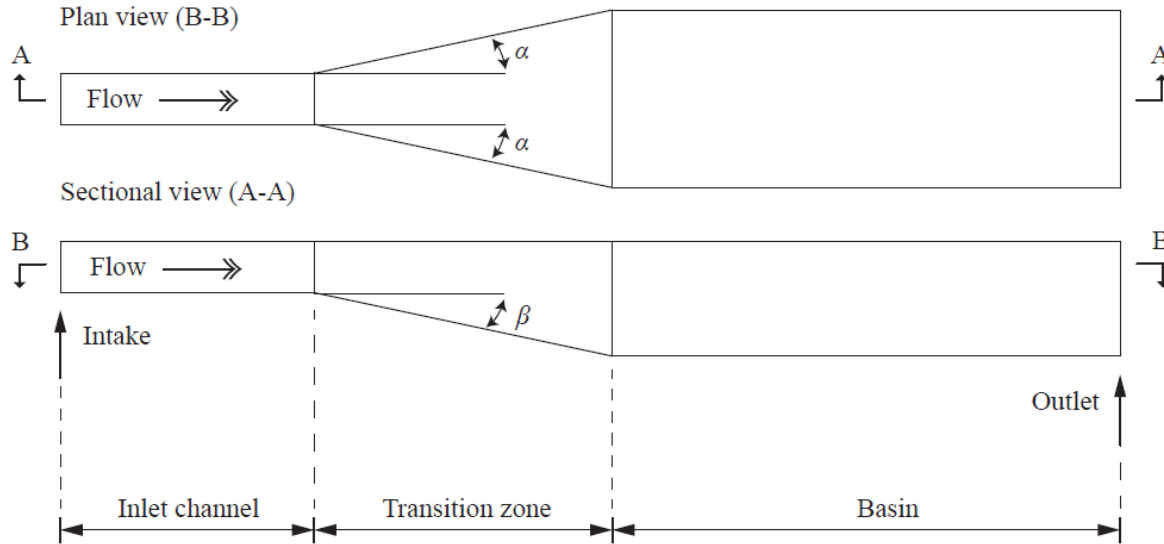


Figure 2.14: Schematic illustration of a typical elongated settling basin; α and β refer to the horizontal and vertical angles of expansions, respectively (Paschmann, 2018).

Mosonyi (1991) recommends D within the range of 1.5 to 4 m, with velocities not exceeding 0.4 to 0.6 m/s. While Giesecke et al. (2014, as cited in Paschmann, 2018), for an even flow distribution to reduce recirculation zones in the basin, recommend $L/B \geq 8$ and $B/D \approx 0.8$. According to Avery (1989), at least L/B of 2 to 3 should be maintained for hydraulic considerations. Similarly, according to TU Delft (2020), the *Camp* number C_p (analogous to square of Froude number) given by Equation (2.24) should not be less than 10^{-5} to avoid unstable flows with recirculation zones.

$$C_p = \frac{U^2}{gR} = \frac{Q^2(B + 2D)}{g(BD)^3} \quad (2.24)$$

where, R is the hydraulic radius of the settling basin (rectangular).

Camp (1936, as cited in Avery, 1989) demonstrated that the hydraulic performance of long narrow basins is better in comparison to that of wide low-velocity basins and also basin with higher values of Froude number exhibit better flow patterns and low dispersion. Besides, Lysne et al. (2003, ch. 9) recommend dividing the flow into two or more chambers in the settling basin so that it becomes possible to dewater one of the basins during dry periods that permit inspection and maintenance without affecting the plant production.

Transition Zone

The inflow should be evenly distributed over the width and the depth of settling zone to attain an optimum hydraulic efficiency and efficient functioning of settling basin. An uneven flow distribution in a settling basin results in considerably lower trap efficiency compared to a basin with uniform flow distribution (Lysne et al., 2003, ch. 9). Furthermore, recirculation zones and high eddies may be formed within the effective surface area of settling basins by the inlet geometry of the structure and inflow condition, which can subsequently lead to drop in the trap efficiency (Nøvik et al., 2014). The expansion from inlet channel to basin should be symmetric and gradual to avoid flow separation from sidewalls and bottom of transition zone.

Henderson (1966) recommends a value of $\alpha = 14^\circ$ corresponding to the ratio of 1:4 (1 in lateral direction and 4 in flow direction) so that the head loss is reduced, for the horizontal expansion as shown in Figures 2.14 and 2.15. While the value suggested by Lysne et al. (2003, ch. 9) is $\alpha < 5^\circ$ to 6° . Merkely (2004) prescribes an expansion angle of $\alpha = 9.5^\circ$. Likewise, Simanjuntak et al. (2009) found suitable hydraulic conditions for $\alpha = 14^\circ$ (corresponding to expansion transition of

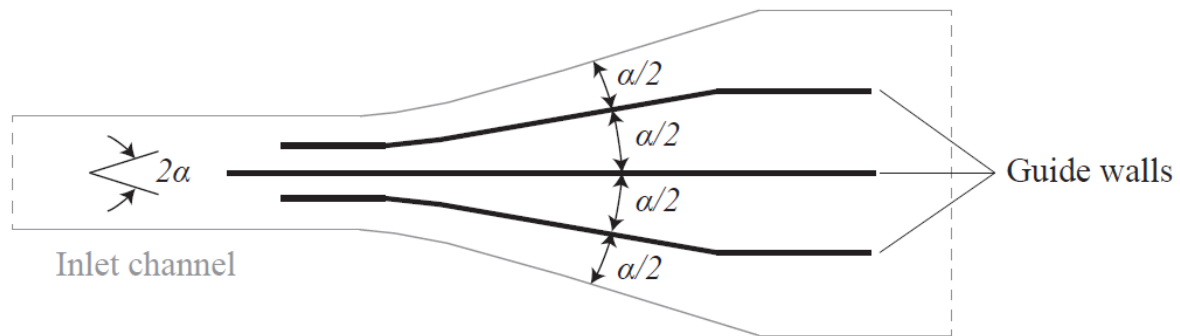


Figure 2.15: Transition zone with guide walls (Paschmann, 2018).

1:4) that reduced the head loss and provided optimum bed shear stress at the basin entrance, based on numerical simulations. The authors further mention that the deposition of suspended sediments is sustained without resuspension when the basin width is 1.75 to 2.00 times the transition length.

For the vertical expansion angle, β as shown in Figure 2.14, Qamar et al. (2014) based on model studies of desanders in Himalayan rivers, recommend $23.5^\circ \leq \beta \leq 26.6^\circ$ (corresponding to bed slope between 2.0 to 2.3). While $\beta \leq 18.43^\circ$ is recommended by Ortmanns (2006, as cited in Paschmann, 2018) with due consideration to adequate room for tranquilizers.

Further, Visher and Huber (2002, as cited in Paschmann, 2018) recommend the length of the transition zone to be twice the basin width. However, the length can be shortened by the use of guide walls, tranquilizers, perforated plates or slotted walls in the transition zone as recommended by Lysne et al. (2003, ch. 9).

Inlet and Outlet

The inlet channel should be linearly oriented with the transition zone and basin, preferably for a length of at least ten times its width (Lysne et al., 2003; Qamar et al., 2014) to ensure homogeneous approach flow towards basin preventing the effect of rotational flow created by the bend in the inlet channel.

The operating level of the basin is generally governed by the a weir at the outlet. If the outlet is narrower than the basin, smooth transition should be provided to secure uniform flow abstraction and reduction in flow disturbances. However, the contraction at the outlet can be more abrupt compared to inlet expansion (Avery, 1989). Also, it is possible to install perforated plated or slotted walls as in the case of inlet transition zone (Lysne et al., 2003, ch. 9). As per Qamar et al. (2014), the centre line of the outlet should overlap with the basin axis to ensure even abstraction over the whole basin width. The authors further mention that the outlet should be as high and wide as possible.

2.6.7 Data Requirements

It is essential that sediment data, including suspended sediment load, concentration, particle size distribution and quartz content are available for the successful planning, designing and operation of settling basin. Particularly for ROR plants, information regarding quartz content and concentration of suspended sediments in diverted water along with their seasonal variation, is more vital (Biswhwakarma, 2015).

2.6.8 Potential Hydraulic Problems in Settling Basin

When the flow is uniform in the settling basins, settling occurs efficiently and the hydraulic size of the basin is computed based on the same assumption. In practice, however, flow conditions are far from ideal, resulting in lower sand trapping than expected. Hydraulic problems commonly observed in settling basins, which are responsible for reducing trap efficiency are given below (Annandale et al., 2016, ch. 8):

Hydraulic short-circuiting

A part of the flow along with the sediments follows the shorter path compared to the design path from inlet to outlet of the basin, which reduces both detention time and trap efficiency, whereas in other parts of the basin, recirculation zones or dead zones are prevalent.

Flow splitting

The hydraulic loading rates are not uniform among parallel basins when the diverted water flow is not evenly divided. The trap efficiency of the overlaid basin is lowered so that higher concentration of sediment will be released.

Entrance jets

When the velocity in the conveyance channel between intake and settling basin is high, flow can form jet penetrating deep into the basin resulting in large secondary currents and recirculating flows, which are not favourable for efficient settling of sediments, as shown in top basin of Figure 2.16a.

Non-parallel flow paths

The conveyance channel may have bend right before the basin, which forces the flow against one of the sides of the basin or the entrance may be unsymmetrical relative to the basin, as shown in Figure 2.16b, or exit weirs may be located on to the side of the basin rather than having entrance and exit zones along the straight line, as shown in Figure 2.16c. These can deviate the flow towards one side of the basin while forming a dead zone on the opposite side.

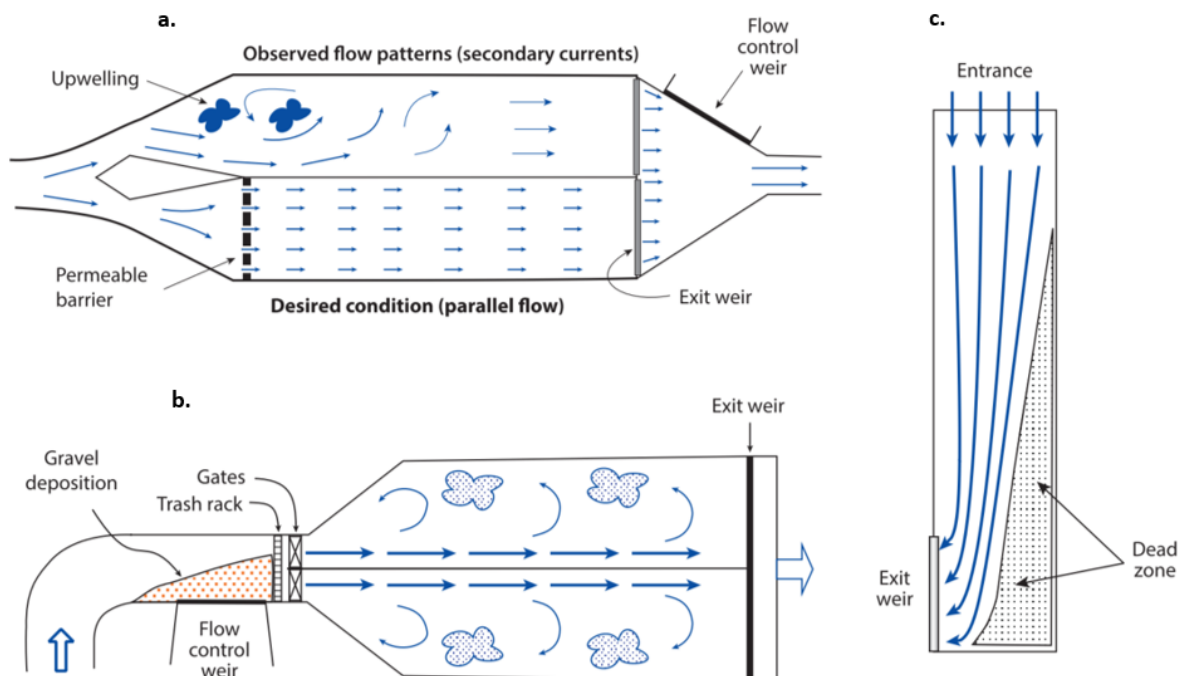


Figure 2.16: Undesirable hydraulic geometry observed in settling basins (modified from Annandale et al., 2016, ch. 8).

Hydraulic overload

Headworks are commonly provided with an overflow weir to discharge excess flow during high river levels since control of rate of flow diversion is not precise at the intake. If the overflow weir is placed downstream of the basin, excess flow passes through the basin producing maximum hydraulic overload during floods when sediment concentrations are at peak. Therefore, overflow weir should be placed before the settling basin so that only design flow passes through the basin.

It is essential to reduce these hydraulic shortcomings that produce flow disparity, hydraulic short-circuiting and high or imbalanced hydraulic loading rates so that settling of sediments is optimum. One of the economic methods to improve the flow patterns is to install a flow tranquilizer at the basin inlet that homogenizes the flow evenly across the cross-section of sedimentation zone, serving for improved basin hydraulics, as in bottom basin of Figure 2.16a. While in some cases, side outlet weirs can be shifted across the end of the basin without much expenses, to straighten the flow path.

2.6.9 Sediment Flushing

Settling basins are provided with certain dead storage to accumulate sediments between flushing processes. Further deposition after exceeding dead storage will decrease the effective cross-section thereby increasing the transit velocity and reducing the trap efficiency. Hence, the deposited sediment needs to be flushed out so that the settling efficiency is sustained, and production regularity is confirmed. The deposition rate is governed by the concentration of suspended sediments in diverted water and particle size distribution for specific hydraulic condition. The decrease in storage capacity of the basin is proportional to the increase in concentration, which requires increased flushing frequency (Biswhwakarma, 2015).

There are various flushing technologies available, which are classified into two principle categories based on plant operation regularity during flushing, which are given below (Lysne et al., 2003, ch. 9):

1. Power plant closed down during flushing
 - a. Conventional gravity flow flushing
 - b. Mechanical removal
 - c. Manual unloading (small projects only)
2. Power plant in operation during flushing
 - a. Continuous flushing
 - b. Intermittent flushing

The flushing of deposits in the first mode is done while shutting down the operation of the plant either by conventional gravity flow flushing or mechanical/ manual excavation. A swift velocity is required inside the basin to erode and transport the deposits during conventional gravity flow flushing. It involves operation of flushing gates while the flushing flow is adjusted by the inlet gate. The capacity of the flushing gate should be adequate to ensure even abstraction of water covering the entire width of the basin so that islands of deposits are avoided.

In the second mode, flushing is carried out without shutting down the plant. Continuous flushing involves extraction of water through a series of orifices along the bottom of the settling basin continuously, preventing any deposition during the plant operation. The water consumption generally ranges from 20 to 30% of the flow passing through the basin. The commonly adopted flushing arrangement in this category comprises longitudinal hoppers with flushing canals that run along the bottom of the hopper. On the contrary, intermittent flushing involves no loss of water during the time between flushing operations, so the flushing water consumption is less compared to that of continuous flushing. There exist several intermittent flushing systems, namely *Hopper system*, *Bieri system*, *Serpent Sediment Sluicing System (S4)* and *Slotted Pipe Sediment Excluder*.

Chapter 3

Model Studies

A model refers to a system that functions analogous to other system under consideration and offers precise prediction of their behaviour. Three types of models are commonly used in hydraulics: *analytical* models, *physical* models and *numerical* models (Chanson, 2004, ch. 13). However, only the latter two are described in the following text.

3.1 Physical Model

A physical model is a scaled representation of a hydraulic flow situation, where boundary conditions, upstream flow conditions and the flow field are scaled suitably for investigation under a controlled environment to predict the flow behaviour in the prototype. Usually, physical hydraulic models are used during the design phase to optimize the design of a structure and confirm operational safety, including their role in the decision-making process in selecting a technically and economically optimal solution design. It is common to employ a smaller size model of the prototype however, some applications (for example, water treatment plant, flotation column) may demand the model larger in size than the prototype (Chanson, 2004, ch. 14).

Apart from the conventional use of physical models in the design of hydraulic engineering works, they are also being used as *process* models and *validation* models. Process models cover investigations of physical processes to expand the existing knowledge of fundamental physics while validation models are employed to yield test data against which numerical models may be compared, validated and calibrated (Chadwick et al., 2013, ch. 11).

3.1.1 Basic Principle

Model studies require due consideration of similitude, realistic model scales, model layout and construction. A model is said to have similitude with the prototype (i.e., the flow conditions are similar in model and prototype) if the model shows similarity of form (*geometric similarity*), similarity in motion, i.e., time and velocity (*kinematic similarity*) and similarity of forces (*dynamic similarity*).

Geometric similarity indicates that the ratios of all corresponding model and prototype dimensions are the same. Also, all corresponding angles are equal in both model and prototype.

$$L_r = \frac{L_m}{L_p} = \frac{B_m}{B_p} = \frac{D_m}{D_p} \quad \text{Length} \quad (3.1)$$

where, the subscript r refers to the ratio of model-to-prototype, while m and p refer to model and prototype parameters, respectively. The parameters for geometric similitude include length, width, depth, area and volume.

Kinematic similarity indicates that the ratios of velocities and accelerations at homologous points in model and prototype are equal.

$$U_r = \frac{(U_1)_m}{(U_1)_p} = \frac{(U_2)_m}{(U_2)_p} = \frac{(U_3)_m}{(U_3)_p} \quad \text{Velocity} \quad (3.2)$$

Dynamic similarity indicates that ratios of model and prototype forces are constant, i.e., force polygons are similar in geometrically equivalent points in model and prototype.

$$F_r = \frac{(F_1)_m}{(F_1)_p} = \frac{(F_2)_m}{(F_2)_p} = \frac{(F_3)_m}{(F_3)_p} \quad \text{Force} \quad (3.3)$$

Other parameters considered in dynamic similitude include work and power.

The ratios L_r , U_r and F_r , as defined in Equations (3.1) to (3.3) are *basic-scale* ratios from which other scale ratios can be defined as given below:

$$\text{Mass, } M_r = \rho_r L_r^3 \quad (3.4)$$

$$\text{Time, } t_r = \frac{L_r}{U_r} \quad (3.5)$$

$$\text{Discharge, } Q_r = U_r L_r^2 \quad (3.6)$$

$$\text{Pressure, } P_r = \frac{F_r}{L_r^2} \quad (3.7)$$

where, ρ is the density of the fluid.

3.1.2 Model Laws

Model relations are derived based on dimensionless combinations of appropriate parameters. It is not possible to satisfy all force ratio requirements if the model is smaller than the prototype. So, model studies, which use downscaled topography need to disregard some less relevant parameters to simulate more important parameters (Lysne et al., 2003, ch. 10). There exist several model scaling laws, based on the respective dimensionless number, which has to be chosen as per the purpose of the investigation. *Froude* number is generally used for scaling free-surface flows, open channels where gravity is important. Similarly, for enclosed flow situations like pipe flows, turbomachines, valves where viscosity has the major effects, *Reynolds* number is used. When inertial and surface tension effects are predominant, like in the studies of air entrainment in flowing water, similarity based on *Weber* number is employed. *Euler* number is used for scaling models where pressure forces are dominant on flow as in flow through turbines and pumps (Chanson, 2004, ch. 14).

Froude Law

Gravity effects are dominant in free surface flows (e.g. rivers and wave motion). In such case, the similarity between model and prototype is performed usually by Froude similitude, which relates gravity and inertial forces, neglecting the effects of surface tension and viscous forces. Froude law is obtained by equating corresponding Froude numbers ($Fr = U/\sqrt{gL}$; L is the characteristic dimension) of the model and the prototype:

$$Fr_p = Fr_m \quad (3.8)$$

Scale ratios obtained by using Froude law are given in Table 3.1. Model laws based on other dimensionless numbers are not discussed here as they are not relevant to the current study.

Table 3.1 Scale ratios based on Froude law.

Parameter	Scale ratios in term of L_r
Length, L	L_r
Velocity, U	$L_r^{1/2}$
Time, t	$L_r^{1/2}$
Discharge, Q	$L_r^{5/2}$

3.1.3 Disadvantages of Physical Model

Physical models produce spontaneous qualitative impression compared to numerical models through a direct illustration of the flow and sediment patterns. However, these models involve high expenses, long duration for extensive simulations and are immovable. The models once built can be neither easily replicated nor stored for an extended period in case further investigations are required in future (Morris and Fan, 1998, ch. 11). Physical models cannot reproduce all the physical processes occurring in the prototype in correct proportion as dictated by model laws, giving rise to scale effects (Chadwick et al., 2013, ch.11). Scale effects are the distortions caused by viscosity or surface tension other than the governing dominant forces. Different fluids need to be used to possibly attain the same Reynolds and Froude number in model and prototype that makes the model impractical and uneconomical (Chanson, 2004, ch.14). Besides, the measuring probes may disturb the flow or the flow may be unreachable to be measured with the available instruments (Ferziger et al., 2020, ch. 2).

According to Olsen (2017, ch. 9), simulating multiple sediment processes may not be possible in the physical model since different scaling laws produce different model sediment characteristics. Furthermore, scaling down finer sediments (less than 0.1 mm) can involve particles with cohesive forces and physical models are not capable of accurately reproducing cohesive sediment behaviour (Morris and Fan, 1998, ch. 11). Olsen (2017, ch. 9) further mentions that scaling bed forms is difficult in the physical model. It is nearly impossible to attain the same ratio of bed form height to water depth in model and prototype thereby causing different influences on the energy loss and sediment transport capacity in model and prototype.

3.2 Numerical Model

With the advent of powerful computers, numerical models have emerged as an alternative or at least a complementary tool to physical model studies (Ferziger et al., 2020, ch. 2). Numerical models can be advantageous compared to physical models for their lower cost, simplicity in repeating simulation for different conditions, portability, reproducibility and the ability to simulate sediments, including the problems inappropriate for physical modelling like sediment cohesion (Morris and Fan, 1998, ch. 11).

The physical aspects of fluid flow are based on three conservation laws: conservation of mass, conservation of momentum and conservation of energy (Anderson, 2009). Computational Fluid Dynamics (CFD) predicts quantitatively the fluid flow phenomena, by utilizing numerical methods and algorithms on the governing equations based on the conservation laws. The predictions occur under the defined conditions with regard to flow geometry, fluid properties, and the boundary and initial conditions of the flow field. Such predictions generally cover sets of values for flow parameters including velocity, pressure, or temperature at selected locations in space and for selected times (Hu, 2012).

Nevertheless, hybrid modelling approaches that involve combined physical and numerical modelling accompanied by field measurements are more preferred nowadays. Physical models together with the visual response through an immediate qualitative representation of the physical processes can

provide test data for verification of numerical model and input data for further investigation. On the other hand, numerical models may be employed for predicting spatial and temporal variation of velocity and sediment transport fields without scale effects (Chadwick et al., 2013, ch. 11).

3.2.1 Grids

In order to solve the governing equations for a given fluid geometry by a computer software, the geometry should be in the form compatible to the program. The geometry should be divided into a set of finer elements called *cells*. The program solves the governing equations in each of the cells. These cells divide the computational domain into distinct, non-overlapping geometrical space without any isolating holes between them. The complete network of the cells is called a *grid* or a *mesh*. The intersection points are called *grid points* or *vertexes*, which are connected by *grid lines*. The shape of cells can be *triangular*, *quadrilateral* or *polyhedral* in 2D grids and *tetrahedral* or *hexahedral* in 3D grids.

Grid Types

Grids can be divided into several types based on different characteristics, namely *orthogonality*, *structure*, *blocks* or *movement* (Olsen, 2017, ch. 5). Orthogonality is represented by the angle formed by intersection of grid lines. If the angle is 90° , the grid is said to be orthogonal and if not, the grid is non-orthogonal. Likewise, grids can be *structured* or *unstructured* based on structure. In a structured grid, the grid cells can be distinctively identified by using *i*, *j* and *k* indexes while this is not possible in an unstructured grid as the cells are not in particular order. The structured grids are composed of quadrilaterals in 2D and hexahedra in 3D. The unstructured grids cells are triangles in 2D and tetrahedra in 3D however, combination of triangles and quadrilaterals in 2D and hexahedra, tetrahedra, prisms and pyramids in 3D are also possible (Blazek, 2015, ch. 3).

The structured grids allow for easy access to the neighbor cells and thereby simplify the evaluation of gradients, fluxes and boundary conditions due to consistent connectivity as opposed to unstructured grids. However, structured grids have limitation in adapting to complex geometries, for which several structured grids representing different parts in a domain may be connected to form the whole domain (Blazek, 2015, ch. 3). Each structured grid, in this case, is known as a *block*, which is connected to form a *multi-block* grid that encompasses the whole domain. Another possibility is to *outblock*, where some cells are made inactive to adjust the grid to a complex geometry (Olsen, 2017, ch. 5).

When it is essential to simulate the vertical movements like changes in water levels or changes in bed levels or lateral movements, as in the case of a meandering river, *adaptive* grids can be utilized. The adaptive grid allows movement of the grid according to the solution during simulation. Besides, it is often desirable to simulate the interior part of concern in more detail, like computation of local scour around the pier in the river or dispersion of pollutants at the source in a lake. In such cases, a *nested* grid may be employed where the part of interest is modelled by finer grid overlapping the coarser grid defining the whole domain (Olsen, 2017, ch. 5).

Grid Qualities

The accuracy and convergence of a finite volume algorithm relies on the grid qualities represented by *non-orthogonality*, *aspect ratio* and *expansion ratio*. The non-orthogonality refers to the deviation of the angle between intersecting grid lines from 90° . The grid lines should be made with low non-orthogonality with an intersection angle as close as being perpendicular so that quick convergence can be attained together with improved accuracy in some instances. The situations where grid lines intersect below 45° and beyond 135° should be avoided (Olsen, 2017, ch. 5).

The aspect ratio or distortion ratio refers to the ratio of grid dimensions in two different directions, and the expansion ratio means the ratio of grid dimensions of consecutive cells in the same direction. These ratios should be kept as low as possible to evade convergence issues and inaccuracies. The aspect ratio of 2 to 3 is tolerable if flow direction is along the longest cell side. However, aspects ratios of 10 to 50 cause retardation of convergence speed, which demands an enormously large

number of iterations. The expansion ratios below 1.2 are generally preferred, and if the ratio is as high as 10, simulation can end up with unrealistic results (Olsen, 2017, ch. 5).

3.2.2 Spatial Discretization

Discretization is the process of approximating the partial differential equations by the system of algebraic expressions linking variables at discrete locations in space and time (Ferziger et al., 2020, ch. 2). Each differential term in the governing partial differential equation is substituted by algebraic equation where the variable in one cell is expressed as a function of the variables in the adjacent cells. There are several discretization approaches, of which three broadly used methods are described below:

Finite Difference Method

The finite difference method is applied directly to the governing equations in differential form. Taylor series expansion or polynomial fitting is utilized to approximate the derivatives of the flow variables with respect to spatial coordinates. The method is simple and effective provided the grids are structured with the possibility of attaining higher-order approximations. Furthermore, it can also compute values at locations other than grid nodes by interpolation (Ferziger et al., 2020, ch. 2). As this approach demands a structured grid, the application is restricted rather to simple geometries, which is a major disadvantage in complex flows. Besides, it can not be employed to a body-fitted or curvilinear coordinates directly.

Finite Volume Method

The finite volume method employs integral form of governing equations. The method discretizes the governing equations by subdividing the computational domain into several adjoining control volumes. The surface and volume integrals are then estimated by applying suitable quadrature formulae, which result in algebraic expression in each cell involving several nodal values of the neighboring cells (Ferziger et al., 2020, ch. 2). The flow quantities are either stored at centroids of grid cells (*cell-centered scheme*) or at the grid points (*cell-vertex scheme*) (Blazek, 2015, ch. 3).

The major advantage of this method is that spatial discretization is done in the physical space directly, so the physical system should not be transformed into a computational coordinate system. Also, the finite volume method can adapt to any grid type, whether structured or unstructured, and hence is suitable for complex geometries. As the method involves the direct discretization of conservation laws, it conserves the mass, momentum and energy (Blazek, 2015, ch. 3). However, this method requires three levels of approximation: interpolation, differentiation and integration which imposes difficulty in developing methods of order higher than second in 3D (Ferziger et al., 2020, ch. 2). Owing to its flexibility and conservative properties, the finite volume method is the most commonly used approach nowadays.

Finite Element Method

The finite element method was conventionally used in solid mechanics and it gained popularity during the 1990s in solving problems related to fluid dynamics (Blazek, 2015, ch. 3). Similar to the finite volume method, the computational domain is split into discrete elements. The distinctive feature of this method is the use of weight function before integration over the whole domain (Ferziger et al., 2020, ch. 2). The finite element method involves a rigorous mathematical foundation, and the numerical effort required, compared to the finite volume method, is significantly higher. However, the finite element is particularly suited for non-Newtonian fluids (Blazek, 2015, ch. 3). Besides, due to its integral formulation and unstructured grids this method is suitable for flows in complex geometries.

Apart from the schemes described earlier, some other approaches exist, namely *Spectral-element* method, *Lattice Boltzmann* method, *Gridless* method.

3.2.3 Discretization Schemes

The approximations of surface integrals and volume integrals need the value of the variables at cell faces (Ferziger et al., 2020, ch. 4). Values at cell faces are obtained by interpolation of the results, which are typically stored at grid centers. Numerous numerical schemes exist to perform the spatial discretization/interpolation within the methods discussed earlier. Some of them are briefly described in the following text by the finite volume method for a structured grid; nevertheless, these schemes are also appropriate to other approaches.

Figure 3.1 shows a typical Cartesian control volume in 2D where P represents the central cell, and other cells are named according to cardinal directions (North, East, South and West) with respect to P. The equations that shall follow hereafter in this section comply to the Figure 3.1. The expressions only for face labelled e are given; however, analogous expressions can be obtained by substituting indexes appropriately.

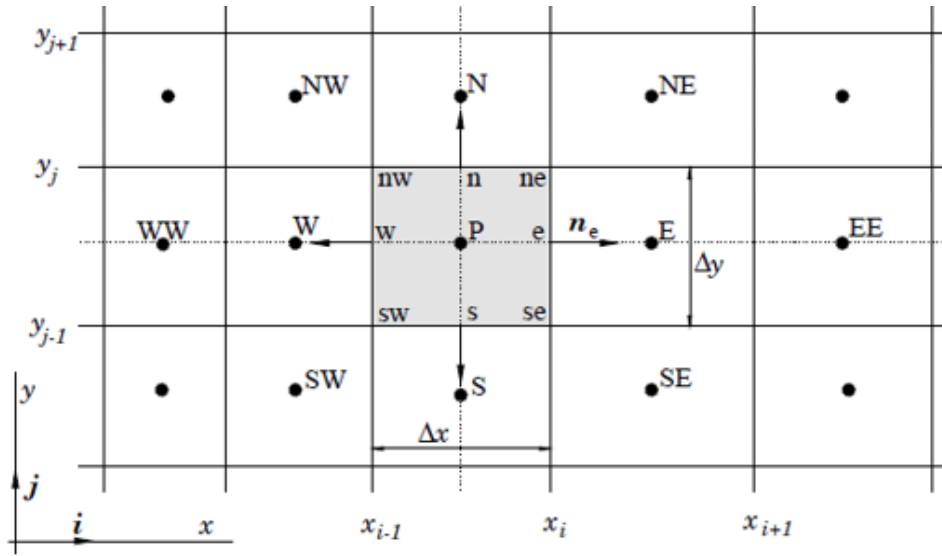


Figure 3.1: A typical control volume in Cartesian 2D grid (Ferziger et al., 2020, ch. 4).

Central scheme is based on the central difference formula or central averaging. The conservative variables to the left and to the right are averaged arithmetically to attain the flux at a common interface of the control volumes (Equation 3.9). As this scheme can generate two independent solutions of the discretized equations, it requires addition of artificial dissipation for stability (Blazek, 2015, ch. 3). The drawback of the scheme is that the increased diffusivity may produce a different result from what a real diffusion would produce (Olsen, 2017, ch. 6).

$$\phi_e = \frac{\phi_E + \phi_P}{2} \quad (3.9)$$

where, ϕ is the face value of general property at faces represented by subscripts corresponding to cardinal directions.

Upwind schemes on the other hand differentiate between upstream and downstream effects, i.e., the flow directions (Blazek, 2015, ch. 3). There are several variants of upwind schemes which are described as follows:

First Order Upwind (FOU) scheme uses a value from single upstream cell. The values at cell faces are ascertained assuming the value at the cell center hold throughout the cell (Equation 3.10).

$$\phi_e = \begin{cases} \phi_P, & \text{if } F_e > 0 \\ \phi_E, & \text{if } F_e < 0 \end{cases} \quad (3.10)$$

where, F_e is the flux at face labelled e .

Power-Law (POW) scheme is a variant of FOU where, the diffusive term is reduced for the flows in which the convection is dominant, with the reduction factor, f given by:

$$f = (1 - 0.1|Pe|)^5 \quad (3.11)$$

where, Pe is the *Peclet* number, which is the ratio of convective to diffusive fluxes and the value of f ranges from 0 – 1 (Olsen, 2017, ch. 5).

Second Order Upwind (SOU) scheme uses values from two upstream cells and are more accurate with less false diffusion compared to FOU (Olsen, 2017, ch. 6). The scheme calculates the face value by linear interpolation. Equation (3.14) is only valid if cells are of equal sizes. For a grid where cell sizes differ, i.e., if the expansion ratio is other than unity, Equation (3.12) is applied (modified from Ferziger et al., 2020, ch. 4).

$$\phi_e = \phi_P \lambda_e + \phi_W (1 - \lambda_e) \quad (3.12)$$

where, λ_e is the linear interpolation factor given by:

$$\lambda_e = \frac{x_e - x_W}{x_P - x_W} \quad (3.13)$$

For a uniform grid with equal cell sizes, $\lambda_e = 1.5$ so that the Equation (3.12) takes the form:

$$\phi_e = \frac{3}{2} \phi_P - \frac{1}{2} \phi_W \quad (3.14)$$

Quadratic Upwind Interpolation for Convective Kinetics (QUICK) scheme instead uses quadratic interpolation using a parabola rather than a straight line to find values at cell face (Ferziger et al., 2020, ch. 4).

$$\phi_e = \frac{6}{8} \phi_P + \frac{3}{8} \phi_E - \frac{1}{8} \phi_W \quad \text{if } F_e > 0 \quad (3.15)$$

3.2.4 Temporal Discretization

For time-dependent computations, the governing equations should be discretized with respect to time in addition to space. Temporal discretization can be implicit or explicit depending on the values used from current (t_n) or new (t_{n+1}) time level.

Explicit scheme initiates using a known solution at t_n to compute a new solution at t_{n+1} . The explicit scheme is simple and easy to implement since the new solution is based exclusively on the known values evaluated at earlier time levels. The major disadvantage of the explicit scheme is that the stability of the scheme is limited to certain value of time-step, Δt . The scheme is stable as long as the chosen time-step complies with *Courant-Friedrich-Lewy (CFL)* criteria, which says the time-step should be equal to or smaller than what would be required to transport information across one unit in the spatial discretization scheme. The condition for time-step in 1D is given as (Blazek, 2015, ch. 6):

$$\Delta t = \sigma \frac{\Delta x}{|U|} \quad (3.16)$$

where, σ is the *CFL* number or simply called as *Courant* number, U is the velocity and Δx is the cell size.

Implicit scheme on the other hand uses unknown value at new time level to evaluate the new solution at t_{n+1} . A set of non-linear equations for the unknown variables appear as a result of implicit operation, which need to be solved at each time-step. The storage requirement is higher compared

to that for explicit scheme (Ferziger et al., 2020, ch. 6). However, implicit scheme offers possibility of using a larger time-step producing an improved efficiency while moving towards a steady-state solution (Ferziger et al., 2020, ch. 6) and produce more stable solution (Olsen, 2017, ch. 3).

3.3 Numerical Modelling of Hydraulics

3.3.1 Navier-Stokes Equations

The Navier-Stokes equations are a set of non-linear second-order differential equations (Ferziger et al., 2020, ch. 1), used to compute the water velocity, U . The equations are derived based on the equilibrium of forces acting on an infinitesimal small volume of water in laminar flow:

$$\frac{\partial U_i}{\partial t} + U_j \frac{\partial U_i}{\partial x_j} = \frac{1}{\rho} \frac{\partial}{\partial x_j} \left(-P \delta_{ij} + \rho \nu \left(\frac{\partial U_i}{\partial x_j} + \frac{\partial U_j}{\partial x_i} \right) \right) \quad (3.17)$$

where, P is the pressure, ν is the kinematic viscosity, ρ is the density of water, x is the spatial geometrical variable, δ_{ij} is the Kronecker delta, which is 1 for $i = j$ and 0 for $i \neq j$.

For a turbulent flow, where the flow behaviour is random and chaotic, it is not economical to describe the motion of each and every fluid particles. Instead, the instantaneous velocity, U^t is decomposed into steady time-averaged value, U with a fluctuating value $u(t)$, so that: $U^t = U + u(t)$. This is known as *Reynolds decomposition* (Versteeg and Malalasekera, 2007, ch. 3).

Inserting these variables in the Navier-Stokes equation for laminar flow (Equation 3.17) and some manipulations and simplifications after, would result in Navier-Stokes equation for turbulent flow. The resulting equations governing the average velocity are known as Reynolds-averaged Navier-Stokes (RANS) equations, (Rodi, 2017):

$$\frac{\partial U_i}{\partial t} + U_j \frac{\partial U_i}{\partial x_j} = \frac{1}{\rho} \frac{\partial}{\partial x_j} (-P \delta_{ij} - \rho \overline{u_i u_j}) \quad (3.18)$$

Owing to the non-linearity on the second term on the left side in Equation (3.17) describing the convection, the decomposition and averaging process ends up with additional terms related to fluctuating velocities $\overline{u_i u_j}$. These behave as stresses on fluid in addition to the viscous stresses and are known as the *Reynolds stresses* (Rodi, 2017).

These stresses are modelled often with *Boussinesq's approximation* (Equation 3.19) (Olsen, 2017, ch. 6). According to Rodi (2017), Boussinesq used artificially introduced viscosity called turbulent or eddy viscosity, ν_T instead of molecular viscosity. Eddy viscosity, however, is not a fluid property and it depends on the local turbulence, which is unknown so, the value should be ascertained with the turbulence model.

$$-\rho \overline{u_i u_j} = \rho \nu_T \left(\frac{\partial U_i}{\partial x_j} + \frac{\partial U_j}{\partial x_i} \right) - \frac{2}{3} \rho k \delta_{ij} \quad (3.19)$$

where, k is the turbulent kinetic energy.

Inserting Equation (3.19) in Equation (3.18) and rearranging the terms:

$$\frac{\partial U_i}{\partial t} + U_j \frac{\partial U_i}{\partial x_j} = \frac{1}{\rho} \frac{\partial}{\partial x_j} \left(- \left(P + \frac{2}{3} k \right) \delta_{ij} + \rho \nu_T \frac{\partial U_i}{\partial x_j} + \rho \nu_T \frac{\partial U_j}{\partial x_i} \right) \quad (3.20)$$

The Equation (3.20) is composed of five different terms: a transient and a convective term on the left side, whereas a pressure/kinetic, a diffusive and a stress term on the right side.

3.3.2 Turbulence Model

According to Versteeg and Malalasekera (2007, ch. 3), it is necessary to develop turbulence models to ascertain the Reynolds stresses and scalar transport terms to be able to calculate the turbulent

flows with the RANS equations. The turbulence model to be suitable in a general-purpose CFD should have extensive applicability, be accurate, simple and economical for computation. The common RANS turbulence models are categorized based on the number of transport equations to be solved in addition to RANS flow equation.

Zero-equation model or algebraic model is the simplest turbulence models and use constant eddy viscosity prescribed empirically or through calibration before being used. The first model that described the eddy viscosity distribution over the flow field is the Prandtl's *mixing-length* model, which relates eddy viscosity to mean velocity gradient, $\partial U/\partial y$ and mixing length, l_m expressed as:

$$\nu_T = l_m^2 \left| \frac{\partial U}{\partial y} \right| \quad (3.21)$$

The model though simple and robust, cannot account for the transport and history effects of the turbulence. Besides, prescribing l_m is problem dependent and difficult for situations with complicated geometry (Rodi, 2017).

One-equation model attempts to account for the transport and history effects of turbulence by solving one additional transport equation thereby improving the turbulent flow predictions. The characteristic turbulence quantity involved in the transport equation can be either the turbulent kinetic energy, k or the eddy viscosity, ν_T . The *Spalar-Allmaras* model is one of the well known one-equation models which uses transport equation for eddy viscosity and is popular in aerospace applications (Rodi, 2017).

Two-equation model is the simplest model that neither need prescription of the length scale nor any other turbulence quantity. The model solves two additional equations for determining turbulent kinetic energy, k and length scale, L . The second equation should not necessarily require L itself and instead can be represented in other forms (Rodi, 2017).

The most popular two-equation model is the $k - \varepsilon$ model, where the length scale is incorporated by the dissipation rate, ε as:

$$\varepsilon = \frac{k^{3/2}}{L} \quad (3.22)$$

The $k - \varepsilon$ model computes eddy viscosity as:

$$\nu_T = c_\mu \frac{k^2}{\varepsilon} \quad (3.23)$$

The turbulent kinetic energy, k is defined as:

$$k = \frac{1}{2} \overline{u_i u_j} \quad (3.24)$$

and modelled as:

$$\frac{\partial k}{\partial t} + U_j \frac{\partial k}{\partial x_j} = \frac{\partial}{\partial x_j} \left(\frac{\nu_T}{\sigma_k} \frac{\partial k}{\partial x_j} \right) + P_k - \varepsilon \quad (3.25)$$

where, P_k is the production of turbulence, expressed as:

$$P_k = \nu_T \frac{\partial U_j}{\partial x_i} \left(\frac{\partial U_j}{\partial x_i} + \frac{\partial U_i}{\partial x_j} \right) \quad (3.26)$$

While, the dissipation rate, ε is modelled as:

$$\frac{\partial \varepsilon}{\partial t} + U_j \frac{\partial \varepsilon}{\partial x_j} = \frac{\partial}{\partial x_j} \left(\frac{\nu_T}{\sigma_\varepsilon} \frac{\partial \varepsilon}{\partial x_j} \right) + C_{\varepsilon 1} \frac{\varepsilon}{k} P_k + C_{\varepsilon 2} \frac{\varepsilon^2}{k} \quad (3.27)$$

where, $c_\mu = 0.09$, $C_{\varepsilon 1} = 1.44$, $C_{\varepsilon 2} = 1.92$, $\sigma_k = 1.0$ and $\sigma_\varepsilon = 1.3$.

The $k - \varepsilon$ model can be utilized in wide variety flows without calibration because of the universal constants. However, this may not be the case for river engineering where bed friction influences the flow field. The roughness needs to be calibrated against the velocity measurement (Olsen, 2017, ch. 6). Besides, the accuracy decreases for flows with adverse pressure gradient (Blazek, 2015, ch. 7).

The $k - \omega$ model, another variant of two-equation model, instead of ε uses the turbulence frequency, ω that incorporates the length scale as:

$$\omega = \frac{k^{1/2}}{L} \quad (3.28)$$

Rodi (2017) mentions that the $k - \omega$ model proposed by Wilcox shows better performance in flows with adverse pressure gradients and does not need damping functions near walls. However, the model is extremely sensitive to the boundary conditions at free-stream boundaries. *Menter SST* model on the other hand, blends these two models such that $k - \varepsilon$ model is active away from the walls and $k - \omega$ model is active near the walls together with the introduction of a shear stress limiter.

Apart from the models described earlier, there exist several more-advanced turbulence models which can model the anisotropic turbulence.

Reynolds Stress Model (RSM) also called the *second-order* or *second-order closure model* is the most complex of the classical turbulence models. While modelling flows with complex strain fields or significant body forces, the $k - \varepsilon$ model encounters several drawbacks. Though the kinetic energy is calculated accurately, the Reynolds stresses are not properly represented. On the contrary, RSM can ascertain the directional effects of the Reynolds stress field through the exact Reynolds stress transport equation. RSM solves six partial differential equations, one for each Reynolds stress together with the equation for dissipation rate ε . So, the computational requirement is substantially higher compared to that for $k - \varepsilon$ model. Also, RSMs have not been validated as widely as $k - \varepsilon$ model (Versteeg and Malalasekera, 2007, ch. 3).

Algebraic Stress Model (ASM) attempts to address the anisotropy of Reynolds stresses economically without solving of transport equations to the full length. The partial differential equations defining the Reynolds stress transport are reduced to algebraic equations, which are solved in conjunction with k and ε equations. In RSM, the gradients of Reynolds stresses are present in convective and diffusive terms, which demand significant computational resources. Neglecting the convection and diffusion terms may appear reasonably accurate in some cases. However, a more general procedure assumes the sum of the convective and diffusive terms of Reynolds stresses to be proportional to the sum of the convective and diffusive terms of the turbulent kinetic energy (Versteeg and Malalasekera, 2007, ch. 3).

Direct Numerical Simulation (DNS) develops a transient solution on an adequately fine grid with sufficiently small time-steps to solve even the smallest eddies and the fastest variations (Versteeg and Malalasekera, 2007, ch. 3). The application of DNS is restricted only to a relatively simple flow conditions with low Reynolds number, Re in the range of $10^4 - 10^5$ (Blazek, 2015, ch. 7). DNS requires extremely large number of grid points for enough spatial resolution $N \propto Re^{9/4}$ (Versteeg and Malalasekera, 2007, ch. 3).

Large Eddy Simulation (LES) instead of time-averaging, utilizes spatial filtering procedure to distinguish the larger and smaller eddies. The operation initiates with a suitable filtering function and a fixed cutoff width aiming to resolve only those eddies with length scale exceeding the cutoff width. LES requires high grid resolution both in stream-wise and crossflow direction. Although computationally intensive, LES requires substantially less computational effort compared to DNS (Blazek, 2015, ch. 7).

3.3.3 The SIMPLE Method

According to Ferziger et al. (2020, ch. 7), the solution of Navier-Stokes equations is complicated due to the absence an independent equation for pressure. In the case of compressible flow, density is a dominant variable in the mass conservation equation, which is not the case with the incompressible flow where the density is constant. Hence, the mass conservation equation becomes a kinematic constraint of the velocity field rather than a dynamic equation. Since only the pressure gradient, not the absolute pressure itself, influences the incompressible flow, it is possible to solve the problem by establishing a pressure field satisfying the continuity equation.

The SIMPLE algorithm is the most commonly used approach to solve the pressure field. SIMPLE stands for Semi-Implicit Method for Pressure Linked Equations. The basic principle is to make an initial guess for pressure, which does not satisfy the continuity and then use the continuity defect to attain formula for the pressure correction. Water continuity is satisfied when pressure correction is added.

In the following text to derive the equations for pressure correction, the initial uncorrected variables are denoted with an index * and the correction variables is denoted with an index '. The corrected variables are free of superscripts. The correction equations can be written as:

$$P = P^* + P' \quad (3.29)$$

$$U_k = U_k^* + U_k' \quad (3.30)$$

where, P and U are the pressure and velocity, respectively and the index k on the velocity refers to the direction, and ranges from 1 to 3 in 3D computations.

Navier-Stokes equations for guessed values for the pressure can be discretized as:

$$a_p U_{k,p}^* = \sum_{nb} a_{nb} U_{k,nb}^* + B_{u_k} - \left(A_k \frac{\partial P^*}{\partial \xi} \right) \quad (3.31)$$

where, a_p and a_{nb} are the weighing factors resulting from discretization, B_{u_k} consists of the terms other than convective, diffusive and pressure terms, A_k is the the cell surface area in direction k and ξ is the index for the grid, which is unity for two adjacent cells.

Likewise, for the corrected variables:

$$a_p U_{k,p} = \sum_{nb} a_{nb} U_{k,nb} + B_{u_k} - \left(A_k \frac{\partial P}{\partial \xi} \right) \quad (3.32)$$

Subtracting Equation (3.32) from Equation (3.31) and using Equations (3.29) and (3.30), the equation for velocity correction can be expressed as (Olsen, 2017, ch. 6):

$$U_k' = - \left(\frac{A_k}{a_p} \frac{\partial P'}{\partial \xi} \right) \quad (3.33)$$

The first term on the right side of Equation (3.32) is avoided as simplification. The SIMPLEC (SIMPLE-Consistent) method instead utilizes the following expression:

$$U_k' = - \left(\frac{A_k}{\left(a_p - \sum_{nb} a_{nb} \right)} \frac{\partial P'}{\partial \xi} \right) \quad (3.34)$$

To calculate the pressure correction, the continuity equation can be used, where the water fluxes passing through each cell side are added:

$$\sum_{nb} A_k U_k = \sum_{nb} A_k U'_k + \sum_{nb} A_k U_k^* = 0 \quad (3.35)$$

$\sum_{nb} A_k U_k^*$ represents the continuity deficit in a cell from the previous time-step and the other term is obtained from Equation (3.33).

Considering each side of the cell, an equation where only the pressure correction is unknown can be obtained as (Olsen, 2017, ch. 6):

$$a_p^\circ P'_p = \sum_{nb} a_{nb}^\circ P'_{nb} + b \quad (3.36)$$

where, b refer to the continuity deficit from the guessed velocity field and the index $^\circ$ is used to denote the new set of weighing coefficients.

The procedure is:

1. Guess a pressure field P^*
ITERATE
2. Solve Equation (3.31) to obtain velocity, U^*
3. Solve Equation (3.36) to obtain pressure correction, P'
4. Correct the pressure using Equation (3.29)
5. Compute velocity correction from Equation (3.33)
6. Correct velocity using Equation (3.30)
UNTIL convergence

The SIMPLE method moves slower towards convergence compared to the SIMPLEC method since the velocity correction is smaller for SIMPLE (Equation 3.33) than for SIMPLEC (Equation 3.34). There exist other improved versions involving more correction steps like SIMPLER (SIMPLE-Revised) and PISO (Pressure Implicit with Splitting of Operators).

3.3.4 Free Surface Algorithms

In an open channel flow, where water surface is present it is necessary to determine the position of free surface. According to Ferziger et al. (2020, ch. 13), free surface flows represent a difficult class of flows with moving boundaries, whose initial position is known and the changed location at later times needs to be ascertained as a part of the solution . The free surface is an air-water boundary in most usual cases; however, liquid-gas and liquid-liquid interfaces also occur. The Navier-Stokes equations need special algorithms for tracking the changes of water surface in space and time (Erdbrink et al., 2014). There exist different algorithms for computing free surface in 3D, which can be categorized based on whether an adaptive grid is used or not (Olsen, 2018, ch. 6).

Fixed grid algorithms

The fixed grid algorithms generally compute a two-phase flow with air and water and determine the position of the boundary within the grid. Some cells will be full of either water or air, and the rest of the cells will be partially filled with water and air.

Volume of Fluid (VOF) method is one of the most used fixed grid algorithms. The method is based on the volume fraction occupied by water, F defined as:

$$F = \frac{V_w}{V_a + V_w} \quad (3.37)$$

where, V_w and V_a represent the volume of water and air in a cell, respectively. The value of F will be 1 when the cell is full of water and 0 when a cell is full of air. The ratio is calculated by solving a

convection-diffusion equation:

$$\frac{\partial F}{\partial t} + U_i \frac{\partial F}{\partial x_i} = \frac{\partial}{\partial x_i} \left(\Gamma \frac{\partial F}{\partial x_i} \right) \quad (3.38)$$

where, Γ is the diffusion coefficient. The position of the free surface is determined based on the values of F in every cell.

Level Set method is another much preferred method. It solves the equation for distance, L to the water surface instead of volume fraction. The convection equation for this distance is expressed as:

$$\frac{\partial L}{\partial t} + U_i \frac{\partial L}{\partial x_i} = 0 \quad (3.39)$$

It is simpler to compute the free surface with level set method compared to that with VOF method.

Marker and Cell method on the other hand follows the motion of massless particles introduced at the initial time to determine the free surface (Ferziger et al., 2020, ch. 13).

Adaptive grid algorithms

Adaptive grid algorithms are able to adjust the grid such that the free surface is aligned with top of the cells. The free surface is initialized first and the algorithm calculates the changes in the free surface. The grids are then adjusted accordingly in small steps to avoid instabilities. All the cells will always be filled with water thereby avoiding the wastage of cells. Hence, the method requires less number of cells than fixed grid algorithms. While the fixed grid algorithms suffer inaccuracies with partially filled cells, adaptive grids do not have such problems. Besides, the method reduces false diffusion as the grid near surface are aligned with the flow. However, the method can be more unstable than the fixed grid algorithms (Olsen, 2017, ch. 6).

The adaptive grid algorithms can be divided based on the equation used to compute the changes in water levels. One method utilizes the *continuity* equation in cells close to free surface. The pressure in these cells are assigned by linear interpolation between cells underneath and zero water pressure at the free surface instead of using the SIMPLE method. This results in water continuity not being satisfied in surface cells. The water continuity defect, ΔQ is computed from the water fluxes in and out of the cell. The defect is then utilized to determine the change in water level, Δz with the equation (Olsen, 2015):

$$\Delta z = \frac{\Delta Q \Delta t}{A_z} \quad (3.40)$$

where, Δt is the time-step and A_z is the horizontal projected area of the cell. As the gravity is included as source term in this approach, the solution may be unstable and extremely short time-step is needed. The method is therefore not suitable for simulations of long time scale.

Another method uses *energy* equation to calculate the changes in water surface. The computed pressure is utilized to compute the water surface elevation, z_p in surface cell indexed p with reference to the water surface elevation in adjacent cell, indexed i as (Olsen, 2015):

$$z_p = z_i + \frac{(P_p - P_i)}{\rho g} \quad (3.41)$$

where, P is the pressure computed using the SIMPLE method while solving Navier-Stokes equations. The method is very stable and allows the use of long time-steps. However, the pressure at the surface should be hydrostatic, and hence the method is unsuitable for computing very steep surface slopes (Olsen, 2017, ch. 6).

3.3.5 Boundary Conditions

Model for numerical simulation can represent only a portion of the whole physical system. Artificial boundaries arise when the real physical domain is curtailed to form a smaller domain, so values have

to be prescribed for some physical quantities, including those for natural boundaries like walls and water surfaces. Boundary conditions should be set properly to simulate precisely the physical system (Blazek, 2015, ch. 8). A division into four parts is considered as follow (Olsen, 2017, ch. 6):

Inflow

Dirichlet boundary conditions, i.e., values for all flow variables should be given at inflow boundary. Velocities may be set based on logarithmic profile. Shear stress can be estimated using the velocity at the inlet bed, which then can be used to determine, turbulent kinetic energy, k using Equation (3.42) and the value for dissipation rate, ε can be calculated using Equation (3.43).

$$k = \frac{\tau}{\rho \sqrt{C_\mu}} \quad (3.42)$$

$$\varepsilon = c_\mu \frac{k^2}{\nu_T} \quad (3.43)$$

where, C_μ is a constant equal to 0.09, τ is the bed shear stress, ρ is the density of water and ν_T is the eddy viscosity.

Outflow

Zero-gradient boundary conditions can be applied for all the variables at the outlet boundary. The flow variables at the outflow are assumed to have the same values as in the nearest preceding cells such that the gradient equals zero.

Water Surface

Symmetrical boundary conditions are applied for velocity at surface, which refers to the use zero-gradient conditions in defining velocity in horizontal direction and zero water flux criteria for determining velocity in vertical direction. Zero-gradient boundary conditions are applied for ε and turbulent kinetic energy is set to zero.

Bed and Wall

No boundary conditions are provided for bed and wall since the flux through them is zero. However, a wall law, Equation (3.44) may be used for both for velocities and and turbulence parameters. The use of wall law can avoid the need of greater number of cells to dissolve the steep flow gradient towards the wall.

$$\frac{U}{u_*} = \frac{1}{\kappa} \ln \left(\frac{30y}{k_s} \right) \quad (3.44)$$

where, U is the flow velocity, u_* is the shear velocity, k_s is the roughness, κ is a constant equal to 0.4 and y is the distance from wall to cell centre.

3.4 Numerical Modelling of Sediment Transport

Sediment transport is conventionally categorized into bed load and suspended load. This distinction is often used while simulating sediment transport since the transport processes are different.

3.4.1 Bed Load

Bed load may be computed using different formulae, for an instance van Rijn formula (Olsen, 2017, ch. 9):

$$\frac{q_b}{d_{50}^{1.5} \sqrt{\frac{(\rho_s - \rho_w)g}{\rho_w}}} = 0.053 \frac{\left[\frac{\tau - \tau_c}{\tau_c} \right]^{2.1}}{\left\{ d_{50} \left[\frac{(\rho_s - \rho_w)g}{\rho_w \nu^2} \right]^{1/3} \right\}^{0.3}} \quad (3.45)$$

where, q_b is the sediment transport rate per unit width, d_{50} is the average sediment particle diameter, τ represents the bed shear stress, τ_c is the critical shear stress to move the sediment particles, ρ_s and

ρ_w are, respectively, the densities of sediments and water, ν represents the kinematic viscosity and g is the acceleration due to gravity. Other formulae for computing bed loads include Meyer-Peter and Müller formula, Einstein formula, etc.

3.4.2 Suspended Load

The suspended load is computed by solving transient convection-diffusion equation (Equation 3.46) for the sediment concentration. The first term on the left side in Equation (3.46) is the transient term, while the second term represents the convection of sediments, i.e., transport of sediments due to velocity of water. The third term, considered as an extra term on the left side refers to the falling of the sediments in the vertical direction. The first right-hand term is the diffusion of sediments that refers to the mixing due to turbulence in water.

$$\frac{\partial c}{\partial t} + U_j \frac{\partial c}{\partial x_j} + w \frac{\partial c}{\partial z} = \frac{\partial}{\partial x_j} \left(\Gamma \frac{\partial c}{\partial x_j} \right) + S \quad (3.46)$$

where, U is the flow velocity, w is the fall velocity, Γ is the diffusion coefficient, c is the sediment concentration over time, t and spatial geometrical directions, x and z . S is the source term that is assigned with the sediment pick-up rate due to bed erosion. Alternatively, the resuspension of sediments can be modelled by using van Rijn's formula (Equation 3.47) for equilibrium concentration near the bed that serves as the boundary condition close to the bed (Olsen, 2017, ch. 9).

$$c_{bed} = 0.015 \frac{d_{50}}{a} \frac{\left[\frac{\tau - \tau_c}{\tau_c} \right]^{1.5}}{\left\{ d_{50} \left[\frac{(\rho_s - \rho_w)g}{\rho_w \nu^2} \right]^{1/3} \right\}^{0.3}} \quad (3.47)$$

where, c_{bed} is the concentration of suspended load at bed, a refers to the reference level set equal to the roughness height. Using Equation (3.47), it is possible to simulate interaction between sediments moving in suspension and close to the bed (Olsen and Skoglund, 1994). However, when bed cells are prescribed with the concentration calculated using Equation (3.47), there will be sediment continuity defect in the bed cell. The continuity defect may be utilized to compute bed changes as a function of erosion and deposition of sediments through a time-dependent simulation.

3.4.3 Non-uniform Sediments

There exist several sediment transport formulae and many of them are intended for sediment with uniform distribution, i.e., the sediments with comparable sizes. However, combination of coarse and fine particles occur in natural river. A non-uniform sediment distribution is taken into account by dividing the sediments into several fractions based on their sizes for numerical modelling. Separate sediment transport formula and convection-diffusion equation are utilized to model each size fraction. Besides, interaction at bed should be well considered. The influence of variable sizes on sediment transport capacity is realized by multiplying transport rate, q_{s0} obtained from transport formula with fraction, f of each size (Olsen, 2017, ch. 9):

$$q_s = q_{s0} f \quad (3.48)$$

where, q_s is the sediment transport rate per unit width. In addition, larger particles may obstruct the motion of the tiny particles hiding behind them. The impact of this process is included by using hiding/exposure formula, whereby Shield's parameter is modified using a parameter, ξ_i for i^{th} fraction given by:

$$\xi_i = \left(\frac{d_i}{d_{50}} \right)^{-0.3} \quad (3.49)$$

where, d_i is the sediment particle diameter corresponding to i^{th} fraction.

3.5 Errors and Uncertainties in CFD

CFD involves discretization while solving the governing equations, which yield approximate results. Moreover, due to the complex fluid flow processes, sometimes partially explained by the mathematical equations, the equations may not often truly represent the real-world physical processes. The European Research Community on Flow, Turbulence and Combustion (ERCOTAC) published Best Practice Guide, which classifies CFD errors as (Olsen, 2017, ch. 6):

1. Model errors and uncertainties
2. Discretization or numerical approximation errors
3. Errors due to not complete convergence
4. Round-off errors
5. Errors in boundary conditions and input data
6. User errors due to inexperience
7. Bugs in the software

3.6 Significance of Model Studies in Headworks

Hydraulics models are being used for the planning and design of different hydraulic components of civil engineering works in rivers, including coastal and offshore structures. The application of hydraulic models become crucial for two reasons. The first reason is the complex nature of turbulent flow in natural water-courses, which cannot be addressed with prevailing empirical formulae, the use of which is constrained for simple cases like for straight channels or pipes. Natural water-courses and the structures generally have complex geometry that includes constrictions, expansions, diversions, varying gradients, etc. Empirical formulae for such instances can only yield approximate results inappropriate for optimizing the design. The second reason is the requirement of performance evaluation of the structures for different flow situations that are likely to occur during the lifetime of the project. The structures need to perform under a wide range of circumstances like normal flow, floods, ice formations, sediment deposition and erosion. These conditions should be investigated before the construction to ensure efficient functioning. At the same time, model studies provide plenty of opportunities to optimize the design thereby minimizing the economic and environmental impacts (Lysne et al., 2003, ch. 10).

Typical problems studied in models may include: overall configuration of dam, gates and intakes, backwater effects under different flow conditions, spillways and sluices capacities, stilling basin design, calibration of dam gates and sluices for operational purpose, operation of gates and intake controls for various discharges and production scenarios, design of intake to reduce vortices, passing of ice or trashes, fish ladder location and performance, sediment buildup and exclusion at reservoirs and intake ponds, river bed changes and local bed changes around the structures, flushing and diversion of sediment, design and operation of sediment excluders (Lysne et al., 2003, ch. 10).

Furthermore, Isaac and Eldho (2016) pointed out the importance of verification of performance of different components through model studies since the design and operation of the projects are highly site-specific due to diverse topography, geology, hydrology and sediment characteristics. The authors also mentioned that the prediction of sediment deposition pattern in the reservoir is required for determining the optimal invert level of the intake, reservoir life and flushing frequency during planning and designing stage.

The problems mentioned above mostly pertain to headworks; however, the model studies are not limited only to headworks with several other potential applications.

3.7 Relevant Works

Olsen and Skoglund (1994) developed a 3D model using SSIIM for simulating hydraulics and sediment transport in settling basin and verified the model results with that of physical model for both water flow field and sediment concentrations. The model was used to estimate the trap efficiency of the sand trap with varied number of grids and discretization schemes. The authors concluded that the accuracy of 3D numerical model is high enough and can be used for designing, despite the recirculation zone was not replicated accurately with standard $k - \epsilon$ model.

Olsen and Kjellesvig (1999) modelled the tunnel type sand trap of Svartisen Hydropower Project (Norway) considering movable bed and computed the bed changes in sand trap. The resulting bed profiles complied well with the measurements from physical model test. They further found from the sensitivity test that the results were more sensitive to roughness of fixed boundaries and less sensitive to the formula for concentration at the bed.

Nøvik et al. (2014) investigated the settling basin of Lower Manang Marsyandi Hydropower Project (Nepal) that included physical as well as 3D numerical modelling in STAR-CCM+ to assess the trap efficiency based on CFD simulation without the use of sediments. The simulation satisfactorily replicated the velocity field at the downstream part while greater deviations were observed at the upstream part of the basin. Besides, the simulation qualitatively reproduced the decrease in turbulent kinetic energy. The results from CFD were utilized to adjust and improve the input parameters used in conventional analytical approaches for calculating trap efficiencies, which yielded slightly decreased values compared to that given with unadjusted parameters. They further concluded that CFD models can serve valuable information to the standard approaches for trap efficiency computation and evaluation of settling basin performance.

Rüther et al. (2005) used SSIIM to compute water velocity and suspended sediment transport in Kapunga (Tanzania) water intake, including the performance of intake by means of performance ratio, which is analogous to trap efficiency in case of a settling basin (as seen from the formula). The computed results showed a good correspondence with measured data. Sensitivity tests were carried out with different grid numbers and discretization schemes, which showed fine grids with second order discretization yielded the best results.

Haun and Olsen (2012) modelled the reservoir flushing for Angostura reservoir (Costa Rica) in a prototype scale with SSIIM and tested the results with the field measurements. They successfully simulated the amount of sediments eroded and formation of flushing channel, however, with deviations in channel widths. They further concluded that 3D model can predict the deposition and erosion of suspended load more accurately compared to 2D model, including the flow features where the velocity profile is non-logarithmic.

Chapter 4

Kali Gandaki A Hydropower Plant

4.1 Introduction

The *Kali Gandaki* river is one of the major rivers of Nepal. The river is characterized by its deep gorges through Himalayas and massive hydroelectric potential. With a total catchment area of $46,300 \text{ sq. km}$, it accommodates three of the world's highest mountains over $8,000 \text{ masl}$, namely *Dhaulagiri I*, *Manaslu* and *Annapurna I*.

Kali Gandaki A Hydropower Plant (KGA) located in western Nepal, is a peaking ROR project with an installed capacity of 144 MW , annually generating about 842 GWh of electrical energy utilizing a net head of 115 m . Commissioned in 2002, it is the largest hydropower project till date in Nepal. The main components of the project are located at *Syangjha* district and also partly includes *Palpa*, *Parbat*, *Gulmi*, *Kaski* and *Rupandehi* districts. The diversion dam is located about 500 m downstream from the confluence of *Kali Gandaki* river and *Andhi Khola* river, between *Mirmi* and *Harmichaur* villages of *Syangjha* and *Gulmi* districts, respectively. The main components of the project consists of about 110 m long, 43 m high concrete gravity diversion dam, open surface settling basins, 6 km long tunnel of 7.40 m diameter and a surface power house. The dam is equipped with radial gates to operate during sluicing mode and sustain about 3.1 Mm^3 of pondage volume for power peaking. The rated design discharge is $141 \text{ m}^3/\text{s}$, which is fed into three Francis turbines (*Maintenance Field Visit on Kali-Gandaki Hydropower Project*, 2013). The salient features of the plant are listed in Appendix A.



Figure 4.1: Existing headworks of KGA during wet season operation (Biswhwakarma, 2018).

4.2 Arrangement of Headworks

The headworks of KGA include concrete gravity diversion dam with three gated spillway, forebay wall and forebay, intake with sluicing arrangements, settling basins and collector channels. Arrangement of headworks with different components is shown in Figure 4.2, which shows the model of existing headworks with the numbers representing the corresponding components as described in the text below. Also, the Figure B.1, which shows layout plan of the headworks, including the proposed modifications by Hydro Lab can also be referred.

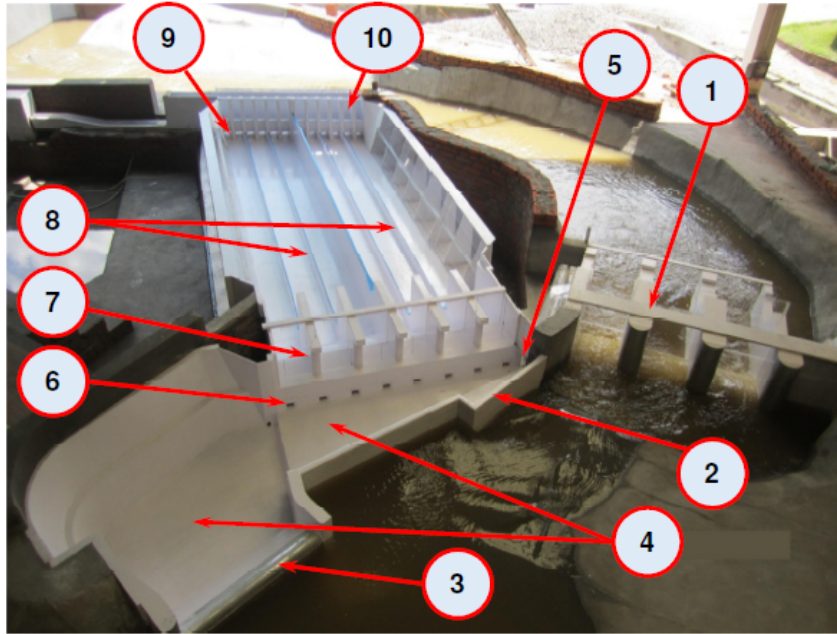


Figure 4.2: Physical hydraulic model of existing headworks (Hydro Lab, 2017). The numbers indicate different structures mentioned in the text.

The dam (1) is 43 m high and about 110 m long equipped with three radial gates and a bascule gate. The crest level of the spillway is at 505.00 masl.

With a crest elevation of 519.00 masl, the dog-legged forebay wall (2) separates the intake flow and the river flow during wet monsoon season allowing the flow pass only through the forebay inlet weir (3). The forebay inlet weir is 36 m long with the crest at elevation 515.00 masl. The forebay floor (4) is at two different levels; 502.00 masl after inlet weir and 506.00 masl before intake. There are eight under sluices (6) below intakes and a forebay flushing gate (5) opening into the river. The forebay is followed by six gated intakes (7) opening into six bays in the settling basins. Hence, the intake can be considered as the inlet for settling basins. The sill level of the intake is at 514.00 masl.

The settling basins (8) are open surface type, trapezoidal in plan with intermittent flushing and consists of two basins each with three bays. The top width of each basin is 40 m and the average length is about 174 m (measured along the midway of the settling basins after the inlet transition). The floor of the basin is at 504.00 masl. The basin has a 15 m high divider wall in the middle and 4 m high two guide walls in each basin. There are 12 flushing gates (9) and 12 collector channel gates (10) with sill levels at 504.00 masl and 514.50 masl, respectively at the end of settling basins.

4.3 Hydrology and Sedimentology

With a catchment area 7,618 sq. km at dam site, the average annual flow is 288 m³/s and the average monsoon flow (June-October) is 597 m³/s. The highest flood recorded in Kali Gandaki river is about 4,500 m³/s in past 100 years while the minimum flow is about 40 m³/s (Chhetry and Rana, 2015).

The daily discharges and sediment concentration for the years 2016, 2017 and 2018 are shown in Figure 4.3.

Like any other major rivers in Nepal, Kali Gandaki initiating from the great Himalayas has high sediment loads. The major reasons behind excessive quantities of sediments are irregular geographical terrain, steep relief, presence of soft, weak and newly formed sedimentary rocks and high monsoon rainfall. The sediment concentration ranges from 20 ppm (0.02 kg/m^3) during dry winter season to as high as 50,000 ppm (50 kg/m^3) during wet monsoon season, with an average of 750 ppm as observed at the plant (Koirala et al., 2016).

According to the case study collated by International Hydropower Association (IHA, 2017), the river carries a suspended load of 43 Mt/yr, of which nearly one-fourth are sand particles highly laden with abrasive angular quartz mineral. About 95% of this amount is transported during monsoon season. As seen in Figure 4.3, the suspended sand concentration escalates from early June and gradually decreases from October in a normal year.

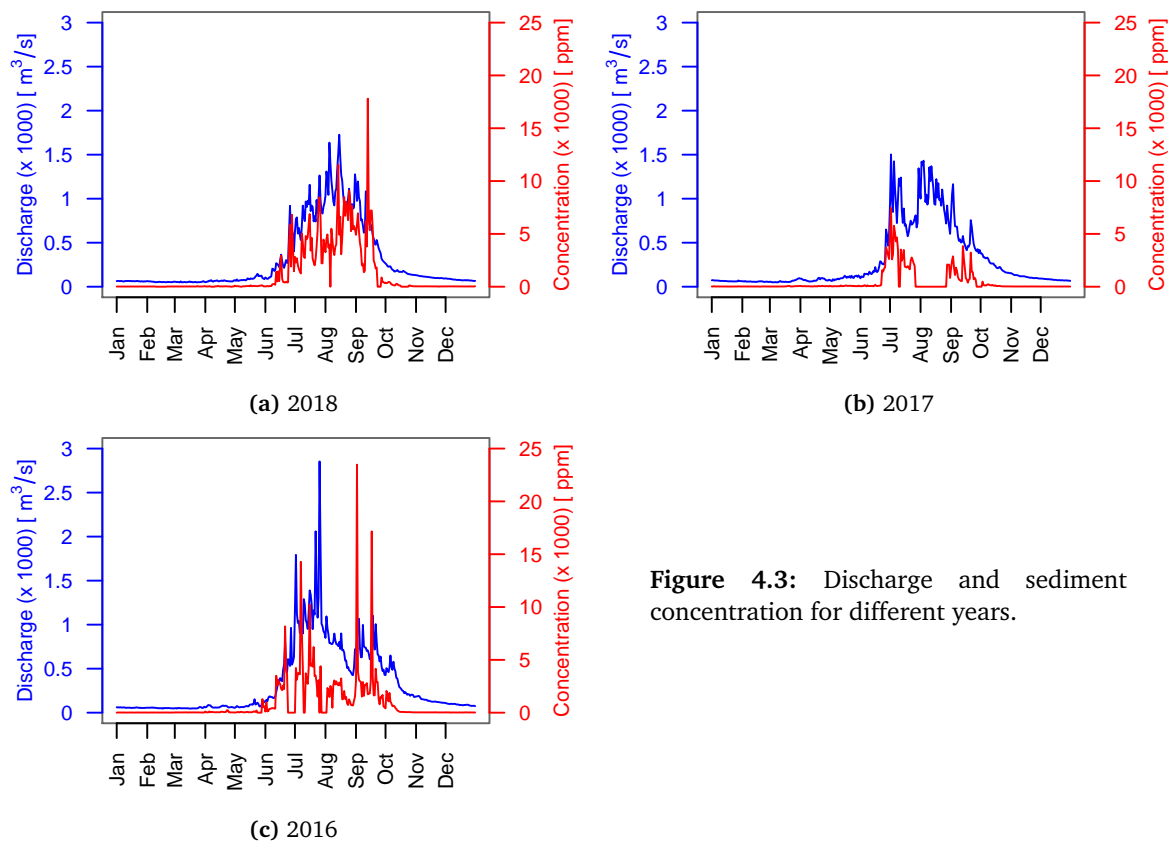


Figure 4.3: Discharge and sediment concentration for different years.

The particle size distribution (PSD) of the suspended sediments, as obtained from the sediment sampling in the reservoir, is shown in Table 4.1.

Table 4.1 Particle size distribution of suspended sediments.

Particle size [mm]	% Finer
1	99.87
0.71	99.43
0.5	97.93
0.355	94.25
0.125	53.81
0.09	26.76

4.4 Problems in Existing Headworks

The major shortcoming in the existing headworks is the unfavourable approach flow condition towards the intake. The flow over the forebay inlet weir is directed more towards right part (utilizing only 20 – 25% of the total length of the weir) striking straight to the trash rack at the leftmost intake. Owing to this concentrated and skewed flow, recirculation flows are created on the both sides of the forebay (Figure 4.4a). Also, the bascule gate installed for the passage of floating trash is not working efficaciously. Due to the concentrated flow speeding over the forebay inlet weir, the floating debris are drawn towards the intake consequently choking the trash rack which must be scraped out mechanically (Figure 4.4b). The effect of concentrated approach flow is not just limited at the intake, it outspreads even inside the settling basins due to short transition between intake and the settling basins. Recirculation flow and eddies can be observed at inlet and main basins (Figures 4.4c and 4.4d). As observed from the dye tests in physical hydraulic model, flow distributions in the settling basins are non-uniform with higher discharge passing through the basin in left (Biswhwakarma, 2018; Hydro Lab, 2017).

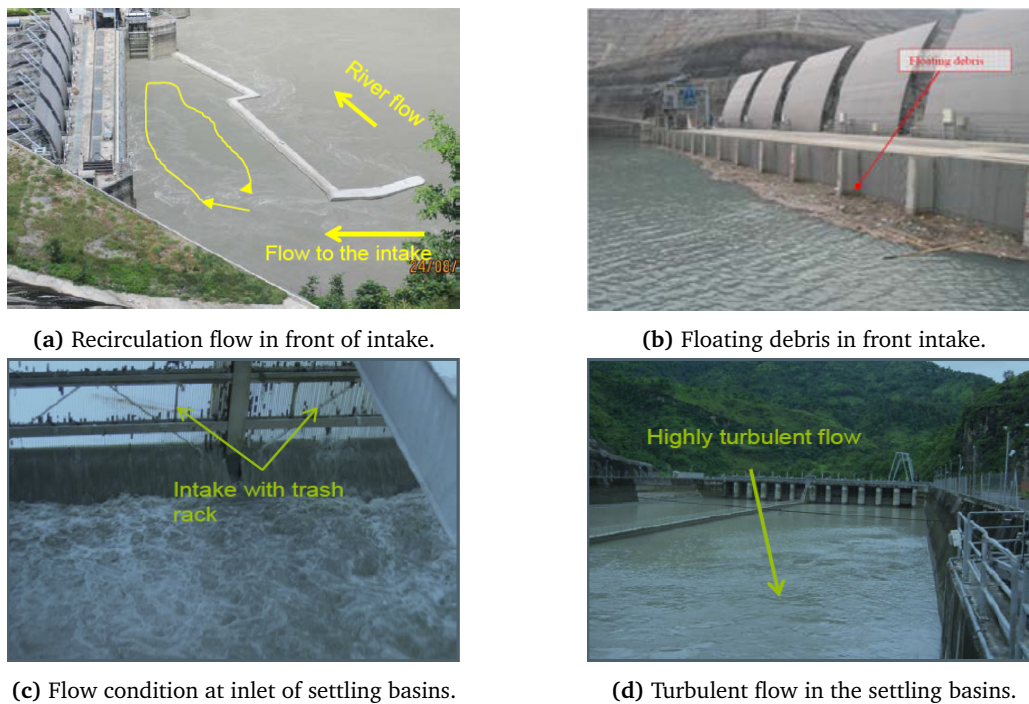


Figure 4.4: Problems in existing headworks at KGA (Biswhwakarma, 2018).

The settling basins were originally designed to settle all of the sediments greater than 0.2 mm, 95% of the sediments greater than 0.15 mm and roughly 70% of the sediments greater than 0.10 mm (Chhetry and Rana, 2015). However, the unfavourable hydraulics due uneven flow distribution in the settling basins, recirculating flow and eddies formation have been hindering the efficient sediment trapping.

Figure 4.5 shows the range of trap efficiencies of the existing settling basins observed in years 2016 to 2018. The efficiencies are computed based on the observed sediment concentrations at the inlet and outlet of the settling basins using Equation (2.14). The data are restricted from mid June to mid October, as the sediment inflows are higher during this period and for the rest of the time the water contains mostly silt and clay particles in a very less quantity. As seen from Figure 4.5, it is clear that the settling basins are not performing efficiently. The median values of efficiencies for years 2018, 2017 and 2016 are 40.32%, 49.41% and 59.66%, respectively considering only sand concentration. These values are as less as 5% if only concentrations of silt and clay are taken into account. Besides,

the plot shows some negative values indicating the intrusion of the settled particles (even for sand) into the flow through the outlet, which can be due to the unfavourable hydraulics in the settling basins.

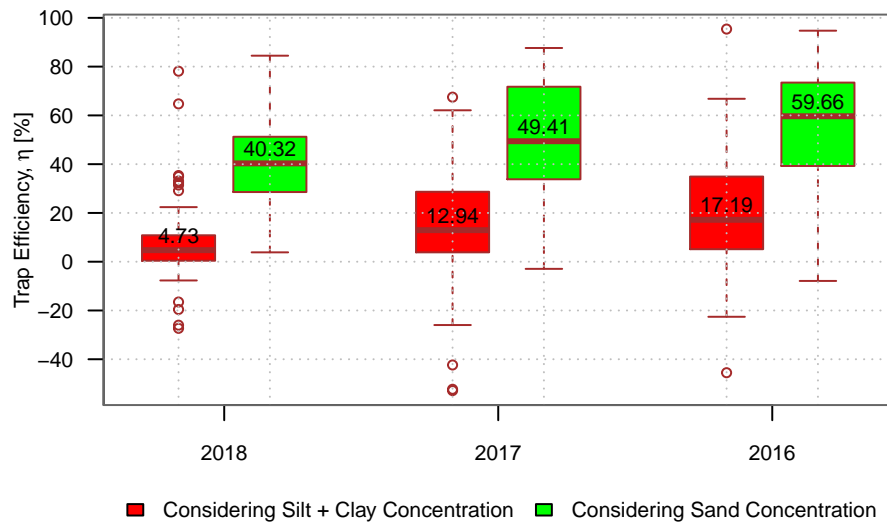


Figure 4.5: Trap efficiencies of existing settling basins in different years, derived from observed sediment concentrations at inlet and outlet of settling basins.

The inefficient functioning of the settling basins can also be realized from the fact that the plant has been facing excessive turbine abrasion since the commercial operation from August 2002. The effect of sediments can be observed in runners, guide vanes, facing plates, labyrinth rings and other under water components (Figure 4.6).



Figure 4.6: Erosion in runner and facing plates (Chhetry and Rana, 2015).

4.5 Physical Hydraulic Model Study and Recommendations

In the view to improve the overall headworks hydraulic performance, including flow patterns in settling basins, physical hydraulic model testing of headworks of KGA was conducted at Hydro Lab, Nepal. The investigation focused also on improving the flow distribution among the chambers of the settling basins and consequently ensure the efficient sediment trapping. The study was carried out in two phases. The first phase was completed in June 2012, which recommended modifications to the existing hydraulic structures. After review of the recommendations, the chief consultant- MWH proposed other alternatives and sought further model tests on the existing model at Hydro Lab. The second phase was completed in February 2017.

The physical hydraulic model of KGA is an undistorted fixed bed model constructed in scale of 1 : 40. It covered up to 800 m of river stretch upstream of the dam for both Kali Gandaki river and Andhi Khola river, while 500 m downstream of the dam. Similarly, it included headworks extending up to collector channel at the end of the settling basins. Bricks, cement, sand and aggregates were used for the construction of the river model, while headworks structures were constructed using waterproof plywood and acrylic materials. The model ratio adopted for different parameters are shown in Table 4.2.

Table 4.2 Model scale ratios used in physical hydraulic model of KGA (Hydro Lab, 2017).

Parameter	Scale ratios in term of L_r	Ratio
Length, L	L_r	1:40
Velocity, U	$L_r^{1/2}$	1:6.32
Time, t	$L_r^{1/2}$	1:6.32
Discharge, Q	$L_r^{5/2}$	1:10,119
Area, A	L_r^2	1:1,600
Volume, V	L_r^3	1:64,000

Five different steady flows ranging from design discharge to a five-years flood (Table 4.3) were simulated in relation to approach flow condition at forebay and into intakes, flow pattern inside the forebay, floating debris transport, flow patterns inside the settling basins at inlet, main basin and outlet. For all the flows, water level inside the settling basins was maintained at 518.00 masl while releasing 141 m³/s into collector channel. Dye and floating objects were employed for visual assessment. Acoustic Doppler Velocimeter (ADV) and Micro-propeller current meter were used for the velocity measurements at settling basins, collector channel gates, intakes gates and along the forebay walls. The model was also tested for the qualitative assessment of flushing efficiency.

Table 4.3 Simulated flows in physical hydraulic model (Hydro Lab, 2017).

Description	Flow at Dam Site [m ³ /s]	Kali Gandaki River [m ³ /s]	Andhi Khola River [m ³ /s]
General test flow	1,200	1,116	84
Design flow	141	132	9
Average monsoon flow (June-October)	597	527	70
1 in 2 years flood	2,260	1,695	565
1 in 5 years flood	2,880	2,020	860

After testing several modifications, the study has recommended following design modifications based on the improved hydraulic performances (Figures 4.7a and 4.7b):

- A 4.5 m high wall on the forebay inlet weir crest provided in two parts; a 25 m long straight wall at the left part of the forebay inlet weir and an oblique transition to the leftmost inlet opening.
- 1 m wide support piers aligned parallel to the intake piers at spacing of 6.30 m c/c over the trimmed forebay wall at 515.00 masl. The arrangement has one support pier along the center line of each intake pier and one support pier in between, with a total of 12 inlet openings.
- A 2.5 m high headwall upstream (riverside) of the support piers which is submerged 1.0 m below water surface when the head pond is maintained at 518.00 masl.
- A walkway on the top of support piers with top elevation at 519.50 masl.
- 1% longitudinal bed slope in the settling basins.
- 1/3rd length of the settling basins upstream are provided with new guide walls having top

elevation at 518.20 *masl*. The existing guide walls with top elevation at 508.00 *masl* are retained for remaining 2/3rd length of the settling basins downstream. 6 m long transition is provided between the new guide wall and the existing one.

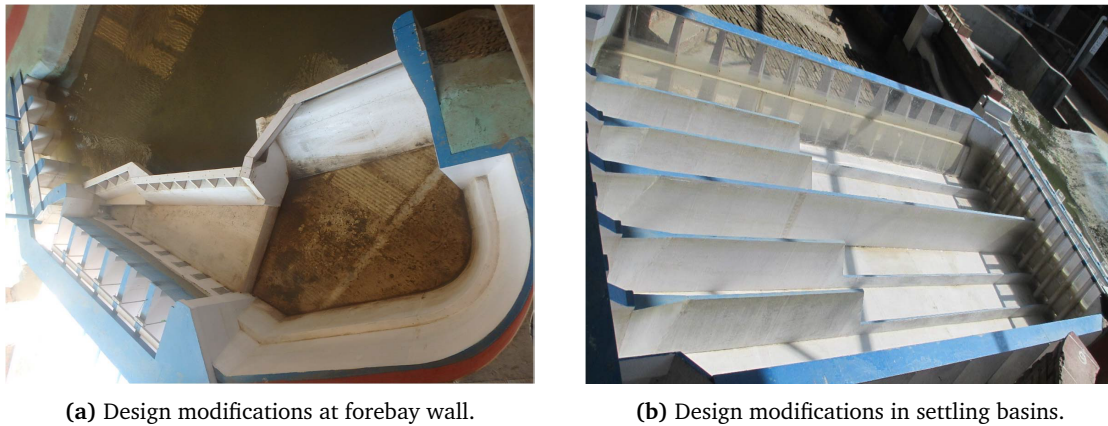


Figure 4.7: Physical hydraulic model with recommended design modifications (Hydro Lab, 2017).

4.6 Need for Numerical Modelling

Despite rigorous efforts made during the physical hydraulic model test, improvement in hydraulic performance has only been documented along with the qualitative assessment of the flushing efficiency. The performance of the modifications, aimed for better hydraulic performance are yet to be tested for their behaviour in terms of suspended sediment handling. Assessment of the trap efficiency can be made to evaluate the performance of the settling basins.

Trap efficiencies were estimated using several analytical approaches described in Section 2.6.4. The trap efficiencies found by using analytical methods are shown in Table 4.4.

Table 4.4 Trap efficiencies estimated using different analytical approaches for water temperature at 20 °C.

		Size fraction (Particle size [mm])			
		1 (0.5)	2 (0.355)	3 (0.125)	4 (0.09)
Trap efficiency η [%]	Hazen’s method ¹	84.49	80.49	52.06	37.67
	Velikanov’s method	98	98	90	72
	Camp’s method	100	100	98	60
	Vetter’s method	99.57	98.38	66.24	45.36
	Sumer’s method	Not applicable for $w/u_* > 1.6$			
	Garde et al. method	94.94	94.94	94.94	88.94
	Raju et al. method	100	100	100	99.52

¹ Trap efficiency is estimated with $m = 1$ since $m = 0$ is represented by Vetter’s method, See Items 1 and 4 in Section 2.6.4. See Tables C.2 to C.8 in Appendix C for detailed calculations.

The estimated values for trap efficiencies are better compared to the values determined from field measurements for existing settling basins (Figure 4.5), except for those determined from Hazen’s and Vetter’s methods for smaller size fractions. However, these analytical approaches are virtually exclusively based on basin geometry (Paschmann et al., 2017). These approaches would yield similar trap efficiencies for both the existing and modified structures since the basic dimensions are unaltered, and hence are not reliable to assess the change in sediment trapping in the settling basins.

The conventional approaches compute the trap efficiency well, provided the effective settling area has uniform flow distribution. However, the velocities in the operating situation are not always evenly distributed, and observations from fields and laboratory investigations show that settling basins with recirculation zones and secondary currents perform less efficiently than predicted, thus making these approaches unsuitable for such cases (Nøvik et al., 2014). Furthermore, these methods neglect or can not account for the approach flow conditions upstream the basin and the effect of inlet geometry, which can cause inhomogeneous basin flow, recirculation zones, and high turbulence responsible for reduced trap efficiency (Nøvik et al., 2014; Olsen and Skoglund, 1994; Paschmann et al., 2017).

Nevertheless, by utilizing numerical model, it is possible to account for the influence of the inflow and outflow conditions while estimating trap efficiency, which is derived from the comparison of incoming and outgoing sediment fluxes (Lysne et al., 2003, ch. 10). Besides, bed change computation in numerical modelling can be used for estimating change in trap efficiency over time with the increasing deposits. Moreover, with time-dependent computation, deposition pattern of sediments can be known, which can aid in designing flushing system (Olsen and Kjellesvig, 1999). The present study, therefore, intends to evaluate the performance of the settling basins with the recommended modifications in terms of suspended sediment handling by utilizing the numerical model.

Several works were done by different researchers successfully on problems related to headworks, including reservoir, intake and settling basins as described in Section 3.7.

Chapter 5

SSIIM

5.1 Introduction

SSIIM (Sediment Simulation In Intakes with Multiblock option) is a CFD program intended for use in River/Environmental/Hydraulic/ Sedimentation Engineering. Since 1990, the program has been under development by Prof. Nils Reidar Bøe Olsen at Norwegian University of Science and Technology. The program was originally developed for its use in simulating sediment transport in general river or channel geometries since a physical model study had difficulty in studying cases, particularly for fine sediments. However, the purpose of the program has later been expanded to cover other concerns in hydraulic engineering like spillway modelling, head loss in tunnels, stage-discharge relationships, turbidity currents, water quality simulations and habitat studies in rivers. Compared to general-purpose CFD software, SSIIM can model sediment transport with movable bed with complex geometries, which allows for modelling different sediment sizes, including sorting of bed load and suspended load, bed forms and influence of sloping beds.

Similar to other CFD models, SSIIM has three parts, namely a pre-processor, a solver and a post-processor. The pre-processor consists of tools like interactive graphical *Grid Editor* and *Discharge Editor* to generate grid and input data. While the solver consists of several modules to compute water velocity, water levels, bed levels, pressure fields, shear stress, etc. The program utilizes an implicit solver to compute the velocity field, which is further used while solving convection-diffusion equations for computing trap efficiency and sediment deposition pattern. As for post-processor, the user interface itself can display velocity vectors and other variables in two-dimensional view as plan, cross-section or longitudinal profile. Compared to other CFD programs, the graphics is directly associated with computational module, which allows users to view results while computation continues and identify the problems. Besides, the results can be exported in the form executable in programs like *Teleplot* or *ParaView* for post-processing.

There exist two versions of SSIIM: SSIIM 1 and SSIIM 2. SSIIM 1 uses a structured grid while SSIIM 2 uses an unstructured grid. SSIIM 1, as it uses structured grid, has an advantage of each cell being easily identified with the i, j and k indexes, which enables easy manipulation of outblocking, wall locations and inflow/outflow surfaces. While the unstructured grid of SSIIM 2 does not have such freedom as the grid cells have only one index making it difficult to detect manually. Graphical *Discharge Editor* should be used to specify the inflow/outflow areas. However, *Grid Editor* available in SSIIM 2 enables generation and connections of multiple blocks, which are appropriate for making grids for complex geometries. Multiple blocks are not possible in SSIIM 1 as the *Grid Editor* works on one block only. Also, SSIIM 2 has additional sediment transport and water quality algorithms, which are not implemented in SSIIM 1. Besides, SSIIM 2 is capable of modelling wetting/drying conditions and lateral movements of the stream, which allows complex grid to adapt to the varying boundaries. Nevertheless, due to the simple connections between cells,

surfaces and geometry points, the structured grid used in SSIIM 1 occupies less memory per cell. Also, the computational speed is better for structured grid version due to faster solvers.

The present study uses SSIIM 1 for simulations with limited application of SSIIM 2 for generating the *koordina* file (See Section 6.3), so most of the text mentions SSIIM 1 simply as SSIIM unless mentioned explicitly. Upcoming sections describe briefly on the files and data sets (Appendix D) pertinent to the thesis work. The readers are therefore encouraged to go through SSIIM User's Manual to comprehend SSIIM and its working principles in detail. The program and user's manual can be downloaded for free from <http://folk.ntnu.no/nilsol/ssiim//>.

5.2 Input/Output Files

There are a range of input and output files, which are read and written by SSIIM. The files relevant to the work are discussed below:

The *geodata* file

The *geodata* file comprises geometrical data represented by x , y and z coordinates obtained from the field measurements, digital maps or GIS. The file serves as the input for *Grid Editor* for grid generation and bed interpolation. SSIIM 2 has extra options to modify the *geodata* file and the modified file can be used in SSIIM 1 afterwards.

The *boogie* file

The *boogie* file lists the intermediate results from computation, including average water velocity, shear stress and water depth during the initialization. Trap efficiency and sediment grain size distribution are also written in the file. Besides, the file displays explanation in case errors occur during simulation. By including D on $F 1$ data set, additional information can be written in the file.

The *control* file

The *control* file feeds in most of the parameters required for the model simulation including grid size, water level, discharges, roughness coefficient, sediment properties, etc. These parameters are provided in the file using different data sets initialized with upper-case letters F , G , I , K , S , W , etc.

The *koordina* file

The *koordina* file defines the bed surface of the grid geometry, which can be made from a map, a spreadsheet or using the *Grid Editor*.

The *koomin* file

The *koomin* file is similar to *koordina* file with exact same format. The *koomin* file defines the minimum elevation surface for bed changes, i.e., the bed will not get underneath the surface defined.

The *unstruc* and *koordina.si1* files

The *unstruc* file stores data for geometry in SSIIM 2. The file consists of coordinates for all grid intersections and information about inflow/outflow discharges and water quality parameters. SSIIM 2 also creates a *koordina.si1* file simultaneously with *unstruc* file. The *koordina.si1* file can be executed in SSIIM 1 after retitling it as *koordina* without any extension, provided that grid contains a single block.

The *timei* and *timeo* files

The *timei* and *timeo* files are related to time series calculations addressing the variation in discharge, waterlevel, sediment concentration and control for output. The *timei* file serves as the input for time series of parameters while the *timeo* file is an output file containing time series from the model simulation.

The *porosity* file

The *porosity* file defines the magnitude and location of porosity in the geometry. $F 7$ data set with P should be used in the control file to evoke porosity computation. This file is used when the river

bed is covered by stones; however, in the present work, the porosity algorithm is utilized to resemble the effect of wire mesh used in the physical hydraulic model that serves as the trash rack in the prototype.

The result file

The *result* file is an output file that displays the results from water flow calculations containing water velocities in three directions, k , ε , pressure and fluxes on the cell walls. The result file is written when the solution gets converged or specified number of iterations are completed. The file also serves as the input for sediment flow calculations. Further, it is possible to start the flow computation from the stage represented in recently stored *result* file (*hot start*).

The interpol and interres files

The *interpol* file contains the x and y coordinates of locations where vertical profiles of velocity or concentration are required. The file is read when the control file contains the *F 48* data set with a number representing respective parameters. The program then interpolates the selected parameter in the verticals at locations defined in *interpol* file. The number 2 on the *F 48* data set causes interpolation of velocities, k and ε while number 3 causes interpolation of concentrations. The program writes the results to *interres* file without generating *result* file if this data set is used.

The Paraview.vtk file

The *ParaView.vtk* file is a graphic output file that serves as the input for the *ParaView* software for post-processing. The file is created from the user interface through the menu or the main program. The files written by the main program allows for incorporating user-specified variables as given on the *G 24* data set. It is also possible to write multiple files for one-time dependent simulation and thereby generate animation.

5.3 Theoretical Basis

5.3.1 Water Flow Computation

SSIIM solves RANS (Equation 3.18) in 3D geometry to compute the water velocity. The equations are discretized with a finite volume method. The convective terms are discretized with POW or SOU scheme as specified on *K 6* data set. Reynolds stresses are modelled using Boussinesq' approximation (Equation 3.19). SSIIM by default uses $k - \varepsilon$ model to compute the turbulent shear stress, however, other simpler model can be utilized, which can be specified on *F 24* data set.

The SIMPLE and SIMPLEC are used for pressure correction. The former is the default method while the latter can be invoked with *K 9* data set. SSIIM omits the transient term by default. Nevertheless, *F 33* data set with time-step and number of inner iterations can be used for transient computations. It is possible to supply water levels and discharges as time series in the *timei* file for transient simulations. The gravity term is neglected in the standard algorithms. However, for water surface calculations with higher gradients, gravity term can be included by using *F 36* data set.

The velocity gradient near walls is often steep, which requires large number of grids to be resolved. Instead wall laws are used assuming velocity profile obeys a certain empirical function. Navier-Stokes equations and turbulence equations both have certain discretized source terms. Wall laws are applied for the cells close to walls to deduce analytical expressions for the source terms. SSIIM uses Equation (3.44) as default wall law. The roughness, k_s in Equation (3.44) are specified on *F 16* data set. Besides, if the roughness varies at bed, roughness for each bed cell can be specified with the *bedrough* file.

5.3.2 Sediment Transport Computation

Sediment flow as stated earlier is conventionally categorized as bed load and suspended load. The suspended load is computed using transient convection-diffusion equation (Equation 3.46) for the

sediment concentration. The diffusion coefficient, Γ in Equation (3.46) is computed using the eddy-viscosity, ν_T in $k - \varepsilon$ model:

$$\Gamma = \frac{\nu_T}{Sc} \quad (5.1)$$

where, Sc is the *Schmidt* number which equals to 1.0 as default, however, the value may be altered with *F 12* data set. The source term, S in Equation (3.46), which gives the pick-up flux from the bed can be specified either as fixed concentration or as pick-up rate using *F 37* data set to account for the sediment resuspension. The default formula is van Rijn's formula (Equation 3.47) for suspended sediments. Several other formulae can be selected on *F 84* data set. Also, the empirical parameter in Equation (3.47) can be varied using *F 6* data set.

SSIIM computes the sediment transport by size fractions, which are specified on *S* data set along with their respective diameters and fall velocities. The number of sediment sizes are specified on *G 1* data set. Sediment inflow can be given either using *I* data set or *G 5* data set in SSIIM 1. The inflow is given in *kg/s* on the *I* data set for each size fraction and the concentration distribution is calculated with Hunter-Rouse equation. While in case of using *G 5* data set, the concentration is specified in volume fraction for a specific surface at the grid boundary. Both data sets may be employed at the same time to incorporate multiple sediment sources. The initial sediment fractions on the bed are defined with *N* and *B* data sets, which respectively gives number of sediment mixes and distribution of the mixes on the bed. It is also possible to use *timei* file to define sediment inflow for time series calculations.

The bed form height, Δ is computed using van Rijn's equation (Olsen, 2017, ch. 9):

$$\frac{\Delta}{D} = 0.11 \left(\frac{d_{50}}{D} \right)^{0.3} \left(1 - \exp \left[\frac{-(\tau - \tau_c)}{\tau_c} \right] \right) \left(25 - \left[\frac{\tau - \tau_c}{\tau_c} \right] \right) \quad (5.2)$$

where, D is the water depth, d_{50} is the average sediment particle diameter, τ represents the bed shear stress, τ_c is the critical shear stress to move the sediment particles. The effective hydraulic roughness, k_s is calculated by using the bed form height and sediment grain size distribution with the equation (Olsen, 2017, ch. 9):

$$k_s = 3d_{90} + 1.1\Delta \left(1 - \exp \left[\frac{-25\Delta}{\lambda} \right] \right) \quad (5.3)$$

where, λ is the bed form length equal to $7.3D$ and d_{90} refers to the particle diameter corresponding to 90% cumulative percentile.

5.4 Limitations

Like any other computer program SSIIM has some limitations which are listed below:

- The program ignores non-orthogonal diffusive terms. Grid cells with angles differing significantly from 90° might yield inaccurate diffusion.
- The grid lines in vertical direction should be perfectly vertical. This can avoid a fitting alignment of the grid cells with the flow field causing false diffusion.
- The kinematic viscosity of the fluid is hard-coded in the program and is equivalent to water at 20°C .
- The program is not made for marine environment, so effects due to density gradients as a result of salinity gradients are not considered.
- SSIIM program contains over 100,000 lines of source code and some less tested modules, which may not work as anticipated. Also, some combinations of modules may not have been tested at all. It is therefore likely that there are number of bugs and it should be well considered while evaluating the results from the program.

Chapter 6

Hydraulics Simulation

6.1 Simulation Case

The numerical model study here intends to evaluate the performance of the settling basins with changed hydraulics due to the modifications recommended from the physical hydraulic model investigation, along with the sediment concentration distribution and bed deposition pattern. The numerical model was run only for the modified headworks with recommendations listed in Section 4.5.

The simulation was run for a constant flow of $1,200\text{ m}^3/\text{s}$ while maintaining downstream water level at 518.00 masl . The discharge resembles the flow carrying a significant quantity of sediment and is exceeded on an average of two weeks per year (MWH, 2015, as cited in Hydro Lab, 2017). Furthermore, the same discharge was used for the comparison of flow behaviour between existing and modified headworks during the physical hydraulic model test, so that the velocity measurements were adequately available for calibrating the numerical model. The operation level of 518.00 masl represents the operation during flood periods when sediment problems are more pronounced. During dry periods, practically no severe problems are encountered while the plant is being operated in peaking runoff mode at operation level of 524.00 masl . Similarly, the simulation replicated the settings for gate operation adopted for the physical hydraulic model test, which are outlined in Table 6.1.

Table 6.1 Gate operating conditions for $1,200\text{ m}^3/\text{s}$ (Hydro Lab, 2017).

Spillway gates	
Gate 1 (left bank/ closer to forebay wall)	Closed
Gate 2 (middle)	3.7 m open
Gate 3 (right bank/ far from forebay wall)	3.8 m open
Intake gate	All six gates fully opened
Under sluice gates	All eight gates closed
Forebay flushing gate	Closed
Settling basins' flushing gates	All twelve gates closed

6.2 Simplifications

Various simplifications were adopted to create the model that is workable and yet representative to the prototype so that it eases working with the software. They are as follow:

1. Abrupt changes in geometries and complex geometries were simplified to avoid complications in grid generation. Round edges were ignored and replaced with sharp edges, as working with

- round edges can be time consuming.
2. Pool formation after the forebay by erection of walls over the existing forebay weir was ignored. A vertical wall was considered in numerical model to exclude the pool. As observed from the dispersion of dye in the physical hydraulic model, it does not have much effect on the flow into the basins (Figure 6.1).
 3. Side slopes in the settling basins were treated as vertical since the expansion ratio becomes too large as the cells become thinner and lengthier compared to adjacent cells, which may lead to unphysical results (Figure B.4).
 4. Tapering guide walls and divide wall in the settling basins were considered to have uniform thickness throughout their height. Thickness was taken as the average of the top and bottom thicknesses (Figure B.4).
 5. The gradual change in the height of guide walls was replaced with the vertical transition since it was not possible to make a sloping surface (Figure B.2).
 6. There exist 12 gates at the end of settling basins opening into the collector channel in the real case. However, two gates in each bay were combined into a single outlet for simplicity as the grid size and grid location were incompatible for precise representation of the separation between two adjacent gates.
 7. Different collector channel gate openings recommended from the physical hydraulic model test were not simulated in the numerical model. Instead, equal discharges were passed through the outlet of each bay so that the numerical model becomes less complex. The openings in the physical hydraulic model were maintained such that equal discharges pass through each gate as well as each basin (Biswhwakarma, 2018).
 8. The length of each bays is considered to be equal so that the plan of settling basin was modelled as being rectangular instead of trapezoidal.

The plan view of the geometry after simplifications, considered for numerical modelling is shown in Figure 6.2 and the actual geometry with design modifications recommended from the physical model test, including dimensions are shown in Figures B.1, B.2a, B.3a and B.4a.

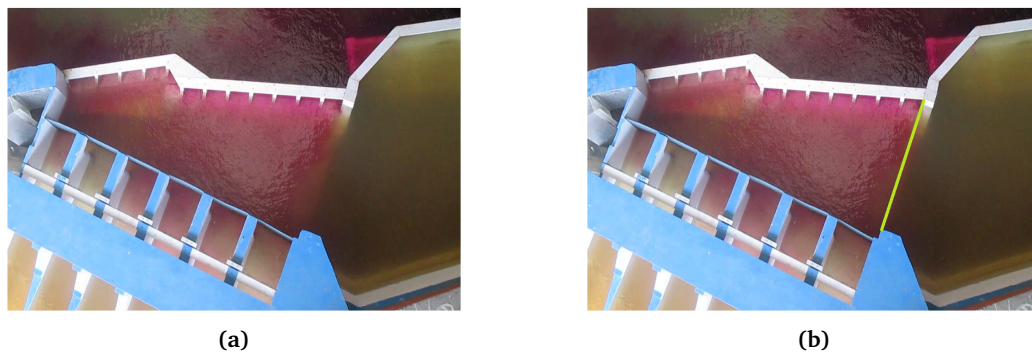


Figure 6.1: (a) Flow pattern in forebay for $1,200\text{ m}^3/\text{s}$ discharge in the river, with almost no dispersion of dye towards the pool (Hydro Lab, 2017), (b) Schematic representation of the vertical wall considered in numerical model to exclude the pool.

6.3 Grid Generation

The *koordina* file in SSIIM defines the basic geometry for the model. The limitation that the vertical grid lines are perfectly vertical simplifies the grid generation since the coordinates for grid points on a plan view are only required. The information of topography, including river bed and geometry of the structure as provided in the drawings, were used to extract the coordinates for the grid points with combined use of *AutoCAD* and *MS Excel* program. As a starting point, the model boundary was defined in the available drawings. The major modifications were proposed at the forebay wall. Hence,

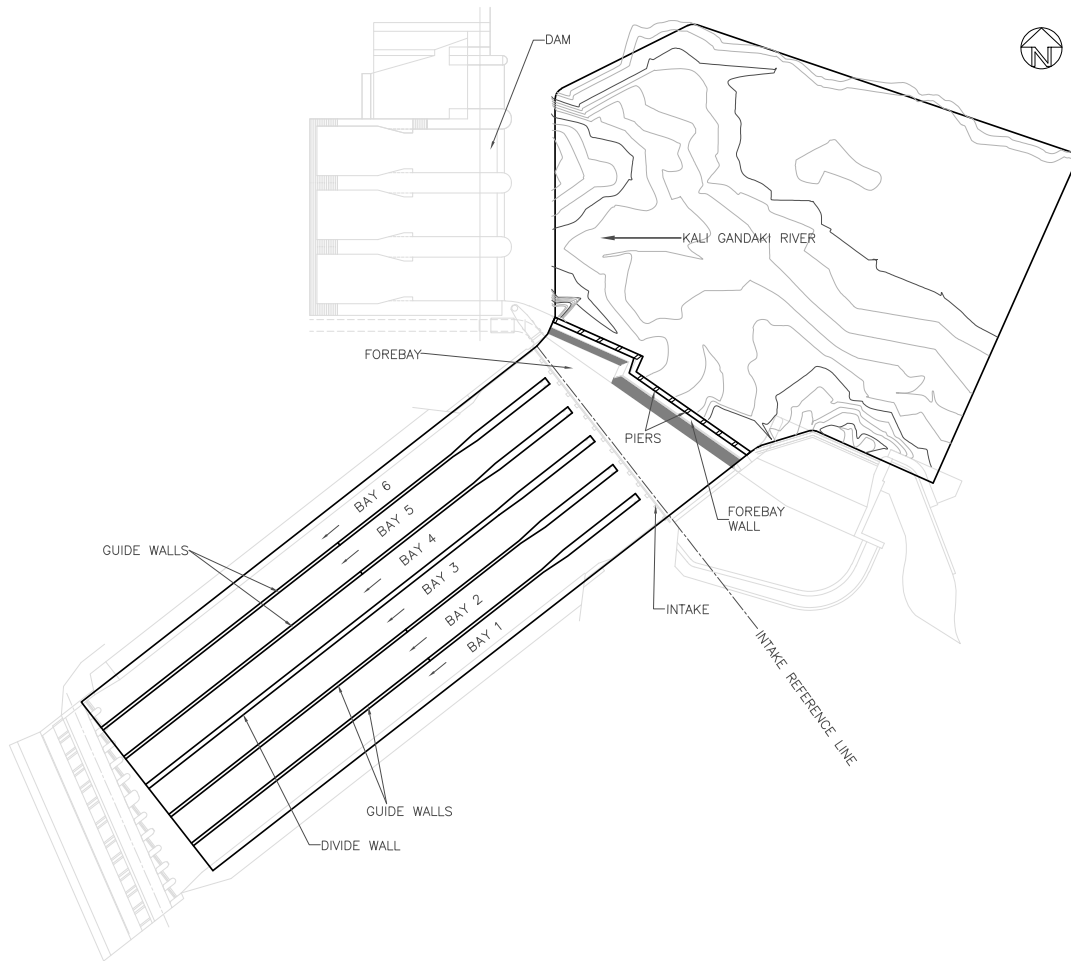


Figure 6.2: Plan view of simplified geometry (black) considered for numerical simulation laid over the actual geometry with recommended design modifications (light grey) including river portion.

a certain segment of the river was included, with the inflow boundary of the model at approximately 200 m upstream from the spillway, so that the influences due to the modifications at forebay wall can be investigated.

The grid generation was dealt with by splitting the geometry into two portions: the river portion with irregular geometry and the structural portion from the forebay wall to settling basins with well-defined linear geometry, for which separate approaches were used to find the coordinates. SSIIM 2 was used to make the *koordina* file for the river portion while for the rest, the input for the *koordina* file was created in MS Excel.

The *geodata* file, as required for delineating complex geometry in SSIIM 2 was created using the contour lines. The contour lines were first transformed into the points and the coordinates of each point were extracted. The *geodata* points are displayed in Figure 6.3 as they appear in *Grid Editor*, where the colors portray different elevations. SSIIM 2 uses the *geodata* file also to interpolate bed levels (z values) of the grid points using the nearest *geodata* points in the file. The grid points were adjusted by defining and dragging *NoMovePoint* to best represent the river boundary. Having got a reasonable grid in 2D, the grid generation was completed by generating 3D grid, which was saved as the *unstruc* file. Meanwhile, a file called *koordina.si1* is created, which can be used in SSIIM 1 by simply retitling as *koordina* without any extension.

As for the structural portion, the grid was first drawn in AutoCAD with due attention to the location and orientation of barriers like forebay wall, piers, intake control, guide walls and divide wall so that they can be later outblocked precisely. Guided by the grid drawing, the coordinates were calculated



Figure 6.3: Geodata points for the river portion.

in MS Excel. Some simplifications were introduced while defining the structures, which are listed in Section 6.2. The coordinates for the river and settling basins were then merged into a single *koordinata* file with minor adjustments to ensure a smooth connection between the lines.

The grid is a single block, structured and non-orthogonal composed of hexahedral cells. The grid has $185 \times 38 \times 12$ cells in the streamwise, lateral and vertical direction, respectively, with a total of 84,360 cells for coarse grid resolution. The vertical grids distribution was set up in a way that they comply with the elevations of spillway gate openings, surfaces of forebay wall and guide walls in the basin, and openings at the basin outlet. The plan view of the grid used for the simulation in model scale (1:40) with coarse grid resolution is shown in Figure 6.4.

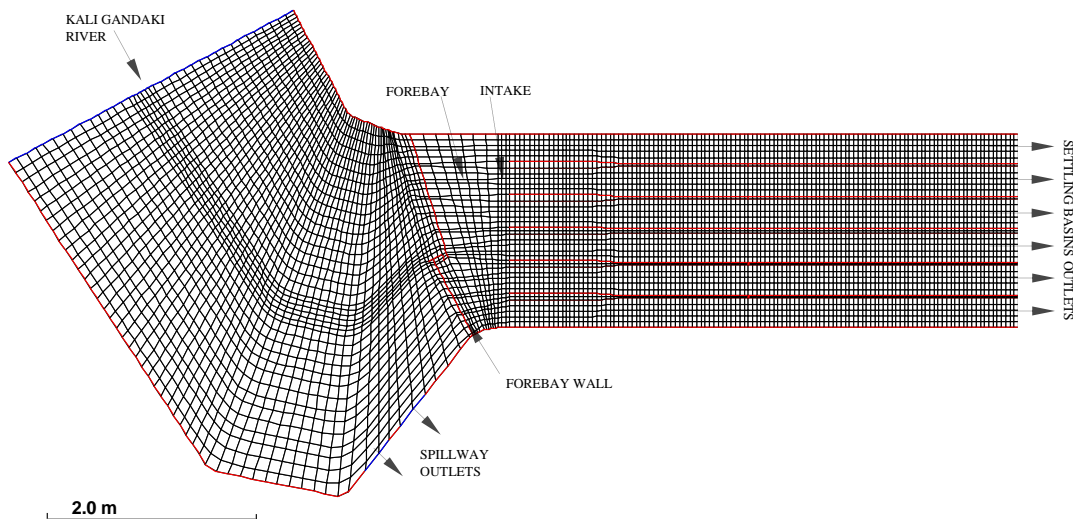


Figure 6.4: Plan view of grid used in simulation (model scale, coarse grid resolution). The orientation was changed to comply with the requirement in SSIIM such that the inlet is on the left side and the outlet is on the right side.

6.3.1 Defining Components, Inlet and Outlet in SSIIM Model

Outblocks defined by *G 13* data sets (24 *G 13* data sets in total) were used to represent forebay wall, piers over the forebay wall, guide walls and divide wall. Wall laws were applied on sides and top for forebay wall and guide walls with the surface at 508.00 *masl*, whereas for piers, divide wall

and guide walls with the surface at 518.20 *masl*, wall laws were restricted to sides only as no water passes over them. Plan views of the model at different levels are shown in Figure B.5 that depict the aforementioned structures.

The inlet and outlets in SSIIM model were defined by *G 7* data sets in the *control* file. The grid consisted of one inflow area and eight outflow areas, of which two outflow areas represented spillway outlets and six outflow areas described outlets at the end of each of the six bays. Refer the *control* files given in Appendixes D.1 to D.4.

6.4 Model Scale Simulation and Calibration

The aim of the hydraulic simulation in model scale (1:40) was basically to replicate the measured velocities in the physical hydraulic model. Numerous simulations with different parameters were run to get the best possible correspondence between measured and simulated results. The numerical model after calibration was intended to be scaled up, to evaluate the performance of the settling basins in terms of sediment trap efficiency along with other associated behaviour in prototype scale.

Hydraulic simulation involved a steady state computation with fixed water surface across the cross-section and fixed bed. The simulations were also tested for two different grid resolutions and two discretization schemes. The coarse grid consisted of $185 \times 38 \times 12$ cells while the fine grid consisted of $370 \times 76 \times 12$ cells, obtained by doubling the number of cells in plan of coarse grid by using *F 7 DJ* data set. The discretization schemes included POW scheme and SOU scheme, which were defined in *K 6* data set.

6.4.1 Input Data

For model scale simulation, the scaled down constant discharge of $0.1186 \text{ m}^3/\text{s}$ was used at the upstream end of the river, of which a total of $0.01392 \text{ m}^3/\text{s}$ was passed through the settling basins ($0.00232 \text{ m}^3/\text{s}$ in each of the six bays) and the rest $0.10468 \text{ m}^3/\text{s}$ through the spillway ($0.05234 \text{ m}^3/\text{s}$ in each of the two gates). The inflows and outflows were defined using *G 7* data set. A constant downstream water level was maintained at 12.95 *masl*, which was defined on *W 1* data set. The discharges and water level were derived by using the scale ratios given in Table 4.2; for example, the discharge of $1,200 \text{ m}^3/\text{s}$ in prototype was scaled down as $1,200/40^{2.5} = 0.1186 \text{ m}^3/\text{s}$, and the elevation of 518.00 *masl* in prototype was scaled down as $518.00/40 = 12.95 \text{ masl}$, and so on.

A roughness height, k_s of 2 *mm* was used, which corresponds to Manning's roughness coefficient, n of $0.011 \text{ s}/\text{m}^{1/3}$ for cement lined channel and planed wood (Chow, 1959, ch. 5). The value of k_s was determined using Equation (6.1) (Olsen, 2018). The roughness was defined with *F 16* data set.

$$k_s = 3d_{90} \quad \text{and} \quad n = \frac{d_{90}^{1/6}}{26} \quad (6.1)$$

where, $d_{90} = 0.67 \text{ mm}$ (obtained from Equation 6.1) refers to the particle diameter corresponding to 90% cumulative percentile.

6.4.2 Input Files

The *control* file (Appendix D.1), the *koordina* file (Appendix D.5), the *interpol* file (Appendix D.7) and the *porosity* file (Appendix D.9) were used in the hydraulic simulation. The *control* file included major parameters for simulation namely, simulation option, roughness height, grid size and distribution, inflow and outflow discharges, downstream water level, etc. Outblocks and associated wall laws options, number of iterations, relaxation factors and discretization scheme were also defined in the same file. The major data sets relevant to the current work are described in Appendix D.1

The coordinates describing the bed surface of the model geometry were defined in the *koordina* file.

The procedure for extracting the coordinates are illustrated in Section 6.3. The x and y coordinates of the measurement points used in the physical hydraulic model were added to the *interpol* file so that the velocity profiles were extracted at identical positions for comparison. The *porosity* file is described in detail in Section 6.4.3.

6.4.3 Use of the *Porosity* File

A wire mesh was used in the physical hydraulic model to represent the trash rack in the prototype. The results from simulations without considering wire mesh deviated largely at all the bays with an exception in Bay 3. And it became apparent that wire mesh was influencing the flow, so it had to be considered in the simulations.

Initial attempts involved the addition of artificial vertical outblocks (up to 48 outblocks were used) in alternate cells to mimic the area reduction by the mesh. However, the simulation produced unsatisfactory results that deviated largely from the measurements. Also, the simulation with different grid resolutions showed a drastic difference in the flow field since the outblocks could not be defined the same way for each grid resolution due to grid size constraint and limitation of the number of outblocks that can be utilized in SSIIM (maximum allowance of 49 outblocks).

The simulation of trash rack requires high resolution with extremely small cell sizes; less number of cells cannot resolve properly the geometry and large number of cells demands substantial simulation time (Qiu et al., 2014). Investigations, for example, Lućin et al. (2020) or Qiu et al. (2014) have utilized unstructured grid with local refinement around the trash rack. However, unstructured grids and nested grids are not supported by SSIIM 1 (Olsen, 2018). Furthermore, the inclination of the trash rack and shape of bars can make the simulation more complicated.

Owing to these constraints and overall size of the geometry, resolving hydraulic features associated with wire mesh or trash rack was unfeasible within the current investigation. In order to account for the influence of wire mesh, a simplified approach involving porosity was adopted. The method involved simulation of the effects due to mesh on the flow with less computational expense instead of focusing on the real mesh dimensions.

The porosity algorithm was evoked by using P on the $F 7$ data set that introduces a sink term in velocity computation. The *porosity* file included the magnitude and location of porosity in the geometry (four values of the porosity at four vertical levels having the same zero reference as for the coordinates in the *koordina* file and the values are linearly interpolated for each cell by the program).

6.4.4 Calibration Data

Velocity measurements taken at different locations (Figure B.1) in the physical hydraulic model test were used for calibrating the numerical model. The observed data included velocities measured at six different sections within settling basins with 24 point measurements at each section (4 point measurements in the vertical direction at the mid-width of each bay, measured with ADV) and six single point measurement at intake (measured at point 2 m below the water surface with Micro-propeller current meter). The sections within the settling basins are named as *SB3*, *SB5*, *SB7*, *SB9*, *SB12* and *SB15*; where, *SB3* represents the first section after the inlet transition and *SB15* represents the last section closer to the basin outlet.

$F 48 2$ data set was used to extract the values of the velocities at corresponding locations defined in the *interpol* file so that the results are written in the *interres* file. MS Excel with custom-made macro was used to read the results in the *interres* file and interpolate the velocities at measured elevations for comparison.

6.4.5 Progress and Results

Having run the simulation well, different trials were made by varying roughness height, porosity and porosity levels to attain the results closer to the measured. Simulation with different roughness influenced only the gradients not the basic velocity profiles. On the contrary, the porosity and porosity levels had a major influence over the profiles, and hence were adopted for the calibration, with a constant roughness height of 2 mm. Several possibilities were evaluated to attain a more correct flow field, based on the results of previous simulations, which guided the values to be used in the next simulation. Initial simulations produced good correspondence with the measured values for the velocities closer to the surface but, the velocities closer to the bed deviated largely, including some negative velocities in the upstream sections, which contradicted the measured values. After numerous hit and trials, the porosity of 0.55 and the porosity levels given in Appendix D.9 produced relatively better results; the negative velocities closer to bed were reduced significantly with a compromise in velocities near the surface.

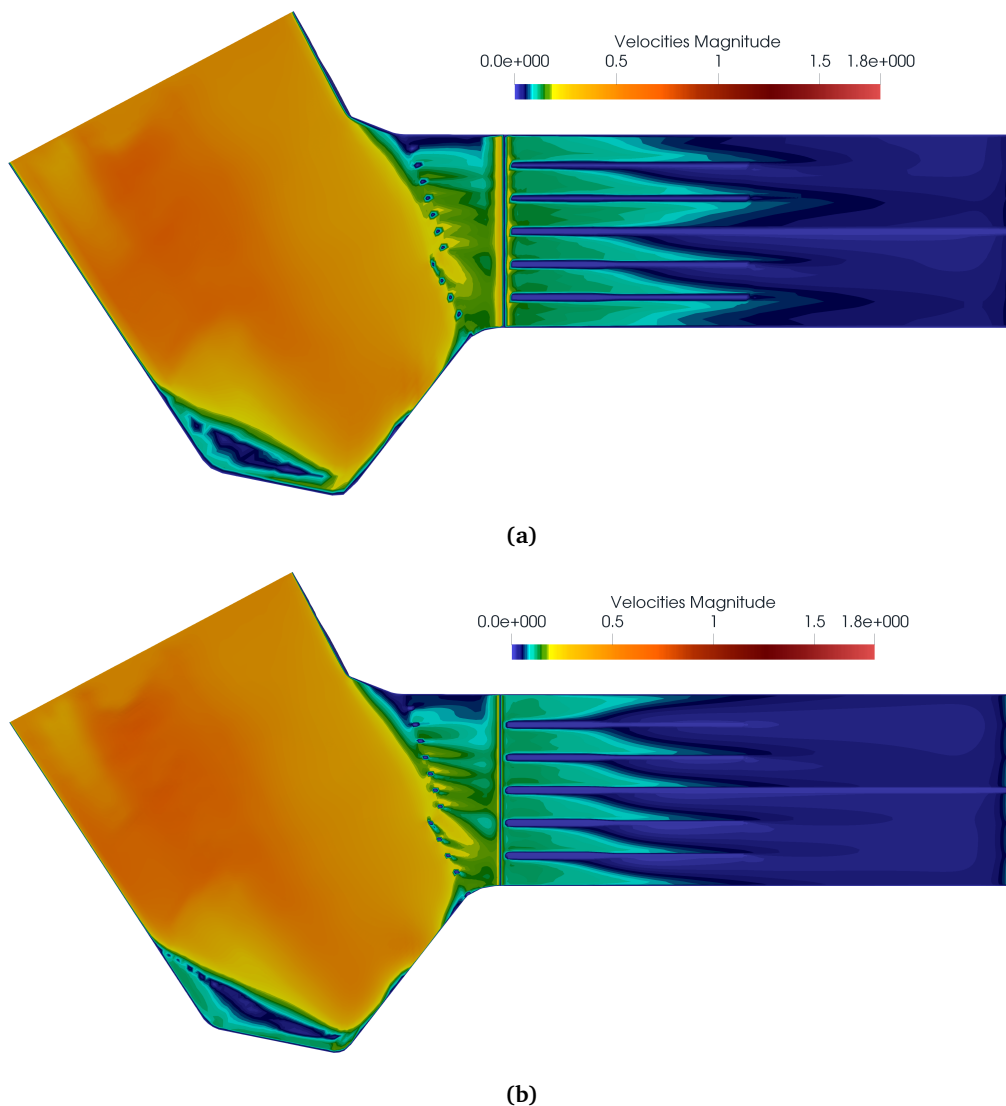


Figure 6.5: Simulated flow field (top view) with POW scheme; (a) coarse grid resolution and (b) fine grid resolution, (model scale). The uppermost and lowermost bays represent Bays 1 and 6, respectively.

Figure 6.5 shows the top view of simulated flow field for two grid resolutions and POW scheme. The flow velocities are redistributed and reduced from forebay to settling basin. The velocities reduce further along the settling and the flow field in fine grid resolution is more homogeneous compared

to that in coarse grid resolution. Besides, the flows in each bay deviate towards the wall and the direction (in Bays 1, 3 and 6) differs with the change in grid resolution.

Figure 6.6 shows the longitudinal profiles at Bay 1 with velocity vectors for two grid resolutions and POW scheme. Recirculation zones are observed at the end of the inlet transition closer to the bed, which were not identified in the physical hydraulic model test. For coarse grid resolution, the recirculation zone extends to a longer distance compared to that for fine grid resolution. Similar behaviour is spotted for other bays as well (Figure E.1).

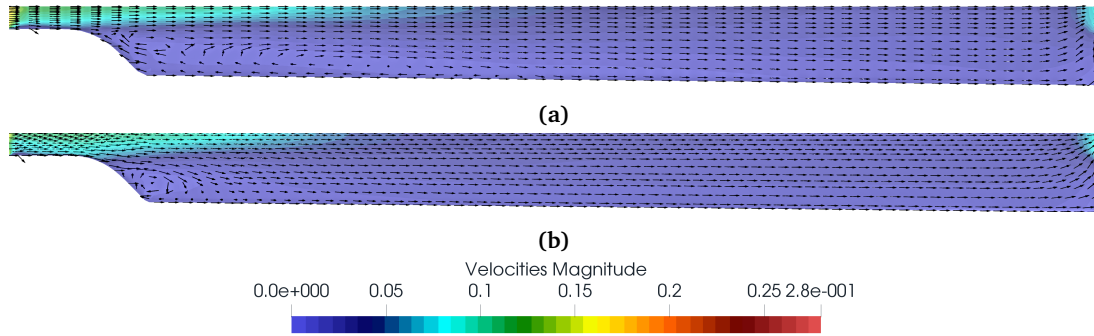


Figure 6.6: Longitudinal profiles with velocity vectors along Bay 1 for simulation with POW scheme; (a) coarse grid resolution and (b) fine grid resolution, (model scale). The velocity vectors represent only the direction of velocities not the magnitude.

Figure 6.7 shows the comparison of the measured and computed velocities at intake for two grid resolutions. The simulation using fine grid resolution appears to produce velocities closer to the measured in comparison to coarse grid resolution, except for Bay 5.

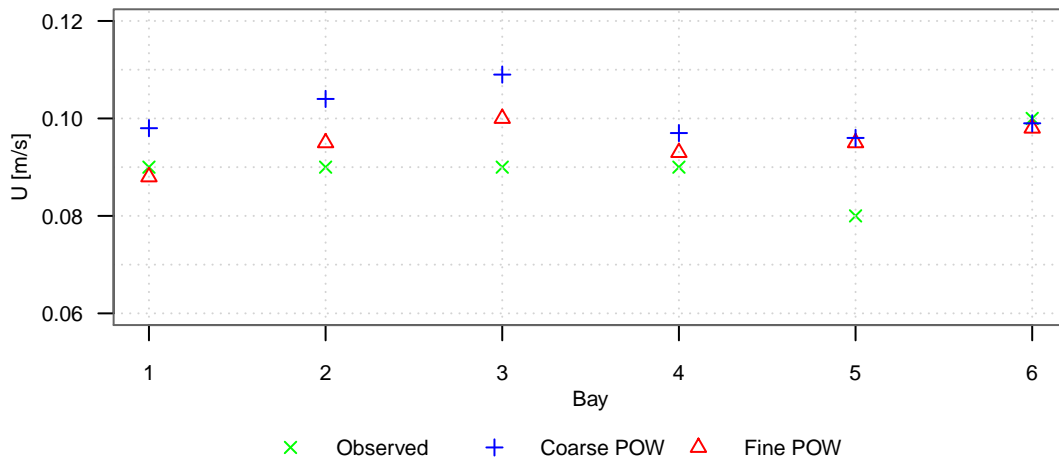


Figure 6.7: Measured and computed velocities at intake in different bays for simulation with POW scheme and different grid resolutions, (model scale).

Figures 6.8 and 6.9 show, respectively, the vertical and longitudinal profiles of measured and computed velocities in streamwise direction in settling basins, with the best results achieved. As seen on the plots, simulation with fine grid resolution shows better correspondence with the measurements compared to that with coarse grid resolution. The vertical profiles compare well with the measurements at later sections after SB7 (with relatively higher deviation in Bay 1), whereas larger deviations are seen in the sections before. These discrepancies are more pronounced in Bays 1 and 6, in comparison to other bays. Similarly, the velocities near the surface fit well (except for Bay 1) compared to those near the bed; however, the trend appears to be similar with few inconsistencies at upstream sections. Besides, in most cases the velocities are underestimated.

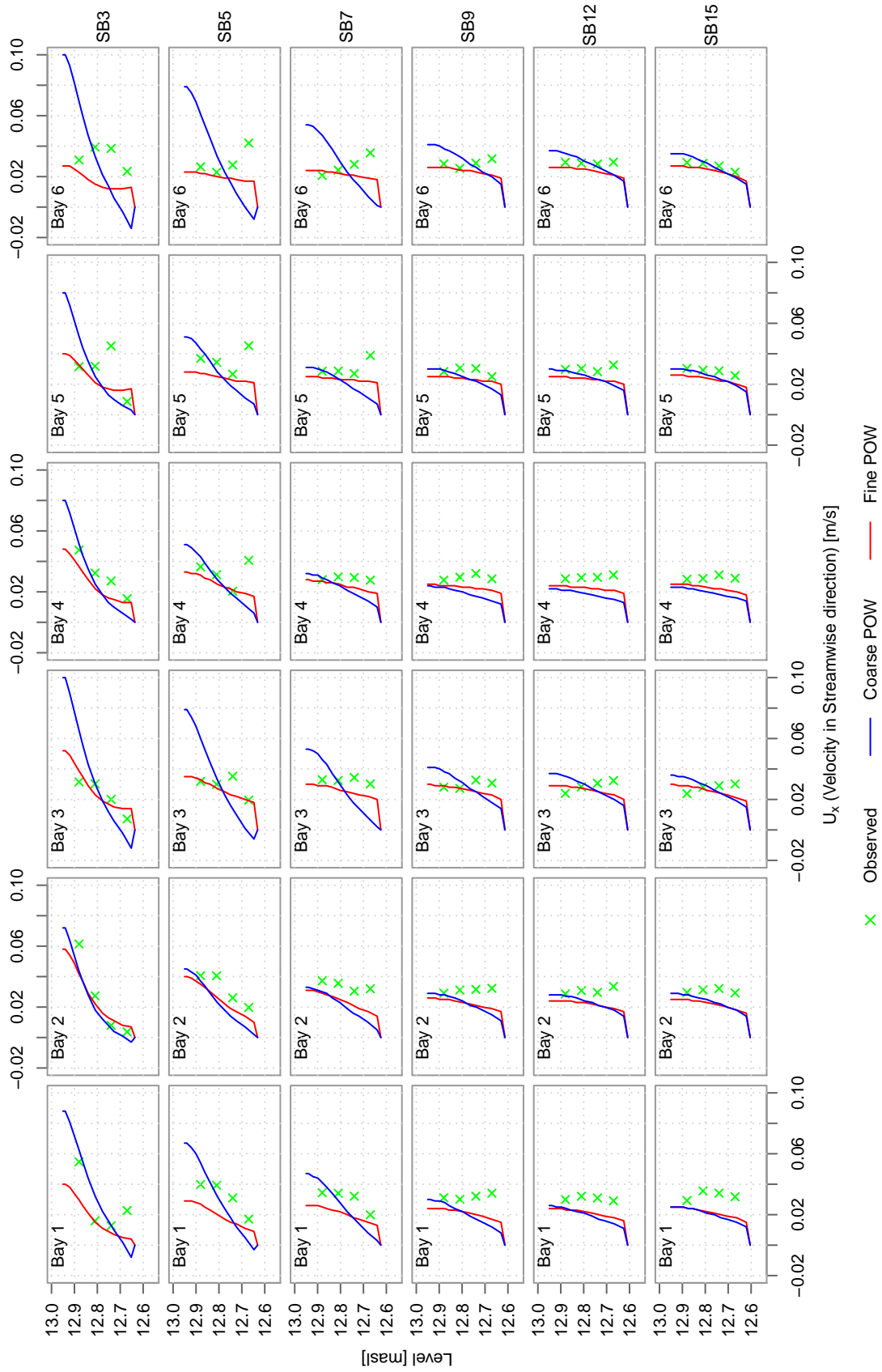


Figure 6.8: Vertical profiles of measured and computed velocities in streamwise direction, U_x in settling basins for simulation with POW scheme and different grid resolutions, (model scale).

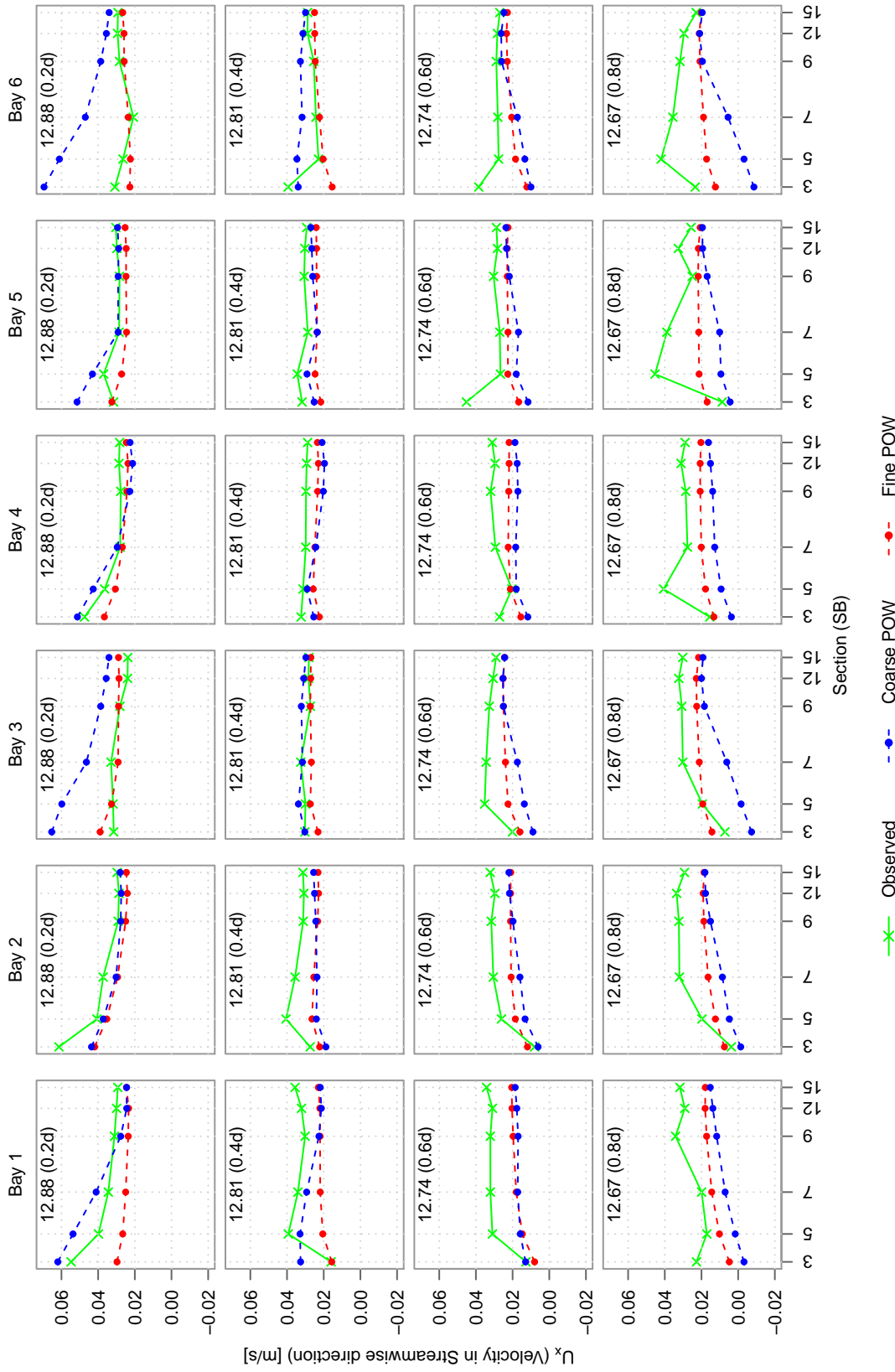


Figure 6.9: Longitudinal profiles of measured and computed velocities in streamwise direction, U_x in settling basins at different levels for simulation with POW scheme and different grid resolutions, (model scale). The levels indicated in the graphs are in $masl$ and d refers to the flow depth.

The simulation with SOU scheme did not show significant improvements in the results. Therefore, the fine grid resolution with porosity 0.55 and POW scheme was opted for sediment analysis in prototype scale.

6.5 Prototype Scale Simulation

After the model was calibrated to a reasonable accuracy by comparison with the measured velocities, the geometry of the numerical model was scaled up to represent the prototype (1:1). Hydraulic simulation involved a steady state computation with fixed water surface across the cross-section and fixed bed. The fine grid resolution, porosity of 0.55 and POW scheme, which produced the best conformity with the measurements in model scale simulation were considered for the simulation in prototype scale. The results of hydraulic simulation, including velocity field, pressure, bed shear stress are required for quasi-steady state simulation of sediment transport. The major advantage of simulating the prototype is that the outputs could be directly applied to the prototype without upscaling, thereby excluding scaling effects compared to the results of a physical hydraulic model (Haun and Olsen, 2012).

6.5.1 Input Data

For prototype scale simulation, the constant discharge of $1,200 \text{ m}^3/\text{s}$ was used at the upstream end of the river, of which a total of $141 \text{ m}^3/\text{s}$ was passed through the settling basins ($23.50 \text{ m}^3/\text{s}$ in each of the six bays) and the rest $1,059 \text{ m}^3/\text{s}$ through the spillway ($529.50 \text{ m}^3/\text{s}$ in each of the two gates). A constant downstream water level was maintained at 518.00 masl .

A roughness height, k_s of 3 mm was used, assuming a rougher surface in the prototype compared to that in the physical model. This is the highest value for a well finished concrete (Chanson, 2004, ch. 4) and corresponds to Manning's roughness coefficient, n of $0.012 \text{ s/m}^{1/3}$ and d_{90} of 1 mm .

The porosity of 0.55 was used as decided from the calibration of the model scale simulation, including the corresponding levels scaled up to represent the prototype size. However, the upscaled levels were modified due to the convergence problem. The simulation results were confirmed again by comparing the results with the upscaled measured velocities. Appendix D.10 shows a portion of the *porosity* file used for the prototype simulation.

6.5.2 Input Files

The *control* file (Appendix D.2), the *koordina* file (Appendix D.6), the *interpol* file (Appendix D.8) and the *porosity* file (Appendix D.10) similar to that used for model scale simulation were utilized for the hydraulic simulation in prototype scale. However, the discharges, roughness height, downstream water level and porosity levels were updated as described in Section 6.5.1. Also, the *koordina* file and the *interpol* file contained upscaled coordinates to represent prototype geometry.

6.5.3 Results

Figure 6.10 shows the top view of the flow field from the simulation, which is consistent with the flow field obtained in model scale simulation with fine grid resolution (Figure 6.5b) with an abnormality in Bay 3, where the flow deviates in the opposite direction. Nevertheless, the vertical and longitudinal profiles of velocities in streamwise direction (Figures 6.15 and 6.16) are similar to that for the model scale simulation with fine grid resolution (Figures 6.8 and 6.9). Figures 6.11 and 6.12 show the velocity distribution in different cross-sections, including intake and sections SB3 to SB15.

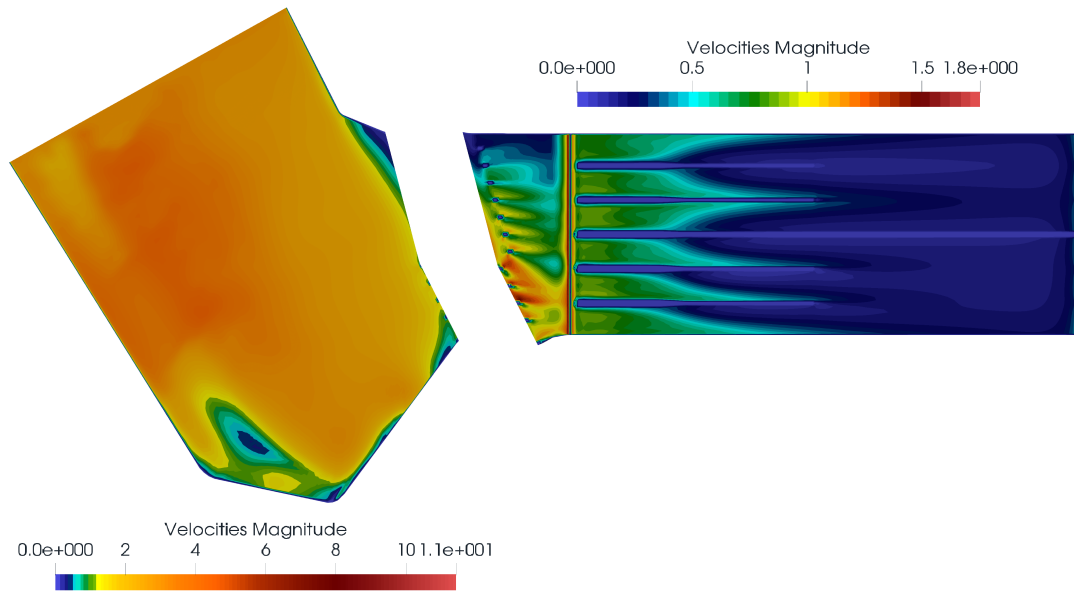


Figure 6.10: Simulated flow field (top view) with POW scheme and fine grid resolution, (prototype scale). The uppermost and lowermost bays represent Bays 1 and 6, respectively.

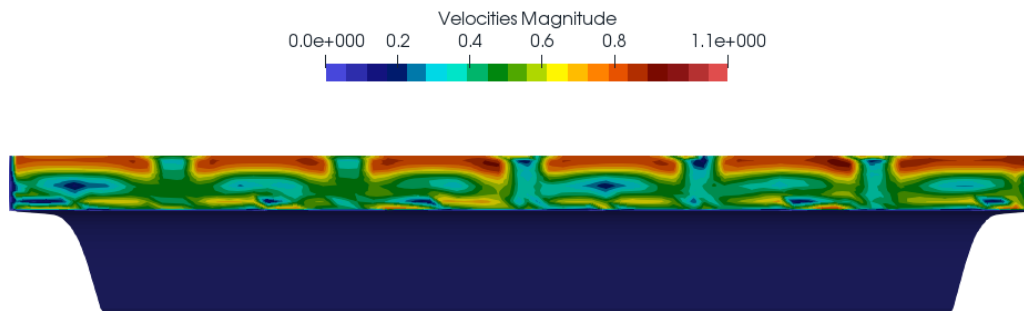


Figure 6.11: Velocity distribution at intake across cross-section (downstream view, prototype scale).

The flow field is considerably inhomogeneous in the river with maximum velocity of about 11 m/s around the spillway outlet (Figure E.2) and the average velocity is around 5.5 m/s . The velocity gets reduced in the forebay where a maximum magnitude of about 1.8 m/s can be observed. Roughly, the first one-third of the settling basins, particularly the inlet transition are characterized by inhomogeneous flow. However, lower velocities prevail on the remaining length, which becomes increasingly more homogeneous; the flow distribution in the right basin is relatively more uniform compared to that in the left (Figure 6.12). Besides, the magnitude of velocity drops to around the maximum of 1.1 m/s at the intake and continues to decrease significantly along the length from 0.6 m/s (closer to surface at SB3) to as low as 0.1 m/s (closer to bed at SB15) and even lower. The exit velocity is around 0.5 m/s . Higher velocities are dominant near the surface and upper segment of the walls, while the velocities near bed and lower segment of the walls are lower. The flow pattern at the intake appears to be symmetric and less affected by the flow in the forebay, which can be due to the control at the intake and the influence of trash rack represented by porosity in the current simulation.

Figure 6.13 shows the longitudinal profiles at each bay with velocity vectors. Recirculation zones are observed at the end of the inlet transition closer to the bed in all the bays, however, with slightly different lengths.

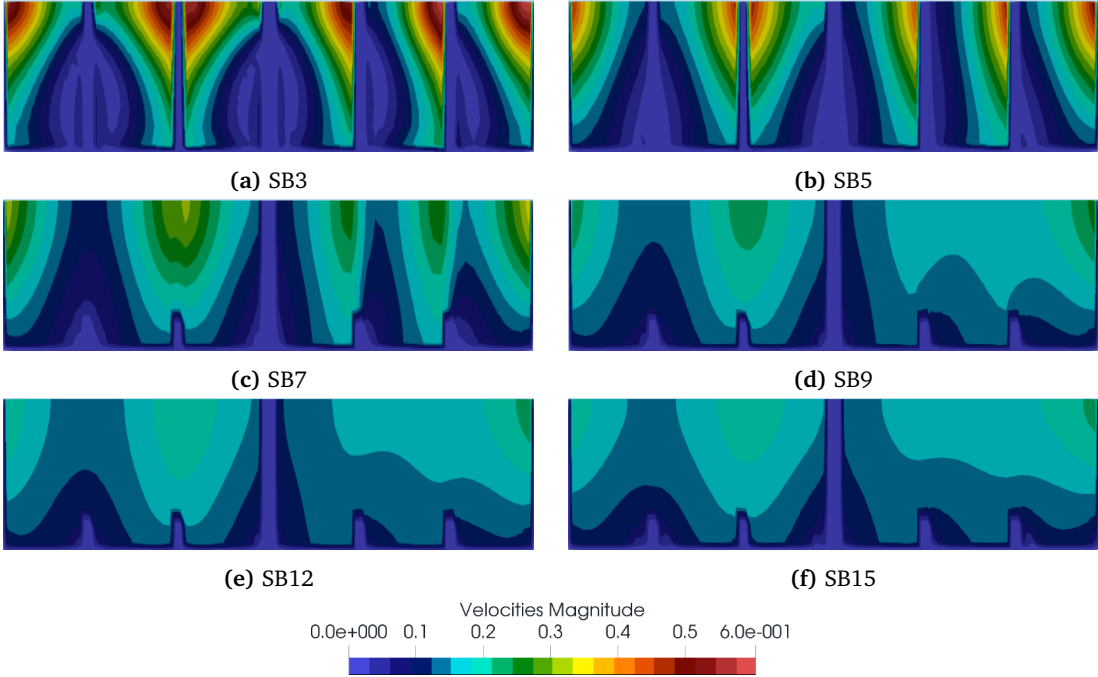


Figure 6.12: Velocity distribution in different cross-sections (downstream view, prototype scale).

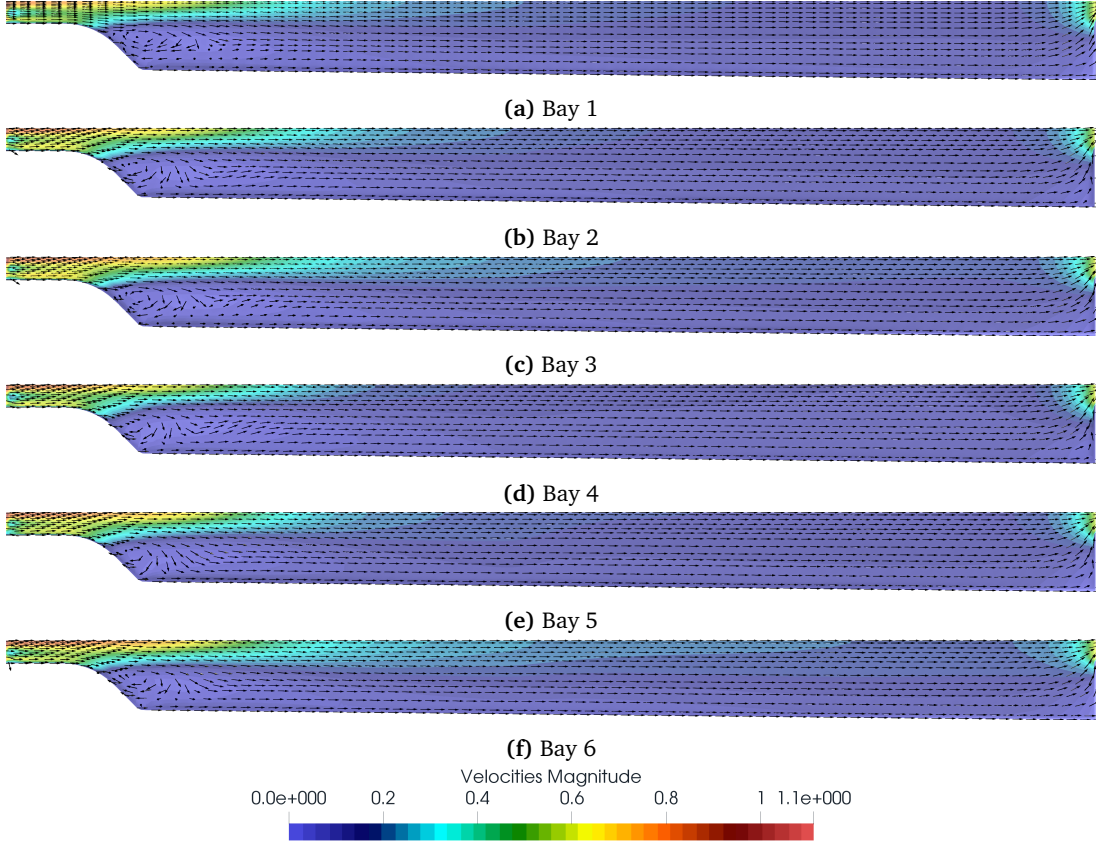


Figure 6.13: Longitudinal profiles with velocity vectors along each bay for simulation with POW scheme and fine grid resolution, (prototype scale). The velocity vectors represent only the direction of velocities not the magnitude.

Figure 6.14 shows the bed shear stress in the river, forebay and settling basins. The bed shear stress is higher at river with a maximum of 260 N/m^2 around the spillway outlet. The bed shear stress decreases to a maximum of 20 N/m^2 at the forebay and around 10 N/m^2 at the intake. The bed shear stress in the settling basins is substantially lower after the inlet transition, although a magnitude of around 2 N/m^2 can be observed at the inlet transition.

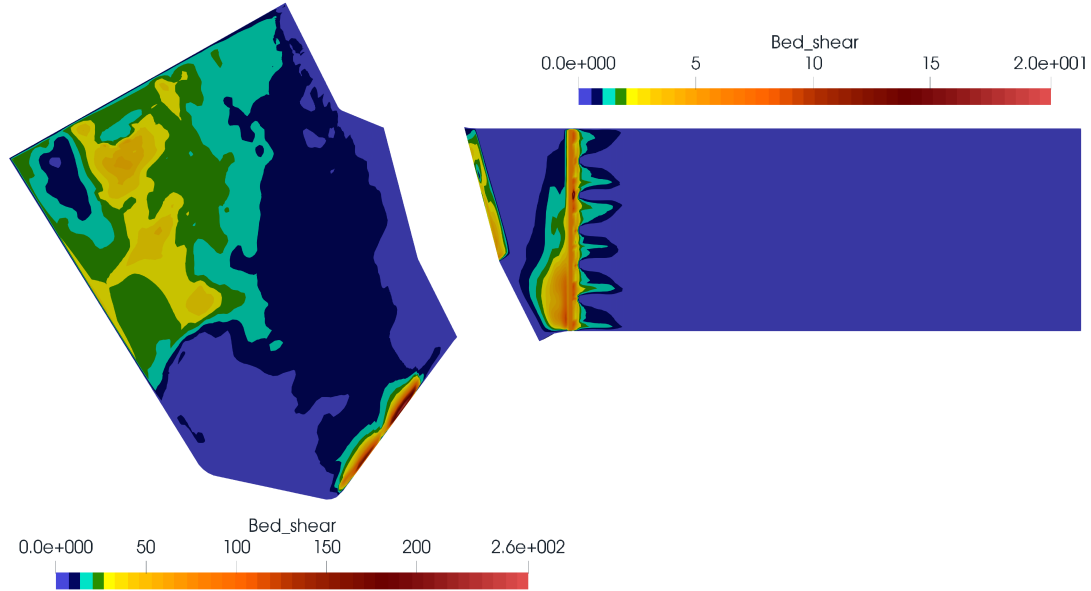


Figure 6.14: Simulated bed shear stress distribution with POW scheme and fine grid resolution, (prototype scale).

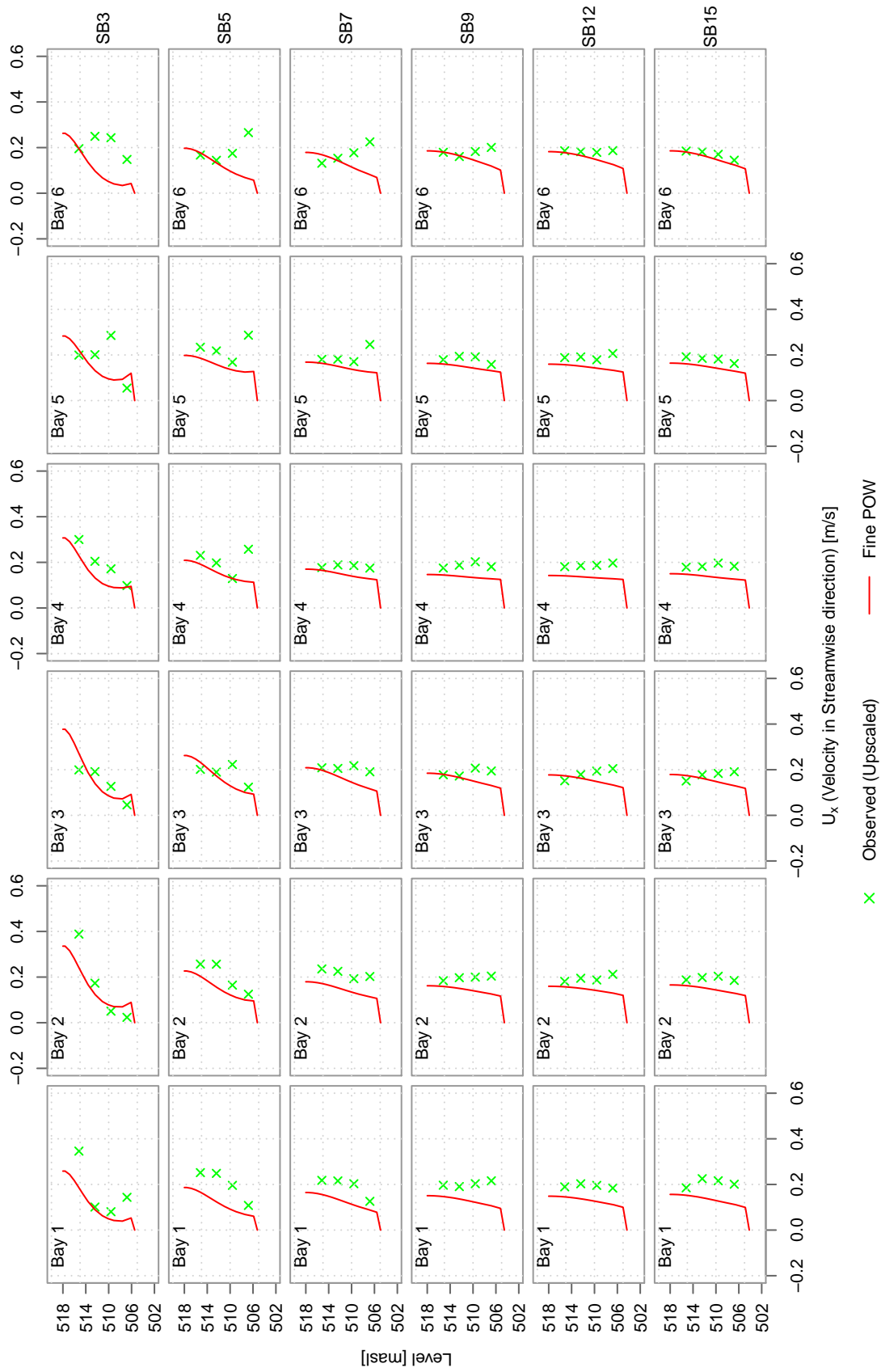


Figure 6.15: Vertical profiles of measured (upscaled) and computed velocities in streamwise direction, U_x in settling basins for simulation with POW scheme and fine grid resolution, (prototype scale).

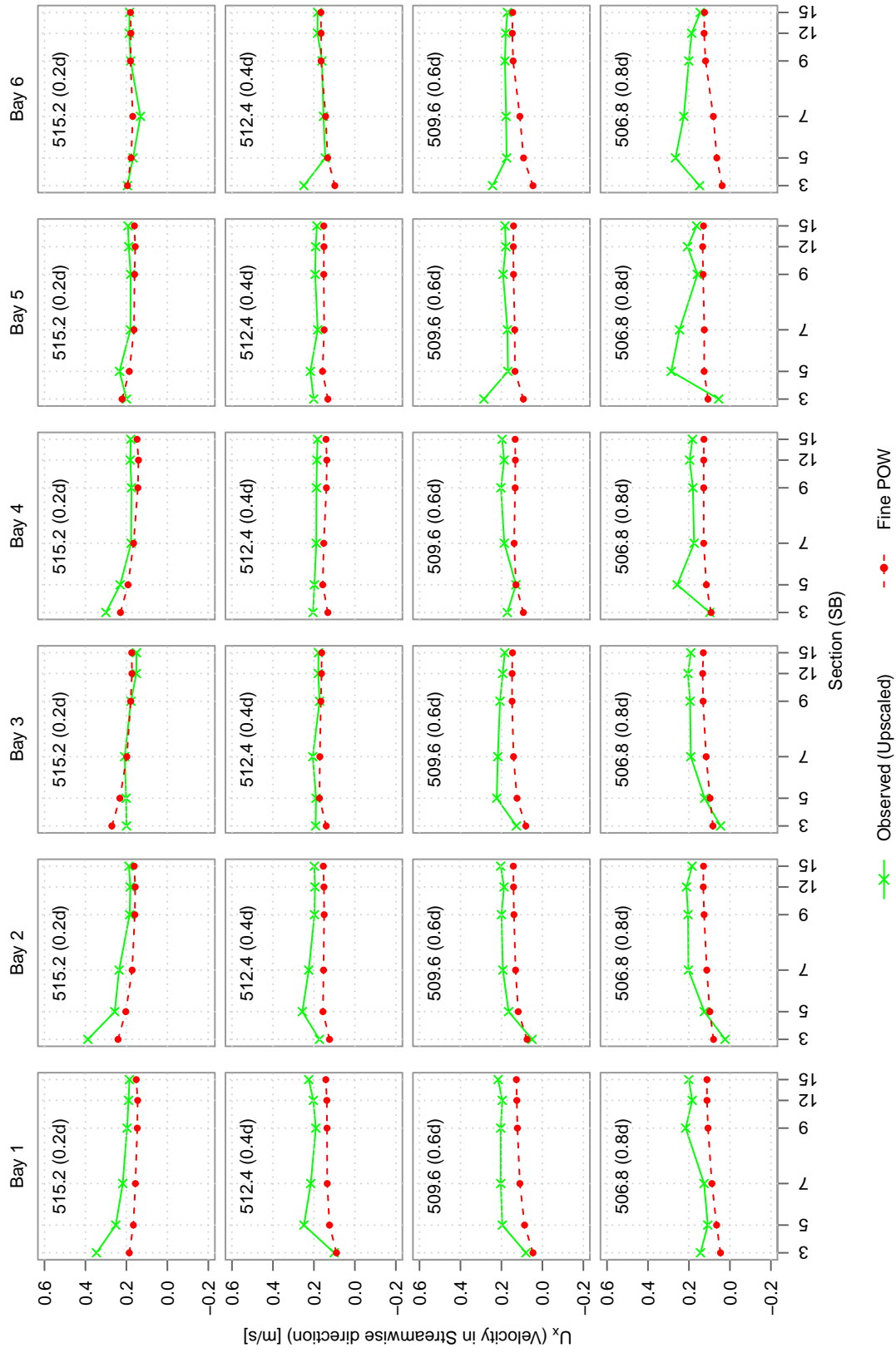


Figure 6.16: Longitudinal profiles of measured (upscaled) and computed velocities in streamwise direction, U_x in settling basins at different levels for simulation with POW scheme and fine grid resolution, (prototype scale). The levels indicated in the graphs are in $masl$ and d refers to the flow depth.

6.6 Problem Encountered

Initial attempts for hydraulic simulation encountered problems of poor convergence and required extended simulation time and number of iterations. This can probably be due to the use of numerous outblocks (24 in total) to represent the forebay walls, piers, guide wall and divide walls. Nevertheless, the convergence speed improved by the use of the *F 15 1* data set for similar set-up. The data set is used for the choice of algorithm for wall laws and the integer *1* directs the program to use only the closest wall (usually the bed), if there are two walls in a cell.

The results varied with the change in orientation of the model. First simulations were carried with the model orientation shown in Figure 6.17, which was obtained by rotating the site orientation (Figure 6.2) by 180° such that the North pointed downwards. This was done to comply with the requirement of the software, so that the inlet is on the left side and outlet is on the right side. Out of curiosity, the orientation was changed with the outlet and side walls of settling basins along the y-axis and x-axis, respectively (Figure 6.4). Changing the orientation improved the results, and hence the model with latter orientation, i.e., Figure 6.4 was opted for further simulation to calibrate the model.

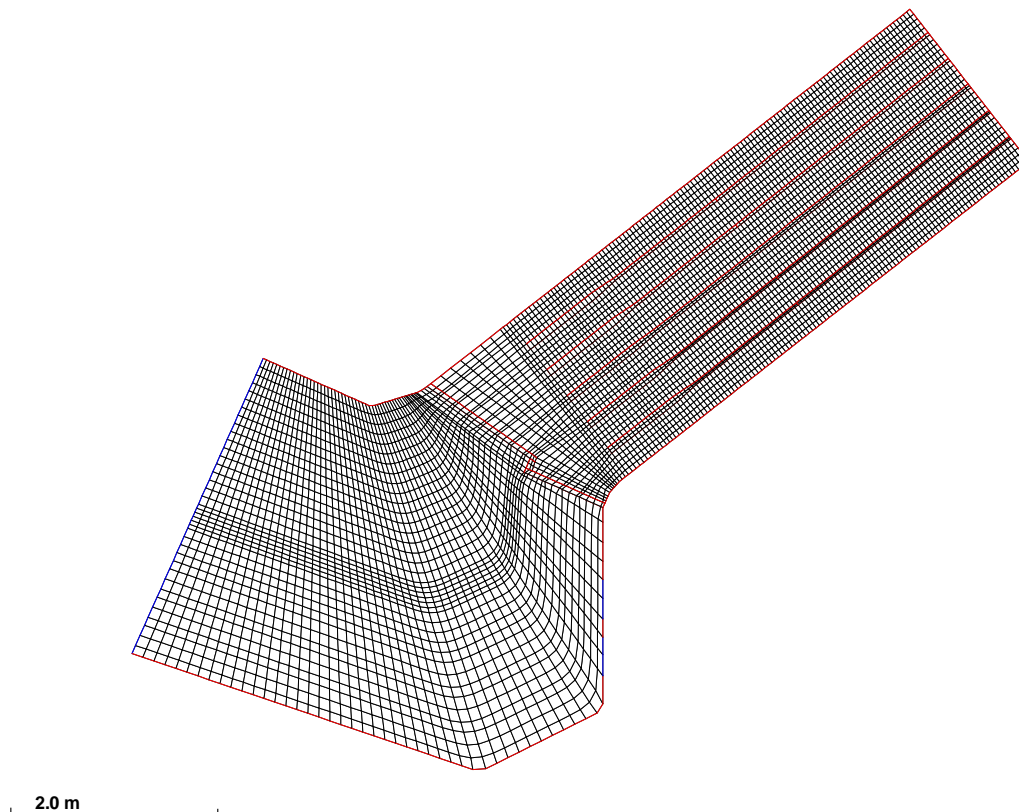


Figure 6.17: Plan view of grid used in initial simulation (model scale, coarse grid resolution) with different orientation. The orientation was obtained by rotating the site orientation by 180° .

Chapter 7

Sediment Simulation

Sediment simulation was carried out to estimate the trap efficiency for different particle sizes for evaluating the performance of the settling basins with recommended design modifications in prototype scale. Besides, the distribution of sediment concentration and bed deposition patterns were also investigated by analyzing the concentration and bed level changes along each bay.

Two different scenarios were simulated. A quasi-steady state without bed changes was modelled in the first case that utilized the results from the hydraulic simulation. *F 68 2* data set was used so that the simulation does not recompute the flow field and update the bed level. While the other case involved recomputation of flow field after the update of bed, invoked by *F 68 0* data set, and so the bed changes were taken into consideration. However, both the simulations considered transient sediment computation (TSC) invoked by *F 37 2* data set and fixed water level across the cross-section. The fine grid resolution with porosity of 0.55 and POW scheme, which produced the best conformity with the measurements in model scale hydraulic simulation was considered for both cases. Four different particle sizes were used in the simulation. The simulation was run assuming water temperature at 20°C and fall velocities were calculated using Rubey's formula (Equation 2.13). However, sensitivity analysis was carried out to assess the performance of the settling basins with the reduced fall velocities for water temperature at 10°C .

7.1 Input Data

The input data for sediment simulation included sediments sizes, fall velocities and concentrations. The inputs for discharge, downstream water level, roughness and porosity were set the same as described in Section 6.5.1. Due to the large seasonal variation in discharges and sediments (Figure 4.3), sediment concentration derived based on whole data series may not be realistic. Therefore, the best estimate was computed as the average of daily concentrations measured from June 15 to October 15, when the sediment and flows are higher, for three years from 2016 to 2018. The inflow sediment concentration was set constant at 3,000 ppm.

The particle sizes and their composition were determined from PSD Table 4.1. Since the concentrations for particle sizes 1 mm and 0.71 mm were negligible compared to rest of the particle sizes, simulations were run only with four size fractions corresponding to particle sizes of 0.5 mm, 0.355 mm, 0.125 mm and 0.09 mm. The volumetric concentration for each size fraction were computed with the sediment density of $2,650\text{ kg/m}^3$. And the simulation time was set as 24 hours (86,400 seconds) for all the cases simulated. However, the time-step of 30 seconds and 100 seconds were adopted for sediment simulation with and without bed changes, respectively. The parameters used for the sediment simulations are outlined in Table 7.1.

Table 7.1 Sediment parameters used for simulation.

Size fraction	Particle size [mm]	Fall velocity ¹ (20 °C) [m/s]	Fall velocity ² (10 °C) [m/s]	% in respective size fraction ³	Volumetric concentration [m ³ /m ³]
1	0.5	0.062	0.059	2.7	3.004×10^{-5}
2	0.355	0.047	0.044	5.0	5.720×10^{-5}
3	0.125	0.012	0.010	55.3	6.274×10^{-4}
4	0.09	0.007	0.005	37.0	4.195×10^{-4}

¹ Fall velocities are calculated using Rubey's formula (Equation 2.13) with dynamic viscosity of $1.002 \times 10^{-3} \text{Ns/m}^2$ (Engineers Edge, 2020).

² Fall velocities are calculated using Rubey's formula (Equation 2.13) with dynamic viscosity of $1.307 \times 10^{-3} \text{Ns/m}^2$ (Engineers Edge, 2020).

³ The values are derived using the % retained in the respective sieve sizes (derived from Table 4.1) and modified to represent 100% in total.

7.2 Input Files

In addition to the *control* file, *koordina* file and the *porosity* file similar to that used in hydraulic simulation, the *timei* file (Appendix D.11) and the *koomin* file (Appendix D.12) were utilized for sediment simulation. However, the *control* file included some additional data sets (*S*, *N* and *B* data sets) describing sediment characteristics, namely sediment fraction number, sediment sizes, fall velocities, composition and distribution. Appendixes D.3 and D.4 show, respectively, the *control* files utilized for sediment simulation without and with bed changes. The additional major data sets (including some extra *F* and *G* data sets) relevant to the sediment simulation are described in Appendix D.4.

The *timei* file included discharge, water levels and sediment concentrations for each size fraction defined by *I* data set. In fact, the *timei* file is used to address the variation in parameters stated earlier in time series computations. However, the parameters were assumed constant throughout the time period of 24 hours in the current simulation. Besides, the file included 1,680 *O* data sets describing output control for variables (concentrations in present case), i.e., the cell indexes and size fractions, so that the corresponding concentrations are listed in *timeo* file for determining trap efficiency. The data sets used in the *timei* file are described in Appendix D.11.

The *koomin* file similar in format of the *koordina* file, was used to specify the minimum bed surface level for bed changes.

7.3 Results

7.3.1 Simulation without Bed Changes

Figure 7.1 shows the trap efficiencies of settling basins for each particle size with respect to the time of computation. Trap efficiencies were derived from the average concentrations at the intake (serving as the inlet of settling basins) and outlet of the basins. The concentrations were obtained from the *timeo* file, which lists the values for concentrations of each size fraction in cells as defined with *O* data set in the *timei* file.

The overall trap efficiency is found to be 76%. The trap efficiencies estimated for particle sizes 0.5 mm and 0.355 mm are 100% while for particle sizes 0.125 mm and 0.09 mm are 82% and 58%, respectively. The sediment flux entering the intake is around 430 kg/s out of 3,600 kg/s supplied at the river inlet. And the sediment flux at the outlet of settling basins is about 104 kg/s.

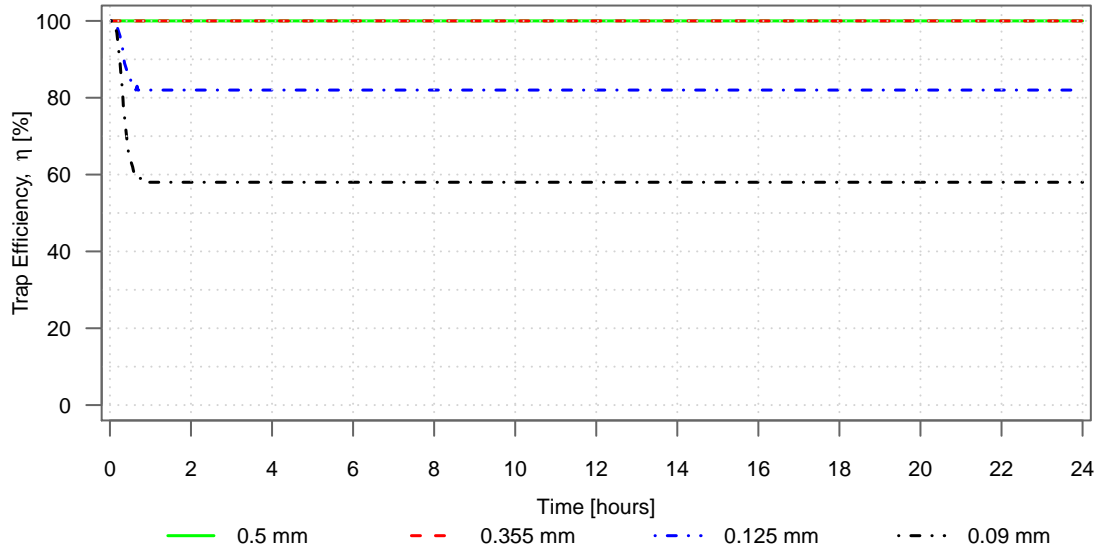


Figure 7.1: Trap efficiencies for each size fraction with respect to the time of computation for simulation without bed changes and water temperature at 20 °C.

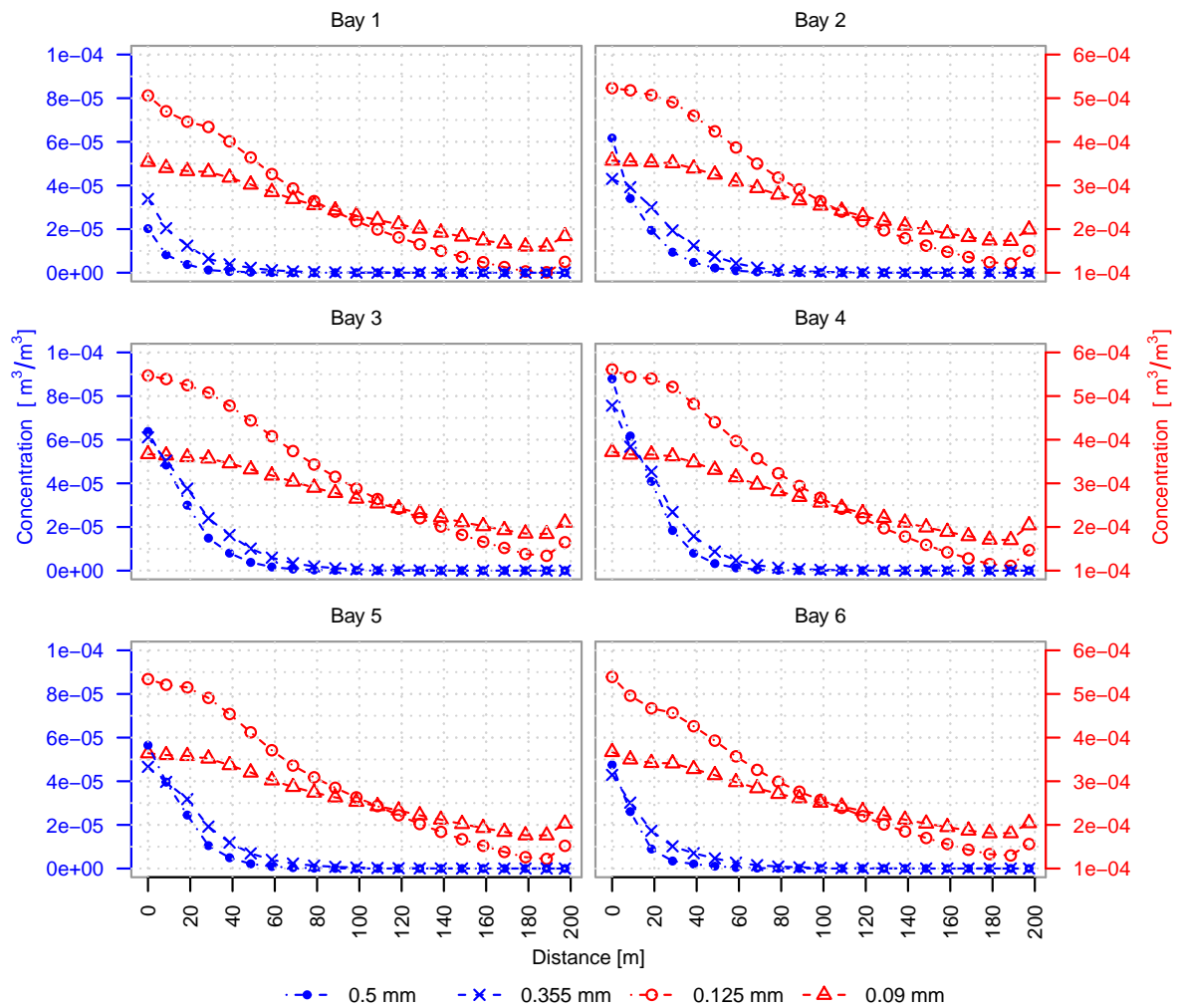


Figure 7.2: Computed depth-averaged concentration for each size fraction along the mid-way of each bay from intake to basin outlet for water temperature at 20 °C. The distances are taken with reference to the intake indicated by 0, which serves as the inlet for the settling basins.

Figure 7.2 shows the change in computed depth-averaged concentration of each size fraction along the mid-way of each bay from intake to outlet of settling basins. The concentration decreases along the basin length, with a considerable reduction in larger sediment sizes within the first half of the basin. Almost all of the sediment of sizes 0.5 mm and 0.355 mm settle within a distance of 100 m from the intake. However, smaller particles show a relatively lower reduction in concentration and tend to flow along and out of the settling basins. A slight increase in concentrations of smaller size fractions at the end of settling basins is observed for all the bays, which can be due to the obstruction caused by the end wall. Besides the reduction of the sediment concentration along the basin, the particle sizes exiting are refined, containing only sediments of sizes 0.125 mm and 0.09 mm .

Figure 7.3 shows computed sum of the depth-averaged concentration along the mid-way of each bay. Despite passing an equal discharge of $23.5\text{ m}^3/\text{s}$ in each bay, the sediment loading is not uniform among the bays. Bay 1 is fed with the lowest sediment concentration, while Bay 4 is supplied with the highest. The difference in sediment flux between these bays is around 11.5 kg/s . However, the trend in the decrease in concentration is similar in each bay, including a slight increase at the end.

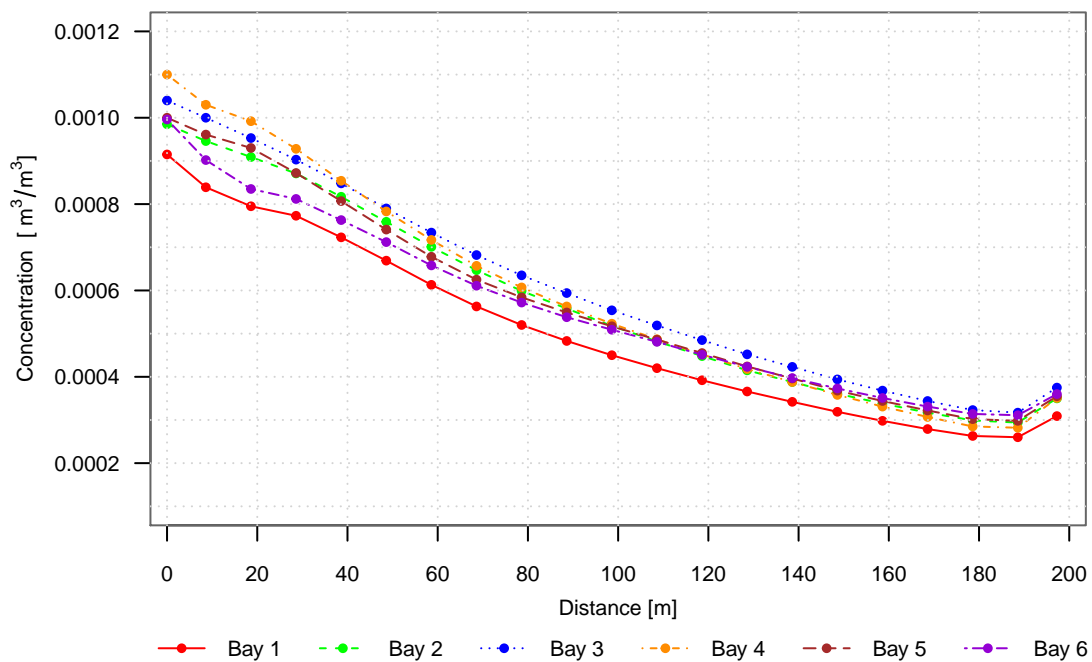


Figure 7.3: Computed sum of depth-averaged concentration along the mid-way of each bay from intake to basin outlet for water temperature at 20°C .

7.3.2 Simulation with Bed Level Changes

The previous simulation estimated trap efficiency without considering the bed movement. However, bed changes occur in the geometry due to the accumulation of the sediments. The decrease in sediment concentration, mostly of coarser particles as seen in Figure 7.2, suggests that deposition starts right from the entrance. For a discharge of $141\text{ m}^3/\text{s}$ passing through the basins, 326 kg/s of sediment flux equivalent to more than a thousand tons are being trapped each hour. These deposits reduce the flow area, thereby increasing the velocity, which will affect the trap efficiency. Simulation considering the bed changes is, therefore, useful to estimate the variation in the trap efficiency for increasing mass of deposits over time. In addition, deposition pattern of sediment may be found, which can serve for the design of an efficient flushing system (Olsen and Kjellesvig, 1999).

Figure 7.4 shows the trap efficiencies of settling basins for each particle size with respect to the time

of computation for simulation with bed changes. The figure depicts the gradual decrease in trap efficiencies for smaller size fractions over time as the deposition increases. The overall trap efficiency is lowered to 69% at the end of simulation. The trap efficiencies estimated for particle sizes 0.5 mm and 0.355 mm are still 100% while for particle sizes 0.125 mm and 0.09 mm are reduced to 78% and 55%, respectively, for a 24 hours simulation.

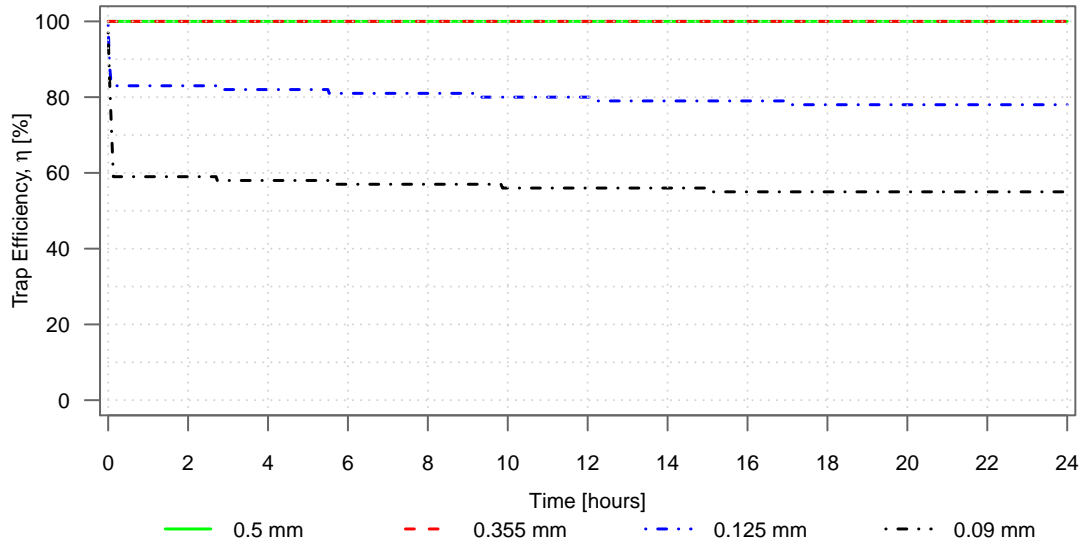


Figure 7.4: Trap efficiencies for each size fraction with respect to the time of computation for simulation with bed changes and water temperature at 20°C.

Bed level changes along the mid-way in each bay are shown in Figure 7.5 at various times. The accumulation of sediments initiates close to the intake for all the bays, corresponding to the decrease in the sediment concentration observed in Figures 7.2 and 7.3. The deposition increases and attains the highest amplitude well within the inlet transition. The maximum bed level changes of more than 2 m are observed in Bays 2, 3 and 4, and for the remaining bays, the depositions are slightly lower. The erosion of deposition is not apparent, as observed in Figure 7.5. However, a small shift of the deposits in Bays 3 and 4 is visible near the intake. Also, a depression can be noticed in all the bays, just prior to the end of inlet transition suggesting the redistribution or erosion of the deposits. The magnitude of the deposit then starts decreasing gradually along the basin length. Besides, the bed level changes show an increase over time.

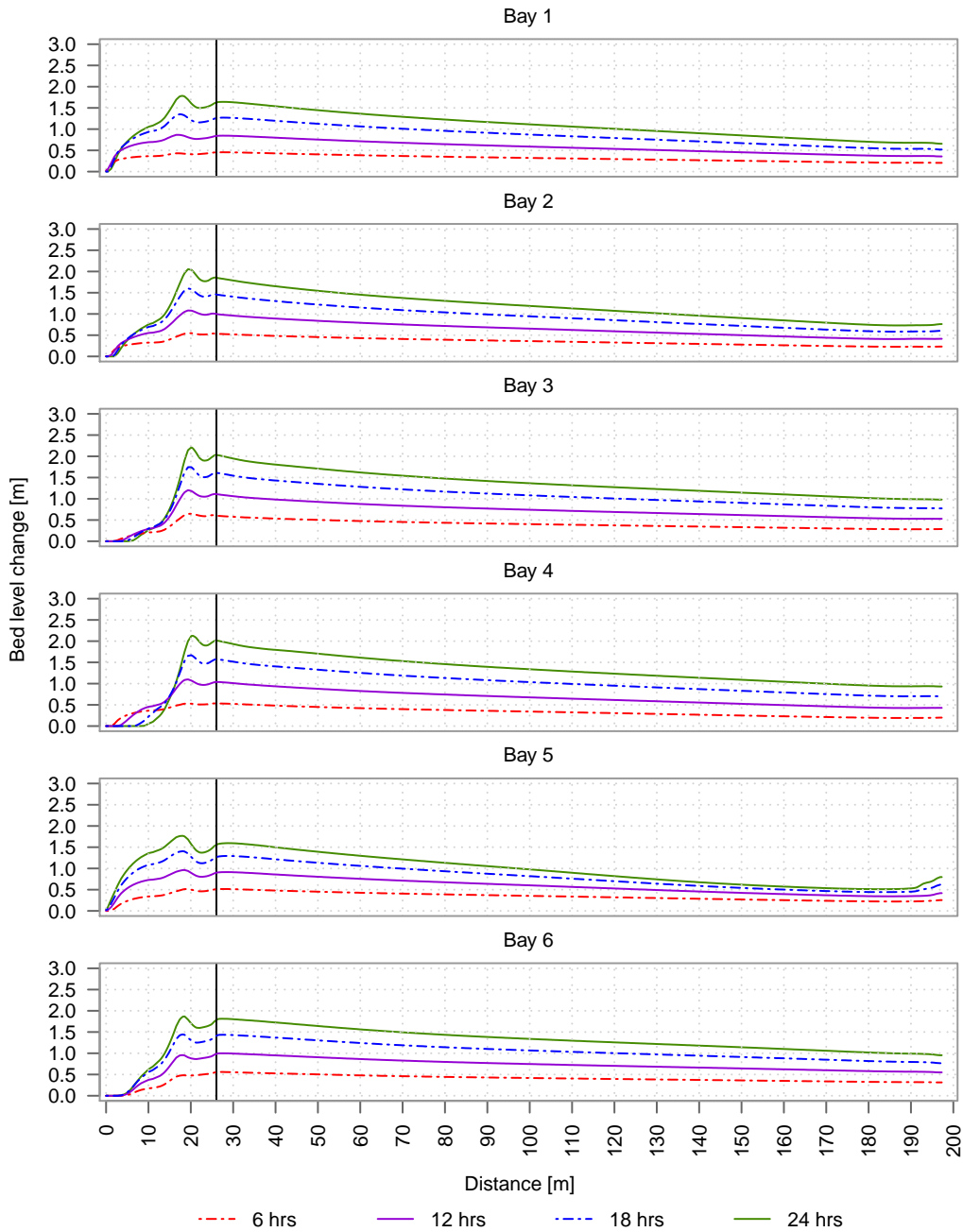


Figure 7.5: Computed bed level changes along the mid-way in each bay at an interval of 6 hours for simulation with water temperature at 20°C. The distances are taken with reference to the intake indicated by 0 and the vertical line between 20 and 30 represents the end of the inlet transition.

7.4 Sensitivity Analysis

The original simulations involved the fall velocities of sediment particles, assuming water temperature at 20°C. However, temperature variation in the water is expected. The fall velocity increases at a higher temperature, thereby increasing the trap efficiency. On the contrary, with lower temperature, the fall velocity decreases with an adverse impact on the trap efficiency. Hence, the reduced water temperature at 10°C was used in the sensitivity analysis to assess the effect of the decrease in fall velocity on the performance of the settling basins. The input data for the simulation were similar to that for water temperature at 20°C, excluding the fall velocities. The sediment parameters used for the simulations are outlined in Table 7.1.

7.4.1 Results

Figures E.3 and E.4 show the trap efficiencies of settling basins for each particle size with respect to the time of computation for the simulations without and with bed changes, respectively. For the former case, the overall trap efficiency is 67%. The trap efficiency estimated for particle sizes 0.5 mm and 0.355 mm are still 100% while for particle sizes 0.125 mm and 0.09 mm are 74% and 44%, respectively. The sediment flux entering the intake is around 433 kg/s out of 3,600 kg/s supplied at the river inlet. And the sediment flux at the outlet of settling basins is about 144 kg/s. While for the latter case, the overall trap efficiency is decreased to 60%. The trap efficiencies for larger particle sizes are still maintained at 100% while for the particle sizes 0.125 mm and 0.09 mm are reduced to 70% and 41%, respectively, for a 24 hours simulation.

Figure E.5 shows the change in computed depth-averaged concentration of each size fraction along the mid-way of each bay from intake to outlet of settling basins. The trend in the decrease in concentrations for sediment sizes 0.5 mm and 0.355 mm is almost the same compared to that observed for water temperature at 20 °C, however, with small variation at the inlet concentrations (Figure 7.2). Almost all of the sediment of these sizes settle within 100 m from the intake. Similarly, the smaller particles of sizes 0.125 mm and 0.09 mm show a relatively lower rate of decrease as depicted by the slightly reduced gradient of the curves, compared to that observed for water temperature at 20 °. Also, the concentrations of these size fractions at the end of the settling basins are comparatively higher.

Figure E.6 showing the computed sum of the depth-averaged concentration along the mid-way of each bay, although appears indistinguishable from Figure 7.3, shows a slower decrease in the sediment concentration. This is evident from a relatively lower gradient and higher concentrations at basins end, indicating an increased amount of sediment escaping out of the basins.

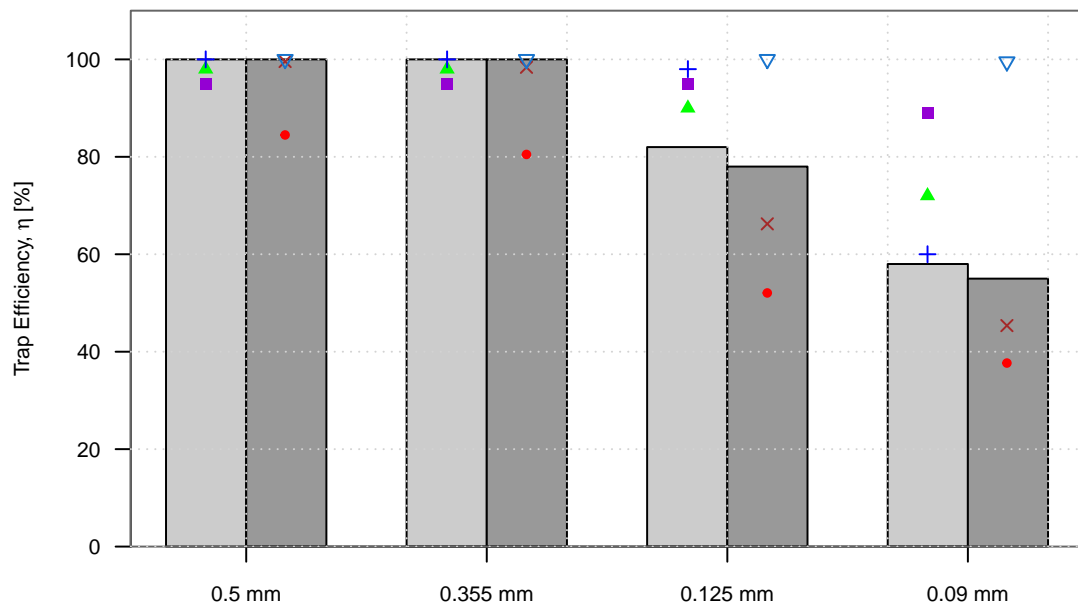
Bed level changes along the mid-way in each bay are shown in Figure E.7 at various times. The bed deposition pattern, including the depression before the end of inlet transition, is similar to that observed for water temperature at 20 °C (Figure 7.5), however, with a lesser magnitude of deposition. The maximum bed level changes of more than 1.5 m are observed in all of the bays, with relatively higher magnitudes in Bays 2, 3 and 4 compared to other bays.

7.5 Comparison with Analytical Method

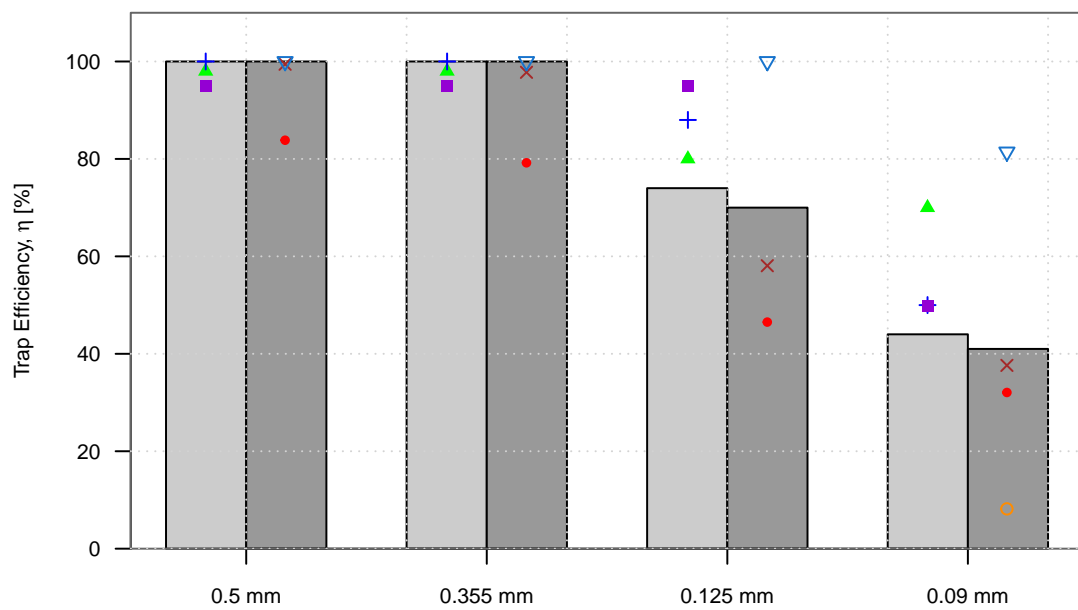
Figure 7.6 shows the comparison of trap efficiencies estimated by different analytical methods for two different water temperatures with that estimated from the simulations. The analytical methods by Velikanov, Camp, Vetter, Garde et al. and Raju et al. estimated similar values for trap efficiency for larger sizes. However, all of these approaches estimated higher trap efficiency for smaller sizes except Vetter's method. And Hazen's method seems to be quite conservative as depicted by the lower trap efficiency for all the sizes under consideration. Sumer's method was not compatible with the current case (water temperature at 20 °C) since all the values for β were greater than 4 (See Item 5 in Section 2.6.4). Nevertheless, the method applied for the smallest size fraction for lower fall velocity (water temperature at 10 °), which produced a significantly lower value as compared to the value estimated from the simulation. The details of calculation for trap efficiency using analytical methods are provided in Appendix C.

7.6 Problem Encountered

Convergence problem was observed in the simulation with bed changes. The simulation with time-step of 100 seconds diverged. So, the time-step was reduced to 30 seconds, which improved the convergence, however, with substantially increased computational time (as long as nine days for a single simulation of 24 hours). Consequently, the simulation for sensitivity analysis was confined only to different fall velocities.



(a)



(b)

Figure 7.6: Comparison of trap efficiencies for different particle sizes estimated using different analytical approaches and from simulation, with water temperature at (a) 20°C and (b) 10°C. The details of calculation are provided in Appendix C.

Chapter 8

Discussion

As presented in Chapter 6, similar settings as in the physical hydraulic model with simplifications were adopted to reproduce the velocities in the numerical model. After numerous simulations run with different parameters, whilst the results at some locations exhibit a good correspondence with the measurements, discrepancies still persist in some instances. This chapter analyzes the results in Chapter 6 obtained from the simulations, particularly with a focus on the possible reasons for deviations noticed between the results from physical and numerical models, including those detected in the numerical models with different computational configurations. Besides, the outcomes presented in Chapter 7 are also discussed, including the evaluation of the performance of the settling basins with recommended design modifications. Since the study is focused on hydraulics and suspended sediment transport at intake and settling basins, the results observed in other parts of the numerical model are not considered in the discussion.

8.1 Model Scale Simulation

Increasing the number of grid cells and application of higher-order scheme can reduce false diffusion, thereby improving the accuracy in a numerical model (Olsen, 2017, ch. 6). The simulation showed the best results obtained with the increase in the number of grid cells. Whereas with the higher-order scheme, i.e., with SOU scheme, the results changed marginally and hence results from the simulation with POW scheme only, are presented and discussed. Reduction in false diffusion while using fine grid resolution explains a more uniform flow field and shorter recirculation zone as compared to that with coarse grid resolution (Figures 6.5 and 6.6). However, the existence and length of the recirculation zone could not be verified as measurements adjacent to the inlet transition were not available.

The deviation of flow jets towards the left or right side of the bays can possibly be due to the short inlet transition and the recirculation zone formed around it (Figures 6.5 and 6.6). However, changing the grid resolution made the flow jets in Bays 1, 3 and 6 follow the opposite side. A similar phenomenon was observed in the investigation by Almeland et al. (2019). The authors further mentioned that this has a little significance for sediment settling and sand trap efficiency, provided the flow features are comparable. They identified from the investigation that the solutions of the Navier-Stokes equations are not unique.

The flow appears to be redistributed due to the effect of control at the intake and the porosity used to represent the wire mesh. The velocities at intake computed from the simulation with fine grid resolution show a better conformity with the measured (Figure 6.7). Nevertheless, higher velocity is observed for both grid resolutions at the intake in Bay 5. Although no significant influences of the approach flow in the forebay on the flow in settling basins are observed, the flow jet directed obliquely towards the guide wall between Bays 5 and 6, (Figure 6.5) can be the potential cause for

the larger deviation. The flow jet is formed due to the sudden change in the forebay wall such that the piers adjacent to the flow jet are not placed on the same line (Figures 6.1 and 6.2 or Figure B.5).

Whilst the vertical profiles of velocities in streamwise direction show a better resemblance after SB7, they deviate strongly in the sections prior to SB7 (Figure 6.8). The discrepancies in the upstream sections can be due to the effect of recirculation zones and the change in the slope from 100% in the inlet transition to 1% in the settling basins within a short distance. The use of vertical walls instead of side slopes may have produced larger differences in Bay 1 and 6 (Figure B.4). Moreover, acrylic material forming the side slopes Bays 1 and 6 is smoother than cement and plywood used in the physical hydraulic model. So, the roughness of 2 mm assumed for the entire geometry, may not reproduce the actual effect.

Besides, the plywood used in the physical model has painted surfaces, which is smoother than the assumed roughness. The larger deviations in velocities closer to bed may be due to the higher roughness adopted (Figure 6.9). However, velocities near the surface are closely replicated with an exception in Bay 1, which can be due to the influence of the artificially introduced vertical boundary wall in the forebay (See Item 2 in Section 6.2 and Figures 6.1 and 6.2) together with the issues stated earlier.

Other possible sources of deviations include additional simplifications made in the geometry (See Section 6.2) and unequal cell sizes while attempting to define the actual size, location and orientation of different structures in the numerical model. Besides, errors due to numerical approximations and possible bugs in the program can also produce inaccuracies.

8.2 Prototype Scale Simulation

Unlike the wire mesh, used in the physical hydraulic model, which has a similar number of horizontal and vertical elements, there exists the trash rack with arrays of vertical bars connected by horizontal bars (very less in number compared to vertical bars) in the prototype. Hence, it is difficult to justify that the porosity approach can physically represent the trash rack. However, it should be noted that the area covered by the bars (20 mm in diameter with 25 mm of spacing in between) in the existing trash rack is around 44% of the total area meaning water can pass through rest 56% of the trash rack area, which is similar to the calibrated porosity value of 55% used in the simulation.

The flow field obtained from the hydraulic simulation in prototype scale (Figure 6.10) shows a reasonable consistency with that from the simulation in model scale with fine grid resolution (Figure 6.5b). The flow direction differs in Bay 3, which can possibly be due to the adjustment of porosity levels to avoid convergence issue in prototype scale simulation (See Section 6.5.1). Nevertheless, the velocity profiles (Figures 6.15 and 6.16) show a similar resemblance, as are observed for the model scale simulation with fine grid resolution (Figures 6.8 and 6.9). The reasons discussed in Section 8.1 are equally relevant for the discrepancies observed between the simulated and the upscaled measured velocities.

Considerable decrease in the velocity is observed along the length of the settling basins with the flow field being gradually more homogeneous (Figure 6.10), which has a positive effect on particle settling. Besides, the small values for the bed shear stress at intake and settling basins (Figure 6.14) suggest no or very low erosion of the settled particles, which is beneficial for the efficient operation of the settling basins. These provide the possible explanations for the limited shift of deposition in Bays 3 and 4 near the intake, and no evident erosion in other bays (Figure 7.5). Since the deposition initiates very close to the intake, low bed shear stress at the intake can be an issue. The deposition may increase further without erosion, thereby increasing the velocity, which is unfavourable for the particle settling downstream. The depression observed prior to the end of the inlet transition, indicating possible erosion, is due to the recirculation zones (Figure 6.13).

The trap efficiencies estimated from the simulation with bed changes show a gradual decrease in

magnitude for smaller size fractions with respect to the time of computation, compared to those estimated from the simulation without bed changes (Figures 7.1 and 7.4). This is mainly due to the vertical growth of deposit over time (Figure 7.5), which decreases the cross-sectional area, thereby increasing the velocity less favourable for particle settling. Almost all of the sediments passing through the settling basins belong to finer fractions (0.125 mm and 0.09 mm), which signifies that a small variation in the amount in finer fractions can significantly affect the overall trap efficiency. The effect of the reduced fall velocities and different simulation scenarios (with and without bed changes) are realized only for the particle sizes of 0.125 mm and 0.09 mm, owing to their higher presence compared to coarser size fractions (Table 7.1).

Although promising results are obtained from sediment simulation, inaccuracies and uncertainties can be expected. In addition to the errors due to numerical approximation and bugs, errors may occur due to the inaccuracy of empirical formula for sediment concentration and the use of time-dependent computations where convergence may not be attained for each time-step. Also, most of the velocities computed from the hydraulic simulation are underestimated compared to measured, potentially affecting the results. Furthermore, the simulations do not take into account the bed forms and change in roughness over time due to deposition of sediments.

8.3 Performance Evaluation

Figure 4.5 shows the trap efficiencies for the existing arrangements, from 2016 to 2018, computed from the daily measured sediment concentration at the inlet and outlet of settling basins. The higher trap values mostly pertain to the days with lower sediment inflows, and in some instances, negative trap efficiencies are also recorded. Besides, the trap efficiency calculated may not be representative as only one measurement per day is taken for sediment concentration. Hence, the median value is opted as the reference to evaluate the performance of the settling basins with design modifications. Furthermore, unlike the mean values, the median values avoid the effect of extreme values recorded.

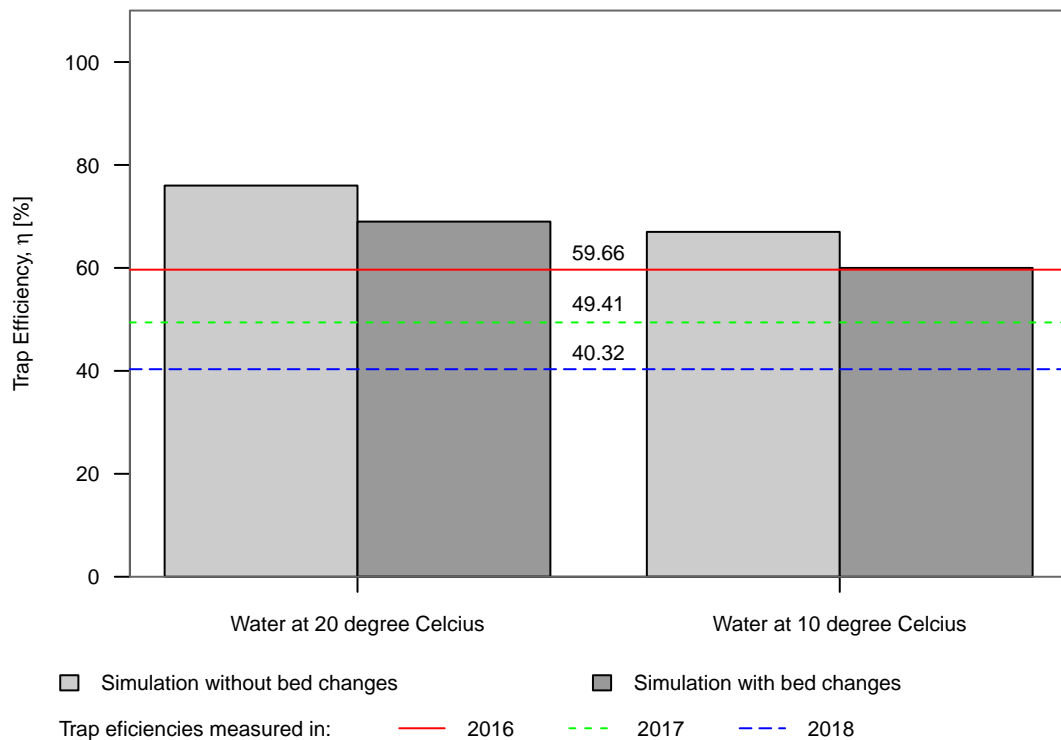


Figure 8.1: Comparison of overall trap efficiency estimated from simulation with measured trap efficiency.

Figure 8.1 shows the comparison between the estimated overall trap efficiency of the settling basins with design modifications from simulation and measured trap efficiency in the existing structure. Since only the suspended sediments belonging to sand-size were simulated, the comparison is limited to the measured values derived for sand concentration. Moreover, sand-size particles are more crucial for turbine erosion compared to silt or clay size particles.

The overall trap efficiencies estimated from the simulation for water temperature at 20°C are greater than the observed values for all three years. The efficiency is improved by 9% and 16% compared to the observed trap efficiency in 2016 (highest among the years considered), respectively, for simulation with and without bed changes. The improvement is even larger if the observed values in 2017 or 2018 are considered.

For water temperature at 10°C, the estimated trap efficiency is reduced due to low fall velocity. However, the magnitude is still greater than observed values for all three years, for the simulation without bed changes. While for the simulation with bed changes, the estimated value is very close to the observed value in 2016. Nevertheless, if the year 2017 is considered, the efficiency seems to improve by 10% and 17%, respectively, for simulation with and without bed changes. These figures are even higher (19% and 26%) with reference to the observed trap efficiency in 2018.

Chapter 9

Conclusion

The 3D numerical model presented in the study is able to reasonably replicate the velocities at intake and velocities (streamwise direction) closer to the surface and at downstream sections of the settling basins, as measured in the physical hydraulic model. Larger deviations are seen for the rightmost and leftmost bays compared to other bays. However, the algorithms can be further improved, potentially enhancing the accuracy of the results. The porosity approach is successfully applied in the numerical model to represent the effect of wire mesh (trash rack in the prototype), provided that the physical representation is ignored. The simulations showed that the velocity field is more sensitive to porosity and porosity levels compared to the roughness height.

Analytical methods for estimating trap efficiency may not be sufficient to ensure an effective headworks design. These methods are based on basin geometry and can not account for the effect of approach flow condition. Also, it is difficult to choose among the several approaches available; the results differ for different methods for the same basin geometry and particle size. Furthermore, these methods do not consider the relative composition of different particle sizes. Similarly, it is difficult to simulate especially the finer suspended sediments in the physical hydraulic model owing to the practical issues with scaling these particles. The current study indicates 3D numerical model can be a useful tool to mitigate these issues and supplement the physical hydraulic model in simulating sediments. Trap efficiencies are predicted in the study to evaluate the performance of the settling basins with recommended design modifications, together with sediment concentration distribution and bed level changes. Moreover, hydraulic simulation conveniently provided details on velocity fields, bed shear stress, including detection of the recirculation zones. However, the recirculation zones observed in the numerical simulation could not be confirmed due to the lack of data around the inlet transition.

Two different simulation scenarios (with and without bed changes) and two different fall velocities (corresponding to water temperatures at 20°C and 10°C) were investigated for the sediment simulation in the prototype scale. One of the important results from the simulations is trap efficiency. Significant improvement in the trap efficiency of the settling basins is observed for the modified geometry in comparison to the performance exhibited by the existing structure in recent years, even with reduced fall velocity (water temperature at 10°C). The improvement in trap efficiency compared to the values observed in 2018, is as high as 19% and 26%, respectively, for the simulations with and without bed changes. Nevertheless, the simulation time was limited to 24 hours, and hence the values are expected to decrease with an extended simulation time for the simulation with bed changes. The simulations showed that the reduction in fall velocity has a significant influence on the trap efficiency, and less effect on sediment concentration distribution and bed deposition patterns. However, the rate of decrease in sediment concentration and magnitude of deposition along the bays are lowered.

Chapter 10

Future Works

Various simplifications were adopted; some directly related to the limitations in the software, tapering guide walls substituted by vertical elements with average thickness and vertical walls instead of side slopes. These are among the potential reasons liable for deviation in the results compared to the measured. Other CFD programs with possibility of using triangular and nested grids may be utilized to best represent the geometry. This could not only verify the obtained results plus the recirculation zones (which were not identified in the physical model test) but also serve for investigating the validity of the use of porosity approach to represent the trash rack.

The physical hydraulic model was constructed using different materials with different roughness, and roughness varies in the prototype as well. However, a constant roughness height was used for both the cases (2 mm and 3 mm, respectively for model scale and prototype scale simulation). Different roughness can be introduced corresponding to the materials and locations, with potential improvement in the results obtained from the current work.

Due to the time constraints and unexpectedly long simulation time, sensitivity analysis for sediment simulation was limited only to different fall velocities for two different water temperatures. However, more parameters can be varied; for example, time-step, number of iterations, sediment pick-up rate, Shield's coefficients, van Rijn's coefficients, turbulence model, etc. This can be advantageous to evaluate the influence of input parameters, thereby identifying uncertainties and making results more robust and reliable.

A constant inflow of discharge and sediment was only modelled in the current work. However, it is possible to further investigate the scenarios with variable inflow as they occur in nature. Besides, higher flows than currently used may be simulated to predict if the arrangement can handle the flow without a significant impact on the plant operation, for instance, with a two-year flood.

The current work is restricted to hydraulic and sediment simulation intended to estimate trap efficiency, concentration distribution and bed deposition pattern. The collector channel gate openings at the end of basins were not simulated; instead, uniform distribution of discharge was assumed among the bays. However, the sediment loads among the bays are not uniform, as discovered from the current simulation. The numerical model can be expanded to investigate different gate openings to evaluate the sediment distribution, which may suggest a more efficient set-up. Furthermore, utilizing the physical hydraulic model to solve the problem is difficult, and the numerical model can simplify the case.

The bed deposition outputs obtained from the simulation can be utilized for flushing simulation, possibly using SSIIM 2. Information on flushing time required, flushed volume, etc. can be produced, which can be valuable for optimal operation of the arrangements. Besides, simulation can be run for a longer time duration, for example, 48 hours or 72 hours or even more, for analyzing the further reduction in trap efficiency and change in bed deposition. Such information is

beneficial in determining the flushing time interval so that it is possible to devise an effective operational strategy. Similarly, the model may be extended to test alternative modifications other than recommended, which can potentially be more efficient.

Bibliography

- Almeland, S.K., Olsen, N.R.B., Bråveit, K. and Aryal, P.R., 2019. Multiple solutions of the Navier-Stokes equations computing water flow in sand traps. *Engineering applications of computational fluid mechanics*, 13(1), pp.199–219. <https://doi.org/10.1080/19942060.2019.1566094>.
- Anderson, J.D., 2009. Basic Philosophy of CFD. In: *Computational Fluid Dynamics*. Ed. by J.F. Wendt. Berlin, Heidelberg: Springer. Chap. 1, pp.3–14. ISBN: 978-3-540-85056-4. https://doi.org/10.1007/978-3-540-85056-4_1.
- Annandale, G.W., Morris, G.L. and Karki, P., 2016. *Extending the Life of Reservoirs: Sustainable Sediment Management for Dams and Run-of-River Hydropower*. The World Bank. <https://doi.org/10.1596/978-1-4648-0838-8>.
- Avery, P., ed., 1989. *Sediment Control at Intakes- A Design Guide*. Settling Basins. BHARA Process Engineering Division. Chap. 7, pp.79–102.
- Biswhwakarma, M.B., 2015. Settling Basin Design Criteria and Trap Efficiency Computation Methods. *Civil engineering voice*, 1.
- Biswhwakarma, M.B., 2018. Performance improvement of headworks: a case of Kaligandaki A Hydropower Project through physical hydraulic modelling. 2nd International Symposium on Hydraulic Modelling and Measuring Technology.
- Blazek, J., 2015. *Computational Fluid Dynamics: Principles and Applications*. 3rd ed. Oxford: Butterworth-Heinemann. <https://doi.org/10.1016/C2013-0-19038-1>.
- Chadwick, A., Morett, J. and Borthwick, M., 2013. *Hydraulics in Civil and Environmental Engineering*. 5th ed. CRC Press, Taylor & Francis Group.
- Chanson, H., 2004. *Hydraulics of Open Channel Flow: An Introduction*. 2nd ed. Oxford: Butterworth-Heinemann.
- Chhetry, B. and Rana, K., 2015. Effect of Sand Erosion on Turbine Components: A Case Study of Kali Gandaki “A” Hydroelectric Project (144 MW), Nepal. *Hydro Nepal*, 17, pp.24–33.
- Chow, V.T., 1959. *Open-channel Hydraulics*. McGraw Hill Book Company, Inc.
- Engineers Edge, 2020. *Water- density viscosity specific weight*. https://www.engineersedge.com/physics/water__density_viscosity_specific_weight_13146.htm. [Accessed 19 May 2020].
- Erdbrink, C.D., Krzhizhanovskaya, V.V. and Sloot, P.M.A., 2014. Free-surface flow simulations for discharge-based operation of hydraulic structure gates. *Journal of Hydroinformatics*, 16(1), pp.189–206. ISSN: 1464-7141. <https://doi.org/10.2166/hydro.2013.215>.
- Ferziger, J.H., Perić, M. and Street, R.L., 2020. *Computational Methods for Fluid Dynamics*. 4th ed. Cham: Springer International Publishing. ISBN: 978-3-319-99691-2. <https://doi.org/10.1007/978-3-319-99693-6>.
- Garde, R.J., Raju, K.G.R. and Sujudi, A.W.R., 1990. Design of settling basins. *Journal of Hydraulic Research*, 28(1), pp.81–91. <https://doi.org/10.1080/00221689009499148>.
- Haun, S. and Olsen, N.R.B., 2012. Three-dimensional numerical modelling of reservoir flushing in a prototype scale. *International Journal of River Basin Management*, 10(4), pp.341–349. <https://doi.org/10.1080/15715124.2012.736388>.

- Hearn, C.J., 2008. *The Dynamics of Coastal Models*. Cambridge University Press. ISBN: 9780521807401.
- Henderson, F.M., 1966. Channel Transitions. In: *Open Channel Flow*. New York, USA: Macmillan. Chap. 7, pp.235–284. ISBN: 0023535105.
- Hu, H.H., 2012. Chapter 10 - Computational Fluid Dynamics. In: P.K. Kundu, I.M. Cohen and D.R. Dowling, eds. *Fluid Mechanics*. Fifth Edition. Boston: Academic Press, pp.421–472. ISBN: 978-0-12-382100-3. <https://doi.org/10.1016/B978-0-12-382100-3.10010-1>.
- Hydro Lab, 2017. *Physical Hydraulic Model testing of Design Modifications of the Headworks of Kali Gandaki A Hydropower Plant, Draft Final Report*. Client: Nepal Electricity Authority (NEA).
- IHA, 2017. Case Study- Kali Gandaki, Nepal. *Sediment Management*.
- Isaac, N. and Eldho, T.I., 2016. Sediment management studies of a run-of-the-river hydroelectric project using numerical and physical model simulations. *International Journal of River Basin Management*, 14(2), pp.165–175. <https://doi.org/10.1080/15715124.2015.1105234>.
- Julien, P.Y., 2010. *Erosion and Sedimentation*. Second Edition. Cambridge University Press. ISBN: 9780521830386.
- Koirala, R., Thapa, B., Neopane, H.P, Zhu, B. and Chhetry, B., 2016. Sediment erosion in guide vanes of Francis turbine: A case study of Kaligandaki Hydropower Plant, Nepal. *Wear*, 362-363, pp.53–60. ISSN: 0043-1648. <https://doi.org/10.1016/j.wear.2016.05.013>.
- Lučin, I., Čarija, Z., Grbčić, L. and Kranjčević, L., 2020. Assessment of head loss coefficients for water turbine intake trash-racks by numerical modeling. *Journal of Advanced Research*, 21, pp.109–119. ISSN: 2090-1232. <https://doi.org/10.1016/j.jare.2019.10.010>.
- Lysne, D.K., Glover, B., Støle, H. and Tesaker, E., 2003. Sediment Transport and Sediment Handling. In: *Hydraulic Design*. Norwegian University of Science, Technology, Department of Civil and Environmental Engineering. ISBN: 82-7598-027-5.
- Maintenance Field Visit on Kali-Gandaki Hydropower Project*, 2013. https://www.academia.edu/4201830/Field_Report_Kaligandaki?auto=download. [Accessed 18 February 2020].
- Merkely, G.P., 2004. *Irrigation Conveyance and Control: Flow Measurement and Structure Design*. Lecture-24: Flumes and Channel Transitions, <https://pdfslide.net/documents/irrigation-conveyance-control-flow-measurement-structure-design.html>. [Accessed 1 March 2020].
- Morris, G.L. and Fan, J., 1998. *Reservoir Sedimentation Handbook*. New York.: McGraw-Hill Book Co.
- Mosonyi, E., 1991. *Water Power Development, High-head Power Plants*. Vol. 2/A. Budapest: Akadémiai Kiadó.
- Nøvik, H., Dudhraj, A., Olsen, N.R.B., Biswhwakarma, M.B. and Lia, L., 2014. Numerical modelling of non-uniform flow in settling basins. *Hydro Nepal*, 14, pp.27–35.
- Olsen, N.R.B. and Kjellesvig, H.M., 1999. Three-dimensional numerical modelling of bed changes in a sand trap. *Journal of Hydraulic Research*, 37(2), pp.189–198. <https://doi.org/10.1080/00221689909498305>.
- Olsen, N.R.B. and Skoglund, M., 1994. Three-dimensional numerical modeling of water and sediment flow in a sand trap. *Journal of Hydraulic Research*, 32(6), pp.833–844. <https://doi.org/10.1080/00221689409498693>.
- Olsen, N.R.B., 2015. Four free surface algorithms for the 3D Navier–Stokes equations. *Journal of Hydroinformatics*, 17(6), pp.845–856. ISSN: 1464-7141. <https://doi.org/10.2166/hydro.2015.012>.
- Olsen, N.R.B., 2017. *Numerical Modelling and Hydraulics*. Fifth Edition. Department of Civil & Environmental Engineering, Norwegian University of Science and Technology. ISBN: 82-7598-074-7.

- Olsen, N.R.B., 2018. *A Three-Dimensional Numerical Model for Simulation of Sediment Movements in Water Intakes with Multiblock Option*, *SSIIM User's Manual*. Department of Civil & Environmental Engineering, Norwegian University of Science and Technology.
- Pandit, H.P., 2009. *Sediment Handling in Himalayan Rivers using Hydrocyclones*. PhD thesis. Tribhuvan University.
- Paschmann, C., Fernandes, J.N., Vetsch, D.F. and Boes, R.M., 2017. Assessment of flow field and sediment flux at alpine desanding facilities. *International Journal of River Basin Management*, 15(3), pp.287–295. <https://doi.org/10.1080/15715124.2017.1280814>.
- Paschmann, C., 2018. *Design optimization of desanding facilities for hydropower schemes*. PhD thesis. ETH Zurich.
- Pradhan, P.M.S., 2004. *Improving Sediment Handling in the Himalayas*. Nepal: OSH Research.
- Qamar, M.Z., Verma, M.K. and Meshram, A.P., 2014. Importance of Desilting Basins in Run-of-River Hydro Projects in Himalayan Region. *International Journal of Emerging Technology and Advanced Engineering*, 4, pp.407–412.
- Qiu, B., He, S., Chu, S. and Feng, X., 2014. Influence of Trash-Barrier on Operation of Pumping Station with Wet-Pits. *Advances in Mechanical Engineering*, 2014 (), April, pp.1–7. <https://doi.org/10.1155/2014/419876>.
- Raju, K.G.R., Kothiyari, U.C., Srivastav, S. and Saxena, M., 1999. Sediment Removal Efficiency of Settling Basins. *Journal of Irrigation and Drainage Engineering*, 125(5), pp.308–314. [https://doi.org/10.1061/\(ASCE\)0733-9437\(1999\)125:5\(308\)](https://doi.org/10.1061/(ASCE)0733-9437(1999)125:5(308)).
- Rodi, W., 2017. Turbulence Modeling and Simulation in Hydraulics: A Historical Review. *Journal of Hydraulic Engineering*, 143 (5), pp.53–60. [https://doi.org/10.1061/\(ASCE\)HY.1943-7900.0001288](https://doi.org/10.1061/(ASCE)HY.1943-7900.0001288).
- Rüther, N., Singh, J.M., Olsen, N.R.B. and Atkinson, E., 2005. 3-d computation of sediment transport at water intakes. *Water Management*, 158, pp.1–7.
- Simanjuntak, T., Boeriu, P. and Roelvink, D.J., 2009. Consideration on the Sedimentation Process in a Settling Basin. *Journal of Hydrology and Hydromechanics*, 57(1), pp.16–25. <https://doi.org/10.2478/v10098-009-0002-4>.
- Sinha, S. and Singh, A.P., 2019. Sediment removal efficiency estimation criteria for modern day desilting basins. *ISH Journal of Hydraulic Engineering*, 25(1), pp.104–117. <https://doi.org/10.1080/09715010.2018.1426057>.
- Støle, H., 1993. *Withdrawal of water from Himalayan rivers : sediment control at intakes*. Trondheim: Division of Hydraulic and Sanitary Engineering, Norwegian Institute of Technology, University of Trondheim. ISBN: 8271194933.
- TU Delft, 2020. *Water treatment – sedimentation*. <https://ocw.tudelft.nl/wp-content/uploads/Sedimentation-1.pdf>. [Accessed 1 March 2020].
- USBR, 2006. *Erosion and Sedimentation Manual*. U.S. Department of the Interior Bureau of Reclamation.
- Versteeg, H.K. and Malalasekera, W., 2007. *An Introduction to Computational Fluid Dynamics: The Finite Volume Method*. 2nd ed. Pearson Education Limited. ISBN: 978-0-13-127498-3.
- Wang, Z.Y. and Dittrich, A., 1992. A study on problems in suspended sediment transportation. *Proceedings of the Second International Conference on Hydraulics and Environmental Modeling of Coastal, Estuarine and River Waters*, 2, pp.467–478.
- Wang, Z.Y., Lee, J.H.W. and Melching, C.S., 2015. *River Dynamics and Integrated River Management*. Berlin, Heidelberg: Springer. ISBN: 978-3-642-25651-6. <https://doi.org/10.1007/978-3-642-25652-3>.

Appendix A: Salient Features

Table A.1 Salient Features of KGA (*Maintenance Field Visit on Kali-Gandaki Hydropower Project, 2013*).

A. Headworks		
Reservoir		
Catchment area at the dam site	7,618	<i>sq. km</i>
Average annual flow	288	m^3/s
90% dependable flow	48	m^3/s
Reservoir levels		
Operating Maximum	EL 524.00	<i>masl</i>
Operating Minimum	EL 518.00	<i>masl</i>
Reservoir volume at EL 524.00 <i>masl</i>	7.7	Mm^3
Live storage	3.1	Mm^3
Diversion Dam		
Design flood (1000 yr)	6,400	m^3/s
Type	Concrete gravity	
Lowest foundation Level	EL 483.00	<i>masl</i>
Deck level	EL 526.00	<i>masl</i>
Height of structure	43	<i>m</i>
Crest length (approx.)	110	<i>m</i>
Spillway		
Type	Concrete gravity	
Design flood (1000 yrs)	6,400	
Crest level	EL 505.00	<i>masl</i>
Number and type of Gates	3 radial gates 15 <i>m</i> (W) × 19 <i>m</i> (H) 1 bascule gate 7 <i>m</i> (W) × 7.5 <i>m</i> (H)	
Settling Basin		
Type	Outdoor, open surface	
Flushing operation	Intermittent	m^3/s
Basin top width (each)	40	<i>m</i>
Operating levels		
Maximum	EL 524.00	<i>masl</i>
Minimum	EL 518.00	m^3/s
Number	2 (with 3 chambers in each basin)	
Collector Channel		
Width	7.40	<i>m</i>
Height	18	<i>m</i>
Length (approx.)	88	<i>m</i>

B. Waterways			
Main Tunnel			
Number and type	One concrete lined pressure tunnel		
Length	5,905	<i>m</i>	
Finish diameter	7.40	<i>m</i>	
Lining (nominal)	0.45	<i>m</i>	
Invert level at intake	EL 508.30	<i>masl</i>	
Invert level at surge tank	EL 487.50	<i>masl</i>	
Slope (approx.)	0.35%		
C. Power Plant Facilities			
Surge Tank			
Finish diameter	26.00	<i>m</i>	
Lining thickness (nominal)	1.00	<i>m</i>	
Height	61.5	<i>m</i>	
Gate (W×H)	One emergency wheel gate (5.5 <i>m</i> × 5.5 <i>m</i>)		
Pressure Shaft			
Alignment	Vertical		
Lining	Steel		
Finish diameter	5.50	<i>m</i>	
Height	65.85	<i>m</i>	
Penstock			
Length (projected)	243.00	<i>m</i>	
Diameter	5.25	<i>m</i>	
Powerhouse			
Type	Surface		
Width	21.10	<i>m</i>	
Height	43.20	<i>m</i>	
Length	90.50	<i>m</i>	
D. Generating Equipment			
Turbines			
Type	Francis	<i>m</i>	
Number of units	3		
Rated output/unit	48	<i>MW</i>	
Rated flow/unit @ peak load	47	<i>m³/s</i>	
Design net head	115	<i>m</i>	
Rated speed	300	<i>rpm</i>	
Generators			
Type	3-phase, synchronous		
Number of units	3		
Rated output	56.50	<i>MVA</i>	
Type of construction	Vertical		
Rated voltage	13.80	<i>kV</i>	
Rated frequency	50	<i>Hz</i>	
Power factor	0.85		
Rated speed	300	<i>rpm</i>	
E. Transmission Line			
Transmission line system	132	<i>kV</i>	
Total length	106	<i>km</i>	

Appendix B: Drawings and SSIIM Model

NOTE:

- All dimensions are in *mm* and relate to the prototype (not to the physical hydraulic model).
- All elevation levels are in *masl*.
- The drawings are not in scale.

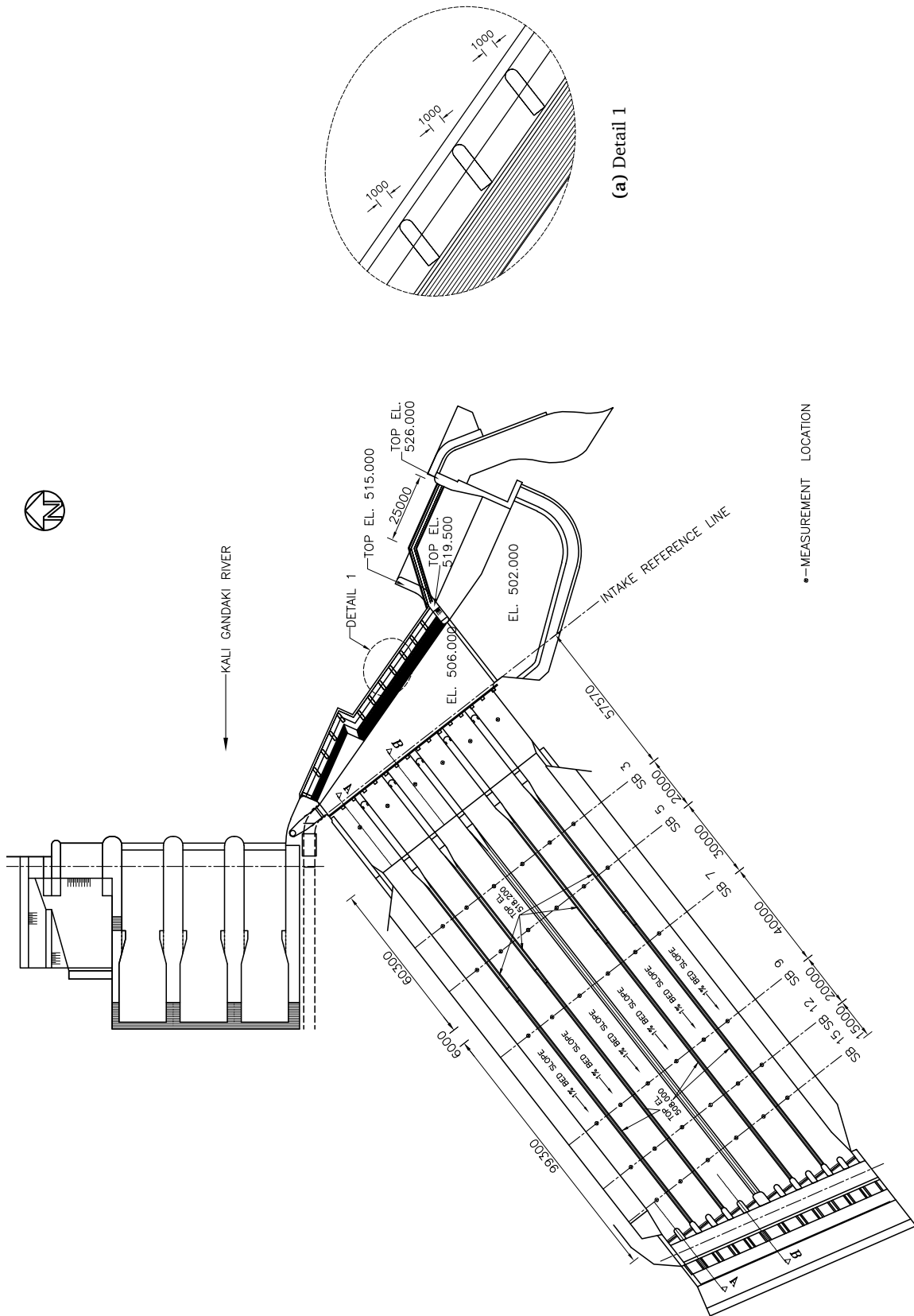


Figure B.1: Plan view of the recommended modifications by Hydro Lab with measurement points and sections.

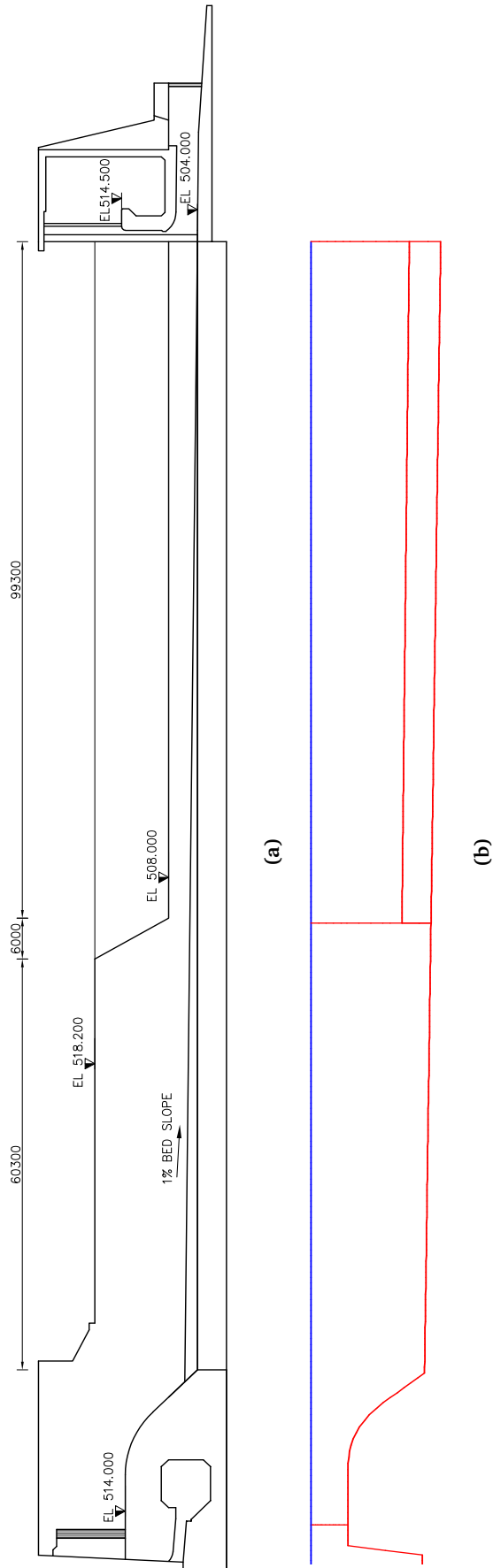


Figure B.2: Longitudinal section A-A, corresponding to Figure B.1; (a) in prototype with modifications and (b) in SSIIM model.

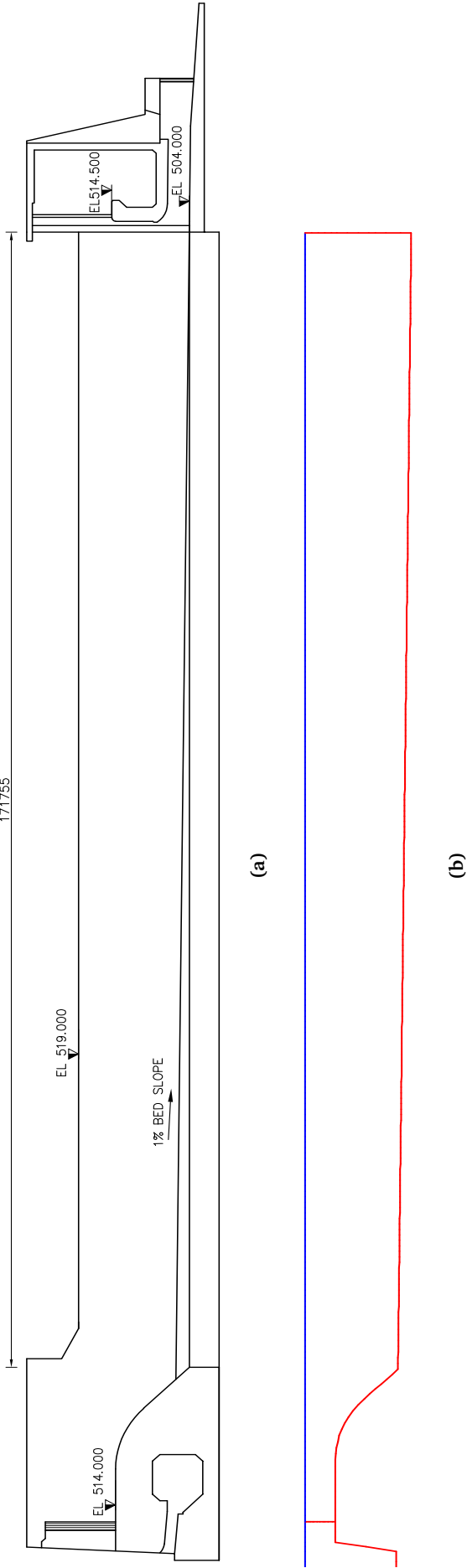
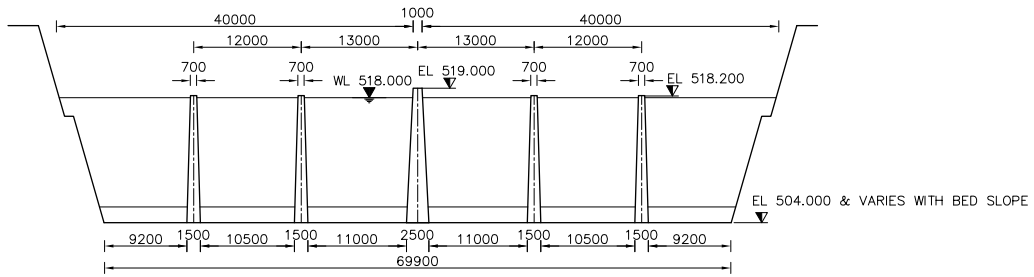
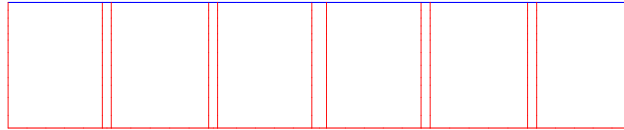


Figure B.3: Longitudinal section B-B, corresponding to Figure B.1; (a) in prototype with modifications and (b) in SSIM model

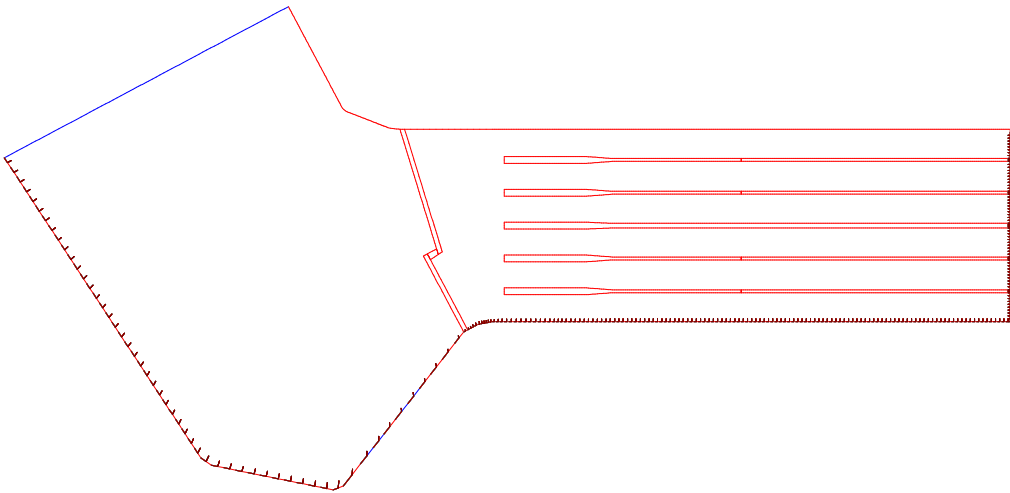


(a)

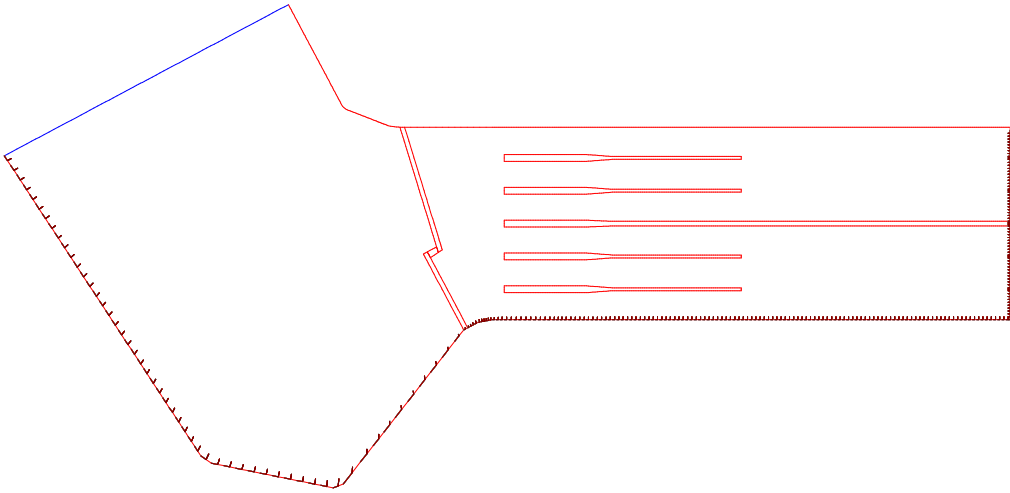


(b)

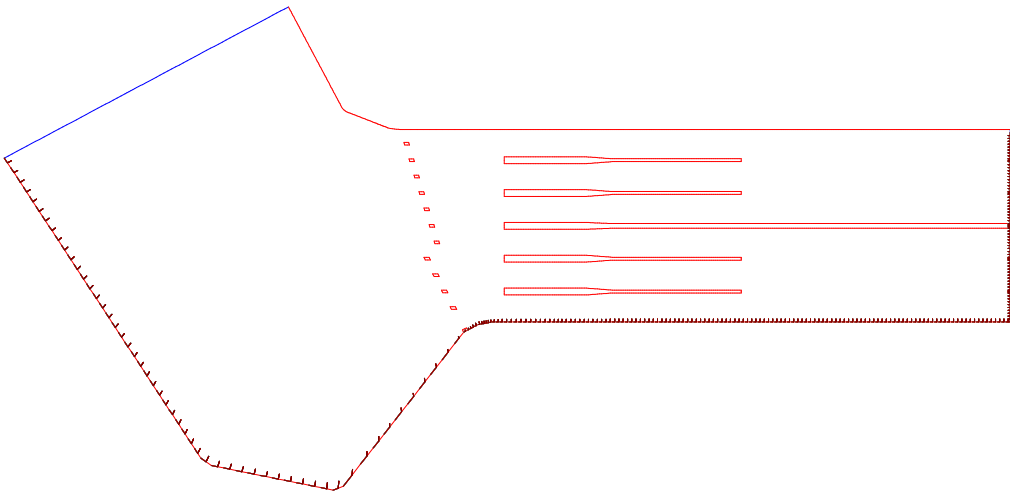
Figure B.4: Cross-section at SB3, corresponding to Figure B.1; (a) in prototype with modifications and (b) in SSIIM model.



(a)



(b)



(c)

Figure B.5: Plan views of SSIIM model at different levels; (a) level 2 showing forebay wall, divide wall and guide walls, (b) level 4 showing the portion of guide walls protruding above 508.00 masl and (c) level 10 showing the piers over forebay wall

Appendix C: Detailed Calculation for Trap Efficiency

Table C.1 Input parameters for calculation of trap efficiency of settling basin.

Design discharge, Q_d	141	m^3/s	
Number of basins, N	2		
Discharge through each basin, Q	70.50	m^3/s	
Number of bays	6		3 bays in each basin
Average length, L	174	m	Measured along the midway of settling basin
Top width, B_t	40	m	
Bottom width, B_b	30.70	m	
Average width, B	35.35	m	
Flow depth, D	14	m	
Flow depth in approach channel, h	4	m	
Manning-Strickler's coefficient, M	90	$m^{1/3}/s$	
Manning's coefficient, n	0.011	$s/m^{1/3}$	
Acceleration due to gravity, g	9.81	m/s^2	
Cross-sectional area, A	494.90	m^2	
Basin surface area, A_s	6150.90	m^2	
Wetted perimeter, P	60.20	m	Assuming a trapezoidal cross-section
Hydraulic radius, R	8.22	m	
Flow velocity, U	0.142	m/s	
Hydraulic gradient, I	1.51×10^{-7}		Using Manning's equation
Shear velocity, u_*	3.49×10^{-3}	m/s	

Table C.2 Trap efficiency computation by Hazen's method, (20°C).

Size fraction	Particle size [mm]	Fall velocity [m/s]	Trap efficiency, η [%]
1	0.5	0.062	84.49
2	0.355	0.047	80.49
3	0.125	0.012	52.06
4	0.09	0.007	37.67

Trap efficiency is calculated using Equation (2.15) with $m = 1$ since $m = 0$ is represented by Vetter's method, See Items 1 and 4 in Section 2.6.4.

Table C.3 Trap efficiency computation by Velikanov's method, (20 °C).

Size fraction	Particle size [mm]	Fall velocity [m/s]	λ	Trap efficiency, η [%]
1	0.5	0.062	4.47	98
2	0.355	0.047	3.39	98
3	0.125	0.012	0.89	90
4	0.09	0.007	0.50	72

The values for λ are calculated with Equation (2.16) and corresponding values of η are obtained from Figure 2.9.

Table C.4 Trap efficiency computation by Camp's method, (20 °C).

Size fraction	Particle size [mm]	Fall velocity [m/s]	wA_s/Q	w/u_*	Trap efficiency, η [%]
1	0.5	0.062	5.45	17.90	100
2	0.355	0.047	4.13	13.55	100
3	0.125	0.012	1.09	3.57	98
4	0.09	0.007	0.60	1.99	60

The values for η are obtained from Figure 2.10 using corresponding values of wA_s/Q and w/u_* .

Table C.5 Trap efficiency computation by Vetter's method, (20 °C).

Size fraction	Particle size [mm]	Fall velocity [m/s]	wA_s/Q	Trap efficiency, η [%]
1	0.5	0.062	5.45	99.57
2	0.355	0.047	4.13	98.38
3	0.125	0.012	1.09	66.24
4	0.09	0.007	0.60	45.36

The values for η are calculated with Equation (2.18).

Table C.6 Trap efficiency computation by Sumer's method, (20 °C).

Size fraction	Particle size [mm]	Fall velocity [m/s]	β	Trap efficiency, η [%]
1	0.5	0.062	44.74	Every values for β are greater than 4 i.e $w/u_* > 1.6$, so this approach is not applicable for the case
2	0.355	0.047	33.87	
3	0.125	0.012	8.92	
4	0.09	0.007	4.96	

See Item 5 in Section 2.6.4.

Table C.7 Trap efficiency computation by Garde et al. method, (20 °C).

Size fraction	Particle size [mm]	Fall velocity [m/s]	w/u_*	η_0 [%]	k	Trap efficiency, η [%]
1	0.5	0.062	17.90	100	0.24	94.94
2	0.355	0.047	13.55	100	0.24	94.94
3	0.125	0.012	3.57	100	0.24	94.94
4	0.09	0.007	1.99	96	0.21	88.94

The values for η_0 and k are obtained from Figure 2.12 and Equation (2.20) is used to compute η .

Table C.8 Trap efficiency computation by Raju et al. method, (20 °C).

Size fraction	Particle size [mm]	Fall velocity [m/s]	w/u_*	Trap efficiency, η [%]
1	0.5	0.062	17.90	100
2	0.355	0.047	13.55	100
3	0.125	0.012	3.57	100
4	0.09	0.007	1.99	99.52

As there is no horizontal expansion, the width of approach channel, b as required in Equation (2.21) to compute η , is assumed to be the same as that of settling basin, i.e., $b = B$.

Table C.9 Trap efficiencies estimated using different analytical approaches for water temperature at 10 °C.

		Size fraction (Particle size [mm])			
		1 (0.5)	2 (0.355)	3 (0.125)	4 (0.09)
Trap efficiency η [%]	Hazen's method ¹	83.84	79.20	46.51	32.06
	Velikanov's method	98	98	80	70
	Camp's method	100	100	88	50
	Vetter's method	99.44	97.78	58.08	37.62
	Sumer's method	<i>Not applicable for $w/u_* > 1.6$</i>			8.17
	Garde et al. method	94.94	94.94	94.94	49.80
	Raju et al. method	100	100	100	81.43

¹ Trap efficiency is estimated with $m = 1$ since $m = 0$ is represented by Vetter's method, See Items 1 and 4 in Section 2.6.4.

See Tables C.10 to C.16 for detailed calculations.

Table C.10 Trap efficiency computation by Hazen's method, (10 °C).

Size fraction	Particle size [mm]	Fall velocity [m/s]	Trap efficiency, η [%]
1	0.5	0.059	83.84
2	0.355	0.044	79.20
3	0.125	0.010	46.51
4	0.09	0.005	32.06

Trap efficiency is calculated using Equation (2.15) with $m = 1$ since $m = 0$ is represented by Vetter's method, See Items 1 and 4 in Section 2.6.4.

Table C.11 Trap efficiency computation by Velikanov's method, (10 °C).

Size fraction	Particle size [mm]	Fall velocity [m/s]	λ	Trap efficiency, η [%]
1	0.5	0.059	4.26	98
2	0.355	0.044	3.13	98
3	0.125	0.010	0.71	80
4	0.09	0.005	0.39	70

The values for λ are calculated with Equation (2.16) and corresponding values of η are obtained from Figure 2.9.

Table C.12 Trap efficiency computation by Camp's method, (10 °C).

Size fraction	Particle size [mm]	Fall velocity [m/s]	wA_s/Q	w/u_*	Trap efficiency, η [%]
1	0.5	0.059	5.19	17.04	100
2	0.355	0.044	3.81	12.51	100
3	0.125	0.010	0.87	2.86	88
4	0.09	0.005	0.47	1.55	50

The values for η are obtained from Figure 2.10 using corresponding values of wA_s/Q and w/u_* .

Table C.13 Trap efficiency computation by Vetter's method, (10 °C).

Size fraction	Particle size [mm]	Fall velocity [m/s]	wA_s/Q	Trap efficiency, η [%]
1	0.5	0.059	5.19	99.44
2	0.355	0.044	3.81	97.78
3	0.125	0.010	0.87	58.08
4	0.09	0.005	0.47	37.62

The values for η are calculated with Equation (2.18).

Table C.14 Trap efficiency computation by Sumer's method, (10 °C).

Size fraction	Particle size [mm]	Fall velocity [m/s]	β	λ	Trap efficiency, η [%]
1	0.5	0.059	42.59	<i>Values for β are greater than 4 i.e $w/u_* > 1.6$, so this approach is not applicable for these size fractions</i>	8.17
2	0.355	0.044	31.27		
3	0.125	0.010	7.14		
4	0.09	0.005	3.87		

See Item 5 in Section 2.6.4.

Table C.15 Trap efficiency computation by Garde et al. method, (10 °C).

Size fraction	Particle size [mm]	Fall velocity [m/s]	w/u_*	η_0 [%]	k	Trap efficiency, η [%]
1	0.5	0.059	17.04	100	0.24	94.94
2	0.355	0.044	12.51	100	0.24	94.94
3	0.125	0.010	2.86	100	0.24	94.94
4	0.09	0.005	1.55	70	0.10	49.80

The values for η_0 and k are obtained from Figure 2.12 and Equation (2.20) is used to compute η .

Table C.16 Trap efficiency computation by Raju et al. method, (10 °C).

Size fraction	Particle size [mm]	Fall velocity [m/s]	w/u_*	Trap efficiency, η [%]
1	0.5	0.059	17.04	100
2	0.355	0.044	12.51	100
3	0.125	0.010	2.86	100
4	0.09	0.005	1.55	81.43

As there is no horizontal expansion, the width of approach channel, b as required in Equation (2.21) to compute η , is assumed to be the same as that of settling basin, i.e., $b = B$.

Appendix D: SSIIM Files

D.1 control file for hydraulic simulation (model scale).

```

T hydraulic simulation pow
F 1 D detailed boogie file
F 2 W run-choice
F 7 DJP double the number of grids & evoke porosity
F 15 1 wall law option
F 16 0.002 roughness
F 48 2 interpolate velocities
F 206 8 number of processors

G 1 371 77 13 1 grid and array sizes
G 3 0 10 24.25 34 40 50 60 70 75 81.25 87.5 93.75 100.0 vertical grid distribution

G 13 2 108 109 2 33 2 9 outblocking at forbay -right portion
G 13 2 110 113 30 33 2 9 outblocking middle portion of forebay wall
G 13 2 114 115 30 77 2 9 outblocking at forbay -left portion

G 13 1 108 109 2 3 10 13 piers on right side
G 13 1 108 109 10 11 10 13
G 13 1 108 109 16 17 10 13
G 13 1 108 109 22 23 10 13
G 13 1 108 109 30 31 10 13
G 13 1 114 115 36 37 10 13 piers on left side
G 13 1 114 115 42 43 10 13
G 13 1 114 115 48 49 10 13
G 13 1 114 115 54 55 10 13
G 13 1 114 115 60 61 10 13
G 13 1 114 115 66 67 10 13
G 13 1 114 115 72 73 10 13

G 13 1 136 243 12 15 2 13 outblocking 1st guidewall from right
G 13 1 136 243 26 29 2 13 outblocking 2nd guidewall from right
G 13 1 136 371 40 43 2 13 outblocking divide wall
G 13 1 136 243 54 55 2 13 outblocking 4th guidewall from right
G 13 1 136 243 66 67 2 13 outblocking 5th guidewall from right
G 13 2 244 371 12 15 2 3 outblocking 1st guidewall from right, after transition
G 13 2 244 371 26 29 2 3 outblocking 2nd guidewall from right, after transition
G 13 2 244 371 54 55 2 3 outblocking 4th guidewall from right, after transition
G 13 2 244 371 66 67 2 3 outblocking 5th guidewall from right, after transition

G 7 0 1 2 77 2 13 0 0 0.1186 1 0 0 inflow block
G 7 1 -1 2 11 10 13 0 0 0.00232 1 0 0 outflow blocks
G 7 1 -1 16 25 10 13 0 0 0.00232 1 0 0
G 7 1 -1 30 39 10 13 0 0 0.00232 1 0 0
G 7 1 -1 44 53 10 13 0 0 0.00232 1 0 0
G 7 1 -1 56 65 10 13 0 0 0.00232 1 0 0
G 7 1 -1 68 77 10 13 0 0 0.00232 1 0 0
G 7 1 2 90 93 2 4 0 0 0.05234 1 0 0 outflow block for dam spillway at right bank
G 7 1 2 96 99 2 4 0 0 0.05234 1 0 0

W 1 50 0.1186 12.95 manning-strickler no., discharge & d/s water level
W 2 19 1 10 20 30 40 50 60 70 80 90 100 106 130 138 148 162 182 242 371 initialization
W 4 2 0 2 90 93 2 4 wall redefinition at spillway
W 4 2 0 2 96 99 2 4
W 4 1 -1 371 2 77 2 9 wall redefinition at outlets
W 4 1 -1 371 12 15 10 13
W 4 1 -1 371 26 29 10 13
W 4 1 -1 371 40 43 10 13
W 4 1 -1 371 54 55 10 13
W 4 1 -1 371 66 67 10 13

K 1 60000 60000 max. number of iterations
K 2 0 1 coeff. for influence of surface/banks
K 3 0.05 0.05 0.05 0.05 0.05 0.05 relaxation coefficients
K 5 0 0 0 0 0 block-correction for each equation,1=yes
K 6 0 0 0 0 0 power-law scheme

```

F data sets

- **F 1:** Debugging option. Character *D* is used for the detailed printout to the *boogie* file and character *C* is used to print the coefficients in discretized equations.

- **F 2:** Automatic execution. The character if placed in this data set will execute the program instantly after initialization. The possible modules can be; *R*: read the result file, *W*: execute water flow computation.
- **F 7:** Run options. *D* and *J* are used to double the number of grid cells in streamwise and lateral directions, respectively, and *P* is used to evoke porosity calculation.
- **F 15:** An integer is read for the choice of algorithm for wall laws. If the integer is *1*, only the closest wall (usually the bed) will be used in case there are two walls in a cell. And if the integer is *0*, both walls will be used.
- **F 16:** Roughness coefficient used on walls and bed. If this data set is not used, the coefficient is determined from the Manning-Strickler's friction coefficient provided in *W 1* data set.
- **F 48:** Parameter for print-out of special files and result interpolation. If the integer is *0*, normal *result* file will be written. However, if the number is higher than *0*, the program will interpolate the chosen parameter value to the profile at locations mentioned in the *interpol* file and write these values in the *interres* file. The number *2* causes interpolation of velocities, *k* and ε while number *3* causes interpolation of concentrations and number *10* is used to write *Paraview.vtk* file.
- **F 206:** Maximum number of processors used for parallel computation. An integer is given, which determines the maximum number of processors. If the number provided exceeds the actual number in the computer, then all available processors will be used.

G data sets

- **G 1:** Four integers are read referring to number of grid lines in *x*, *y* and *z* directions and number of sediment sizes, respectively.
- **G 3:** Vertical distribution of grid cells.
- **G 7:** This data set defines the inflow/outflow on sides, bed or top of the geometry. It is possible to have maximum of 19 *G 7* data sets, each of which contains the inflow/outflow locations and respective discharges. The first integer describes the *type*; *0* for inflow and *1* for outflow. Next integer specifies the side; *1* for default upstream inflow cross-section, *-1* for default downstream outflow cross-section, *2* for the default right bank. After that four integers are read that determine the limits of surface. The next integer *0* refers to direction of flow normal to the surface followed by another integer *0* referring to no update. A float is then read which defines the discharge in m^3/s . Last three integers indicate direction vectors in *x*, *y* and *z* directions, respectively.
- **G 13:** Outblocking option, which is utilised to represent structure or region in geometry where flow is not possible. The maximum number of outblocks that can be used is 49 and there must be at least two free cells between two consecutive blocks. The first integer determines the sides on which the wall laws are applied. *1* for applying wall laws on the sides of the block and *2* for applying wall laws on the sides and top of the block. Six integers are then read, which define the cells of the block.

K data sets

- **K 1:** The first integer indicates the number of outer iterations for flow computation and the second integer defines the minimum number of iterations between water surface updates.

- **K 2:** Two integers are used that indicate the use of wall laws for water flow computation. If 0 , wall laws are used, and if 1 , zero-gradients are used. The first integer applies to side walls and other applies for the surface.
- **K 3:** Six integers are read referring to relaxation factors for velocities in three directions, pressure correction, k and ε equations.
- **K 5:** Block-correction. Six integers are read, each for the six water flow equations. If the integer is 1 , block-correction is used and if 0 , block-correction is avoided.
- **K 6:** Discretization scheme. Six integers are read, which represent the choice of discretization scheme for convective terms. 0 represents Power-Law (POW) scheme, while 1 indicates Second Order Upwind (SOU) scheme. And these options are limited to velocity and turbulence equations only.

W data sets

- **W 1:** Three integers define, respectively, the Manning-Strickler number, discharge and water level at downstream.
- **W 2:** This specifies the cross-sections that are utilised for initial backwater water surface calculation. First integer signifies the number of cross sections followed by number of each cross-section to be used.
- **W 4:** This sets out extra walls for multiple water flow module. One can use at most 29 walls, each defined on one $W 4$ data set. Seven integers are given for each wall. The first integer defines the plane; 1 for $j-k$ plane and 2 for $i-k$ plane. The second integer refers to which of the sides of the cell is treated as wall; 0 for deleting the previously set wall and -1 for calculating wall in the direction of increasing cell indexes. The next integer defines the node plane. And the last four integers define the 2D coordinates for the corner points of the part of the plane considered, which are similar to those given in $G 7$ data sets.

D.2 control file for hydraulic simulation (prototype scale).

```

T hydraulic simulation pow
F 1 D detailed boogie file
F 2 W run-choice
F 7 DJP double the number of grids & evoke porosity
F 11 2.65 -0.047 density and shield's coefficient
F 15 1 wall law option
F 16 0.003 roughness
F 48 2 interpolate velocities
F 206 8 number of processors

G 1 371 77 13 4 grid, array sizes & no. of size fractions
G 3 0 10 24.25 34 40 50 60 70 75 81.25 87.5 93.75 100.0 vertical grid distribution

G 13 2 108 109 2 33 2 9 outblocking at forbay -right portion
G 13 2 110 113 30 33 2 9 outblocking middle portion of forebay wall
G 13 2 114 115 30 77 2 9 outblocking at forbay -left portion

G 13 1 108 109 2 3 10 13 piers on right side
G 13 1 108 109 10 11 10 13
G 13 1 108 109 16 17 10 13
G 13 1 108 109 22 23 10 13
G 13 1 108 109 30 31 10 13
G 13 1 114 115 36 37 10 13 piers on left side
G 13 1 114 115 42 43 10 13
G 13 1 114 115 48 49 10 13
G 13 1 114 115 54 55 10 13
G 13 1 114 115 60 61 10 13
G 13 1 114 115 66 67 10 13
G 13 1 114 115 72 73 10 13

G 13 1 136 243 12 15 2 13 outblocking 1st guidewall from right
G 13 1 136 243 26 29 2 13 outblocking 2nd guidewall from right
G 13 1 136 371 40 43 2 13 outblocking divide wall
G 13 1 136 243 54 55 2 13 outblocking 4th guidewall from right
G 13 1 136 243 66 67 2 13 outblocking 5th guidewall from right
G 13 2 244 371 12 15 2 3 outblocking 1st guidewall from right, after transition
G 13 2 244 371 26 29 2 3 outblocking 2nd guidewall from right, after transition
G 13 2 244 371 54 55 2 3 outblocking 4th guidewall from right, after transition
G 13 2 244 371 66 67 2 3 outblocking 5th guidewall from right, after transition

G 7 0 1 2 77 2 13 0 0 1200 1 0 0 inflow block
G 7 1 -1 2 11 10 13 0 0 23.5 1 0 0 outflow blocks
G 7 1 -1 16 25 10 13 0 0 23.5 1 0 0
G 7 1 -1 30 39 10 13 0 0 23.5 1 0 0
G 7 1 -1 44 53 10 13 0 0 23.5 1 0 0
G 7 1 -1 56 65 10 13 0 0 23.5 1 0 0
G 7 1 -1 68 77 10 13 0 0 23.5 1 0 0
G 7 1 2 90 93 2 4 0 0 529.5 1 0 0 outflow block for dam spillway at right bank
G 7 1 2 96 99 2 4 0 0 529.5 1 0 0

W 1 50 0.1186 12.95 manning-strickler no., discharge & d/s water level
W 2 19 1 10 20 30 40 50 60 70 80 90 100 106 130 138 148 162 182 242 371 initialization
W 4 2 0 2 90 93 2 4 wall redefinition at spillway
W 4 2 0 2 96 99 2 4
W 4 1 -1 371 2 77 2 9 wall redefinition at outlets
W 4 1 -1 371 12 15 10 13
W 4 1 -1 371 26 29 10 13
W 4 1 -1 371 40 43 10 13
W 4 1 -1 371 54 55 10 13
W 4 1 -1 371 66 67 10 13

K 1 60000 60000 max. number of iterations
K 2 0 1 coeff. for influence of surface/banks
K 3 0.05 0.05 0.05 0.05 0.05 0.05 relaxation coefficients
K 5 0 0 0 0 0 block-correction for each equation,1=yes
K 6 0 0 0 0 0 power-law scheme

```

D.3 control file for sediment simulation without bed changes (prototype scale).

```

T sediment simulation pow without bed changes
F 1 D detailed boogie file
F 2 RIS run-choice
F 7 DJP double the number of grids & evoke porosity
F 11 2.65 -0.047 density and shield's coefficient
F 15 1 wall law option
F 16 0.003 roughness
F 33 100 10 time-step, inner iteration
F 37 2 transient sediment computation
F 48 10 write paraview file
F 68 2 no recomputation of velocity field
F 206 8 number of processors

G 1 371 77 13 4 grid, array sizes & no. of size fractions
G 3 0 10 24.25 34 40 50 60 70 75 81.25 87.5 93.75 100.0 vertical grid distribution

G 13 2 108 109 2 33 2 9 outblocking at forbay -right portion
G 13 2 110 113 30 33 2 9 outblocking middle portion of forebay wall
G 13 2 114 115 30 77 2 9 outblocking at forbay -left portion

G 13 1 108 109 2 3 10 13 piers on right side
G 13 1 108 109 10 11 10 13
G 13 1 108 109 16 17 10 13
G 13 1 108 109 22 23 10 13
G 13 1 108 109 30 31 10 13
G 13 1 114 115 36 37 10 13 piers on left side
G 13 1 114 115 42 43 10 13
G 13 1 114 115 48 49 10 13
G 13 1 114 115 54 55 10 13
G 13 1 114 115 60 61 10 13
G 13 1 114 115 66 67 10 13
G 13 1 114 115 72 73 10 13

G 13 1 136 243 12 15 2 13 outblocking 1st guidewall from right
G 13 1 136 243 26 29 2 13 outblocking 2nd guidewall from right
G 13 1 136 371 40 43 2 13 outblocking divide wall
G 13 1 136 243 54 55 2 13 outblocking 4th guidewall from right
G 13 1 136 243 66 67 2 13 outblocking 5th guidewall from right
G 13 2 244 371 12 15 2 3 outblocking 1st guidewall from right, after transition
G 13 2 244 371 26 29 2 3 outblocking 2nd guidewall from right, after transition
G 13 2 244 371 54 55 2 3 outblocking 4th guidewall from right, after transition
G 13 2 244 371 66 67 2 3 outblocking 5th guidewall from right, after transition

G 7 0 1 2 77 2 13 0 0 1200 1 0 0 inflow block
G 7 1 -1 2 11 10 13 0 0 23.5 1 0 0 outflow blocks
G 7 1 -1 16 25 10 13 0 0 23.5 1 0 0
G 7 1 -1 30 39 10 13 0 0 23.5 1 0 0
G 7 1 -1 44 53 10 13 0 0 23.5 1 0 0
G 7 1 -1 56 65 10 13 0 0 23.5 1 0 0
G 7 1 -1 68 77 10 13 0 0 23.5 1 0 0
G 7 1 2 90 93 2 4 0 0 529.5 1 0 0 outflow block for dam spillway at right bank
G 7 1 2 96 99 2 4 0 0 529.5 1 0 0

G 21 1 132 2 77 2 13 sediment fluxes at settling basin inlet
G 21 1 371 2 77 10 13 sediment fluxes at settling basin outlet
G 24 6 D 0 0 m 0 0 z 0 0 v 0 0 s 0 0 U 0 0 variables for paraview files

S 1 0.0005 0.062 size fraction number, size, fall velocity
S 2 0.000355 0.047
S 3 0.000125 0.012
S 4 0.00009 0.007
N 0 1 0.027 sediment sample
N 0 2 0.050
N 0 3 0.553
N 0 4 0.370
B 0 0 0 0 0 distribution of sediment groups

W 1 50 1200 518 manning-strickler no., discharge & d/s water level
W 2 19 1 10 20 30 40 50 60 70 80 90 100 106 130 138 148 162 182 242 371 initialization
W 4 2 0 2 90 93 2 4 wall redefinition at spillway
W 4 2 0 2 96 99 2 4
W 4 1 -1 371 2 77 2 9 wall redefinition at outlets
W 4 1 -1 371 12 15 10 13
W 4 1 -1 371 26 29 10 13
W 4 1 -1 371 40 43 10 13
W 4 1 -1 371 54 55 10 13
W 4 1 -1 371 66 67 10 13

K 1 864 60000 max. number of iterations
K 2 0 1 coeff. for influence of surface/banks
K 3 0.05 0.05 0.05 0.05 0.05 0.05 relaxation coefficients
K 5 0 0 0 0 0 0 block-correction for each equation, 1=yes
K 6 0 0 0 0 0 0 power-law scheme

```

D.4 control file for sediment simulation with bed changes (prototype scale).

```

T sediment simulation pow with bed changes
F 1 D detailed boogie file
F 2 IS run-choice
F 7 DJP double the number of grids & evoke porosity
F 11 2.65 -0.047 density and shield's coefficient
F 15 1 wall law option
F 16 0.003 roughness
F 33 30 100 time-step, inner iteration
F 37 2 transient sediment computation
F 48 10 write paraview file
F 68 0 recomputation of velocity field after update of the bed
F 206 8 number of processors

G 1 371 77 13 4 grid, array sizes & no. of size fractions
G 3 0 10 24.25 34 40 50 60 70 75 81.25 87.5 93.75 100.0 vertical grid distribution

G 13 2 108 109 2 33 2 9 outblocking at forbay -right portion
G 13 2 110 113 30 33 2 9 outblocking middle portion of forebay wall
G 13 2 114 115 30 77 2 9 outblocking at forbay -left portion

G 13 1 108 109 2 3 10 13 piers on right side
G 13 1 108 109 10 11 10 13
G 13 1 108 109 16 17 10 13
G 13 1 108 109 22 23 10 13
G 13 1 108 109 30 31 10 13
G 13 1 114 115 36 37 10 13 piers on left side
G 13 1 114 115 42 43 10 13
G 13 1 114 115 48 49 10 13
G 13 1 114 115 54 55 10 13
G 13 1 114 115 60 61 10 13
G 13 1 114 115 66 67 10 13
G 13 1 114 115 72 73 10 13

G 13 1 136 243 12 15 2 13 outblocking 1st guidewall from right
G 13 1 136 243 26 29 2 13 outblocking 2nd guidewall from right
G 13 1 136 371 40 43 2 13 outblocking divide wall
G 13 1 136 243 54 55 2 13 outblocking 4th guidewall from right
G 13 1 136 243 66 67 2 13 outblocking 5th guidewall from right
G 13 2 244 371 12 15 2 3 outblocking 1st guidewall from right, after transition
G 13 2 244 371 26 29 2 3 outblocking 2nd guidewall from right, after transition
G 13 2 244 371 54 55 2 3 outblocking 4th guidewall from right, after transition
G 13 2 244 371 66 67 2 3 outblocking 5th guidewall from right, after transition

G 7 0 1 2 77 2 13 0 0 1200 1 0 0 inflow block
G 7 1 -1 2 11 10 13 0 0 23.5 1 0 0 outflow blocks
G 7 1 -1 16 25 10 13 0 0 23.5 1 0 0
G 7 1 -1 30 39 10 13 0 0 23.5 1 0 0
G 7 1 -1 44 53 10 13 0 0 23.5 1 0 0
G 7 1 -1 56 65 10 13 0 0 23.5 1 0 0
G 7 1 -1 68 77 10 13 0 0 23.5 1 0 0
G 7 1 2 90 93 2 4 0 0 529.5 1 0 0 outflow block for dam spillway at right bank
G 7 1 2 96 99 2 4 0 0 529.5 1 0 0

G 21 1 132 2 77 2 13 sediment fluxes at settling basin inlet
G 21 1 371 2 77 10 13 sediment fluxes at settling basin outlet
G 24 6 D 0 0 m 0 0 z 0 0 v 0 0 s 0 0 U 0 0 variables for paraview files
P 10 120 number of global iterations between printing results
for time-dependent computations
size fraction number, size, fall velocity

S 1 0.0005 0.062
S 2 0.000355 0.047
S 3 0.000125 0.012
S 4 0.00009 0.007

N 0 1 0.027 sediment sample
N 0 2 0.050
N 0 3 0.553
N 0 4 0.370

B 0 0 0 0 distribution of sediment groups

W 1 50 1200 518 manning-strickler no., discharge & d/s water level
W 2 19 1 10 20 30 40 50 60 70 80 90 100 106 130 138 148 162 182 242 371 initialization
W 4 2 0 2 90 93 2 4 wall redefinition at spillway
W 4 2 0 2 96 99 2 4
W 4 1 -1 371 2 77 2 9 wall redefinition at outlets
W 4 1 -1 371 12 15 10 13
W 4 1 -1 371 26 29 10 13
W 4 1 -1 371 40 43 10 13
W 4 1 -1 371 54 55 10 13
W 4 1 -1 371 66 67 10 13

K 1 2880 60000 max. number of iterations
K 2 0 1 coeff. for influence of surface/banks
K 3 0.05 0.05 0.05 0.05 0.05 0.05 relaxation coefficients
K 5 0 0 0 0 0 block-correction for each equation,1=yes
K 6 0 0 0 0 0 power-law scheme

```

Additional data sets used in sediment simulation:

F data sets

- **F 2:** Automatic execution. The character if placed in this data set will execute the program instantly after initialization. The possible modules can be; *R*: read the *result* file, *I*: initialize sediment concentration computation, *S*: compute sediment concentration.
- **F 11:** Two integers are read defining density of sediment and Shield's coefficient, respectively. If a negative Shield's coefficient is provided, the software computes it according to the parameterization of the original curve.
- **F 33:** The data set evokes the transient water flow parameters. The first float defines the time-step in seconds and the integer after, defines the number of inner iteration for each time-step. The time-step was set to 100*seconds* for simulation without bed changes, while for the simulation with bed changes time-step was set to 30*seconds*.
- **F 37:** Transient Sediment Computation (TSC). The data set activates the time-dependent computation for sediment transport. The integer 2 refers to use of sediment concentration formula for entrainment rate in the bed cells.
- **F 68:** Parameter for choice of water flow computation. An integer is read; if 2, TSC will not recompute the water flow field after an update of the bed which means quasi-steady state is modelled, and if 0, water flow field is recomputed after the update of the bed.

G data sets

- **G 21:** The data set is used to determine fluxes through special parts in the geometry, in addition to the four sides of the geometry. Six integers are read. The first integer indicates whether the surface is a cross-section (1) or a longitudinal section (2) or a horizontal section (3). The second integer refers to section number and the last four integers define the surface.
- **G 24:** The data set determines the variables to be written to the *Paraview* file. The first integer specifies the number of variables on the data set. Then a character and two integers are read for each variable. The character indicates the the variable; *D*: Depth-averaged horizontal velocity, *m*: Bed shear stress, *z*: Bed level, *v*: Water level, *s*: Bed movement, *U*: Bed changes. The following first integer defines the level above the bed and second integer defines the sediment size.

P 10 data set: An integer is read that defines the number of global iterations between printing the *result* file for time-dependent computations.

S data set: The data set defines the size and fall velocity of the sediments. The first integer denotes the size group followed by diameter in *m* and and fall velocity in *m/s*. The coarsest sediment size should be number 1 and the finer sizes should be provided higher numbers.

N data set: The data set consists of size fractions of different sediment groups. The first integer signifies the group index; 0 for the first group. The second integer indicates the sediment size followed by a float defining the corresponding fraction of size in the group.

B data set: The data set defines the distribution of different sediment groups to the different locations in the geometry. Five integers are read; the first integer defines the index for the group, the second and third integers describe the cell numbers in streamwise direction, while the last two integers describe the cell numbers in lateral direction. The integers were set to zero due to lack of information on sediment distribution as *B 0 0 0 0 0*, which indicates that the group is distributed in all the cells.

D.5 koordina file (model scale).

1	1	4.275	4.901	12.938
1	2	4.349	4.941	12.922
1	3	4.443	4.991	12.918
1	4	4.536	5.040	12.925
1	5	4.610	5.080	12.925
1	6	4.704	5.130	12.925
1	7	4.797	5.179	12.925
1	8	4.872	5.219	12.911
1	9	4.965	5.269	12.891
1	10	5.058	5.318	12.889
1	11	5.133	5.358	12.888
1	12	5.208	5.398	12.887
1	13	5.282	5.438	12.886
1	14	5.357	5.477	12.884
1	15	5.432	5.517	12.883
1	16	5.469	5.537	12.882
1	17	5.506	5.557	12.881
1	18	5.544	5.577	12.881
1	19	5.581	5.596	12.880
1	20	5.618	5.616	12.879
.
.
.
.
.
.
.
.
.
186	30	13.924	4.694	12.600
186	31	13.924	4.752	12.600
186	32	13.924	4.809	12.600
186	33	13.924	4.867	12.600
186	34	13.924	4.894	12.600
186	35	13.924	4.950	12.600
186	36	13.924	5.006	12.600
186	37	13.924	5.061	12.600
186	38	13.924	5.117	12.600
186	39	13.924	5.175	12.600

D.6 koordina file (prototype scale).

1	1	170.980	196.048	517.500
1	2	173.964	197.640	516.885
1	3	177.700	199.624	516.702
1	4	181.432	201.612	517.000
1	5	184.416	203.200	517.000
1	6	188.152	205.188	517.000
1	7	191.884	207.172	517.000
1	8	194.872	208.764	516.445
1	9	198.604	210.748	515.637
1	10	202.336	212.736	515.561
1	11	205.324	214.324	515.517
1	12	208.308	215.912	515.474
1	13	211.296	217.500	515.420
1	14	214.284	219.092	515.363
1	15	217.268	220.680	515.305
1	16	218.764	221.476	515.277
1	17	220.256	222.268	515.249
1	18	221.748	223.064	515.221
1	19	223.240	223.856	515.194
1	20	224.736	224.652	515.169
.
.
.
.
.
.
.
.
.
186	30	556.956	187.768	504.00
186	31	556.956	190.068	504.00
186	32	556.956	192.368	504.00
186	33	556.956	194.668	504.00
186	34	556.956	195.772	504.00
186	35	556.956	198.000	504.00
186	36	556.956	200.224	504.00
186	37	556.956	202.452	504.00
186	38	556.956	204.680	504.00
186	39	556.956	206.980	504.00

D.7 interpol file (model scale).

M	9.2369	3.4631
M	9.2369	3.7781
M	9.2369	4.0931
M	9.2369	4.4081
M	9.2369	4.7231
M	9.2369	5.0381
M	10.3962	3.5036
M	10.3962	3.7755
M	10.3962	4.0880
M	10.3962	4.4130
M	10.3962	4.7255
M	10.3962	4.9974
M	10.8962	3.5036
M	10.8962	3.7755
M	10.8962	4.0880
M	10.8962	4.4130
M	10.8962	4.7255
M	10.8962	4.9974
M	11.6462	3.5036
M	11.6462	3.7755
M	11.6462	4.0880
M	11.6462	4.4130
M	11.6462	4.7255
M	11.6462	4.9974
M	12.6462	3.5036
M	12.6462	3.7755
M	12.6462	4.0880
M	12.6462	4.4130
M	12.6462	4.7255
M	12.6462	4.9974
M	13.1462	3.5036
M	13.1462	3.7755
M	13.1462	4.0880
M	13.1462	4.4130
M	13.1462	4.7255
M	13.1462	4.9974
M	13.5212	3.5036
M	13.5212	3.7755
M	13.5212	4.0880
M	13.5212	4.4130
M	13.5212	4.7255
M	13.5212	4.9974

D.8 interpol file (prototype scale).

M	369.476	138.524
M	369.476	151.124
M	369.476	163.724
M	369.476	176.324
M	369.476	188.924
M	369.476	201.524
M	415.848	140.144
M	415.848	151.02
M	415.848	163.52
M	415.848	176.52
M	415.848	189.02
M	415.848	199.896
M	435.848	140.144
M	435.848	151.02
M	435.848	163.52
M	435.848	176.52
M	435.848	189.02
M	435.848	199.896
M	465.848	140.144
M	465.848	151.02
M	465.848	163.52
M	465.848	176.52
M	465.848	189.02
M	465.848	199.896
M	505.848	140.144
M	505.848	151.02
M	505.848	163.52
M	505.848	176.52
M	505.848	189.02
M	505.848	199.896
M	525.848	140.144
M	525.848	151.02
M	525.848	163.52
M	525.848	176.52
M	525.848	189.02
M	525.848	199.896
M	540.848	140.144
M	540.848	151.02
M	540.848	163.52
M	540.848	176.52
M	540.848	189.02
M	540.848	199.896

the variables are unknown so that program computes the value. The four floats at the end indicate the inflowing sediment concentration (volume fraction) for each size fraction specified in S data set.

D.12 koomin file for sediment simulation (prototype scale).

```
1 1 170.980 196.048 517.499
1 2 173.964 197.640 516.884
1 3 177.700 199.624 516.701
1 4 181.432 201.612 516.999
1 5 184.416 203.200 516.999
1 6 188.152 205.188 516.999
1 7 191.884 207.172 516.999
1 8 194.872 208.764 516.444
1 9 198.604 210.748 515.636
1 10 202.336 212.736 515.560
1 11 205.324 214.324 515.516
1 12 208.308 215.912 515.473
1 13 211.296 217.500 515.419
1 14 214.284 219.092 515.362
1 15 217.268 220.680 515.304
1 16 218.764 221.476 515.276
1 17 220.256 222.268 515.248
1 18 221.748 223.064 515.220
1 19 223.240 223.856 515.193
1 20 224.736 224.652 515.168
. . . . .
. . . . .
. . . . .
. . . . .
. . . . .
186 30 556.956 187.768 503.999
186 31 556.956 190.068 503.999
186 32 556.956 192.368 503.999
186 33 556.956 194.668 503.999
186 34 556.956 195.772 503.999
186 35 556.956 198.000 503.999
186 36 556.956 200.224 503.999
186 37 556.956 202.452 503.999
186 38 556.956 204.680 503.999
186 39 556.956 206.980 503.999
```

Appendix E: Additional Figures

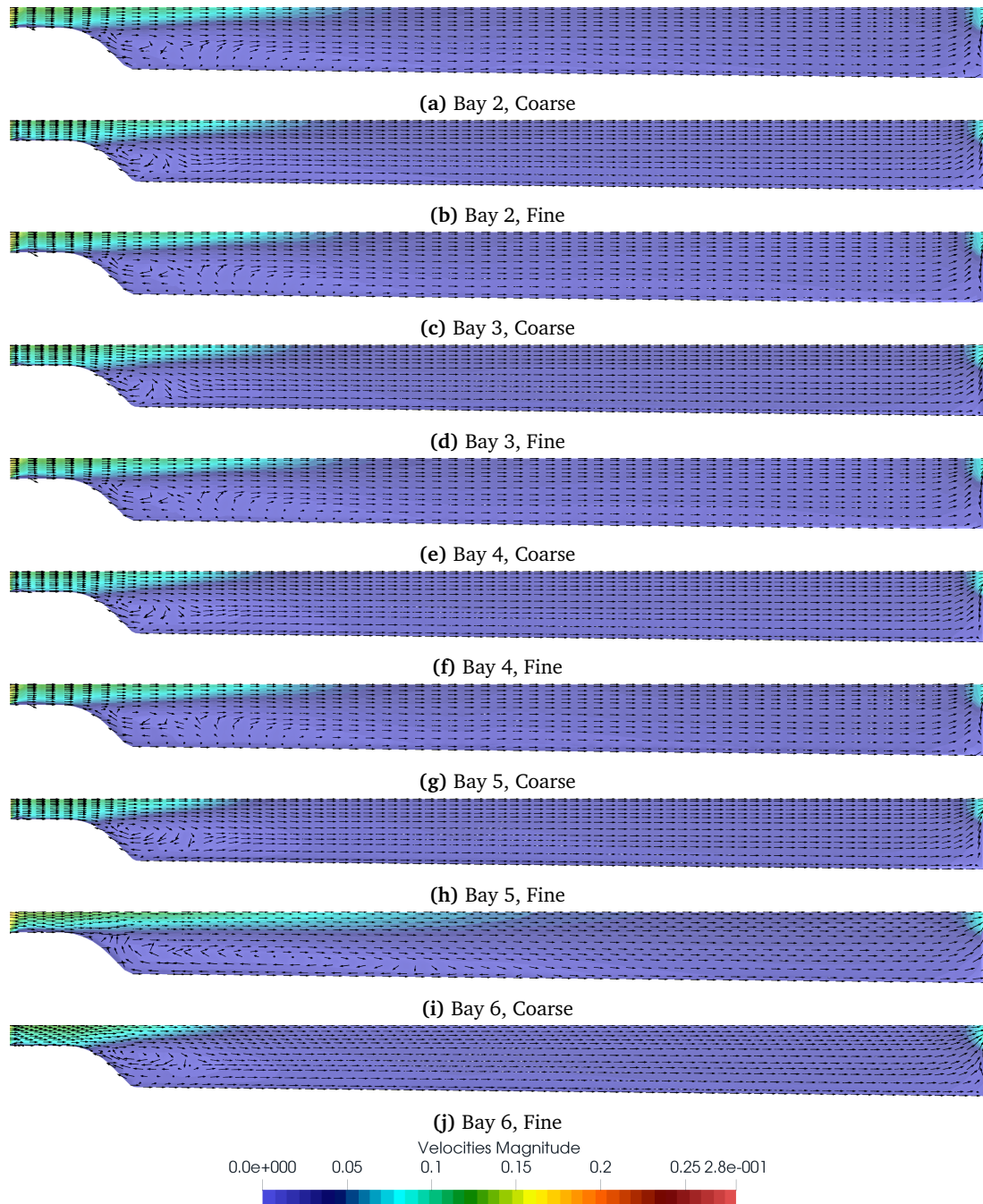


Figure E.1: Longitudinal profiles with velocity vectors along different bays for simulation with POW scheme and different grid resolutions, (model scale). The velocity vectors represent only the direction of velocities not the magnitude.

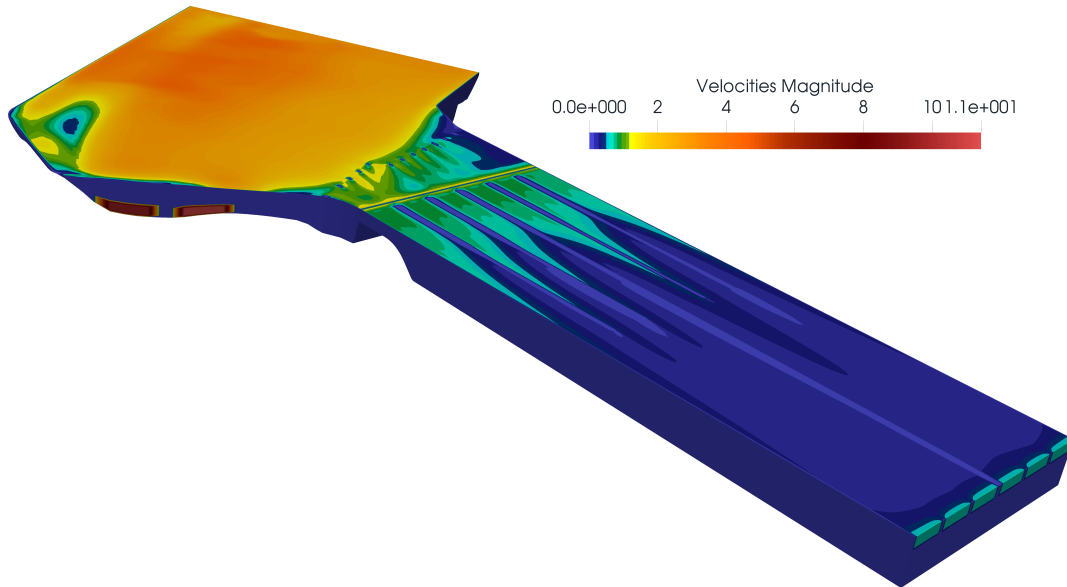


Figure E.2: Simulated flow field with POW scheme and fine grid resolution, (prototype scale) showing outlets at spillway and settling basin.

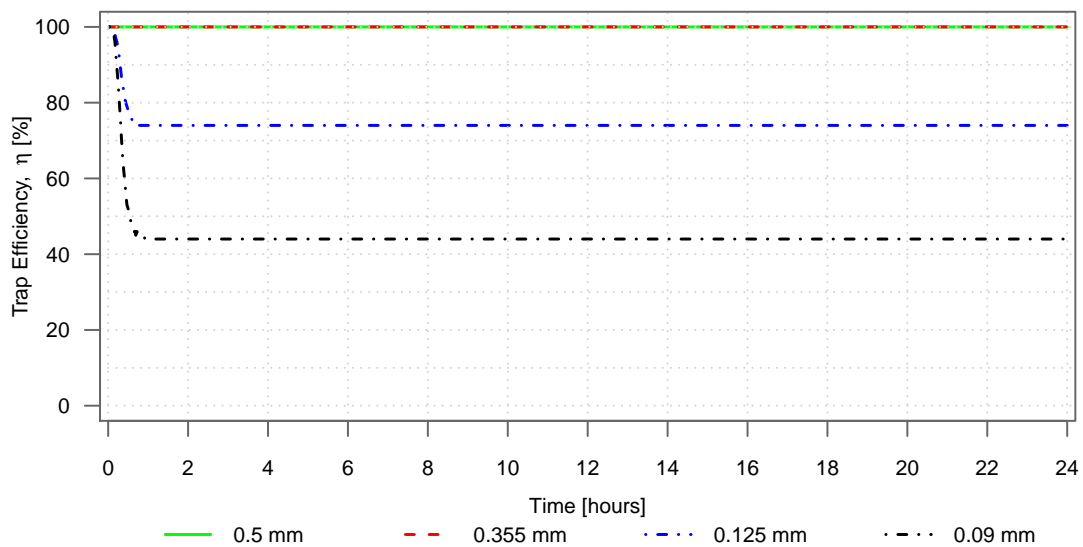


Figure E.3: Trap efficiencies for each size fraction with respect to the time of computation for simulation without bed changes and water temperature at 10°C.

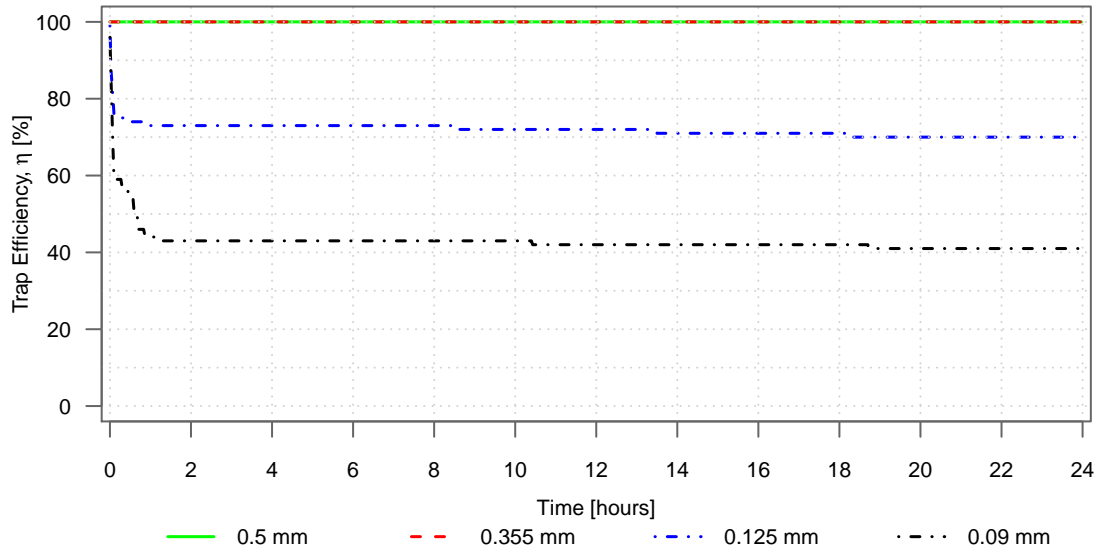


Figure E.4: Trap efficiencies for each size fraction with respect to the time of computation for simulation with bed changes and water temperature at 10 °C.

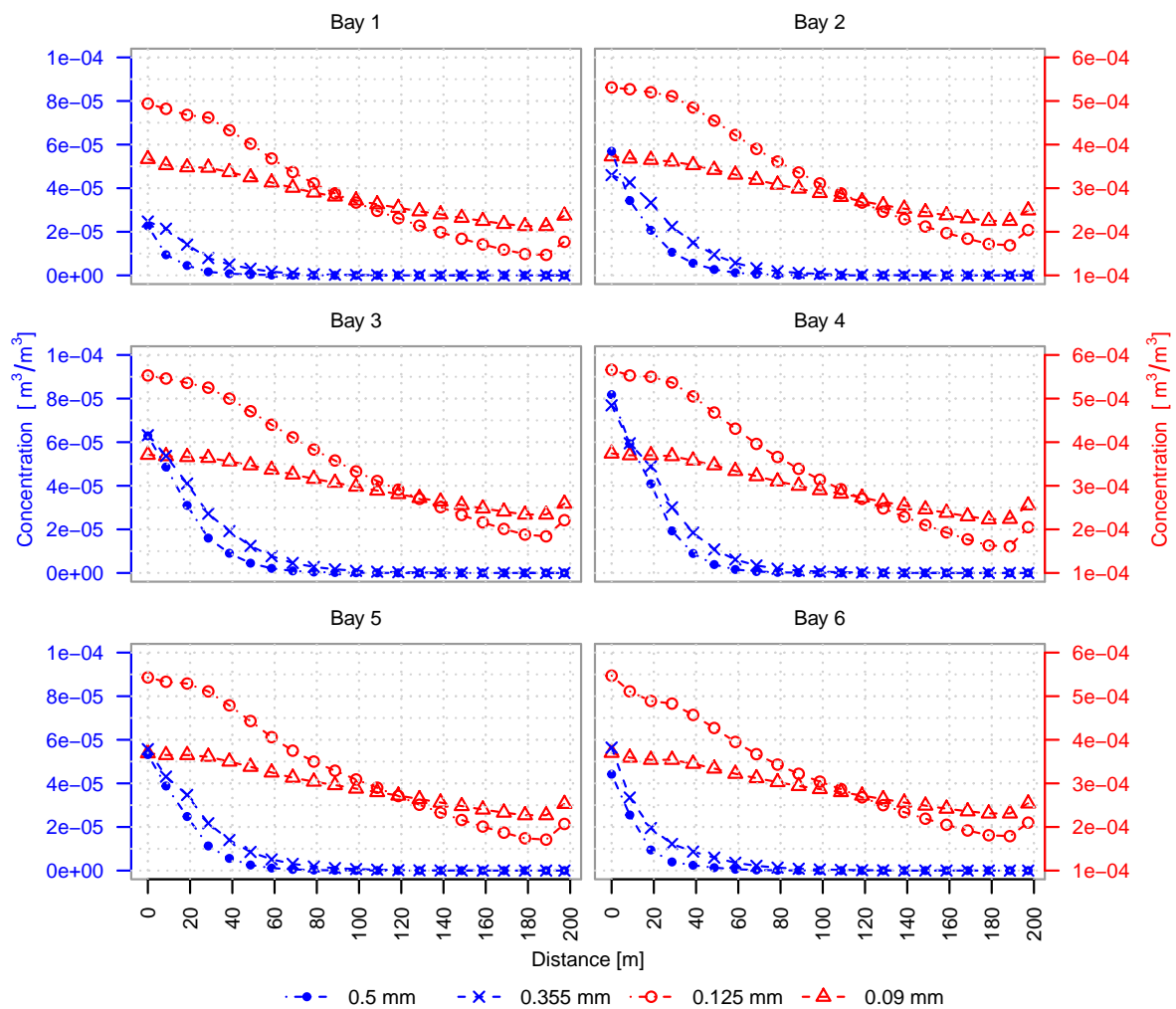


Figure E.5: Computed depth-averaged concentration for each size fraction along the mid-way of each bay from intake to basin outlet for water temperature at 10 °C.

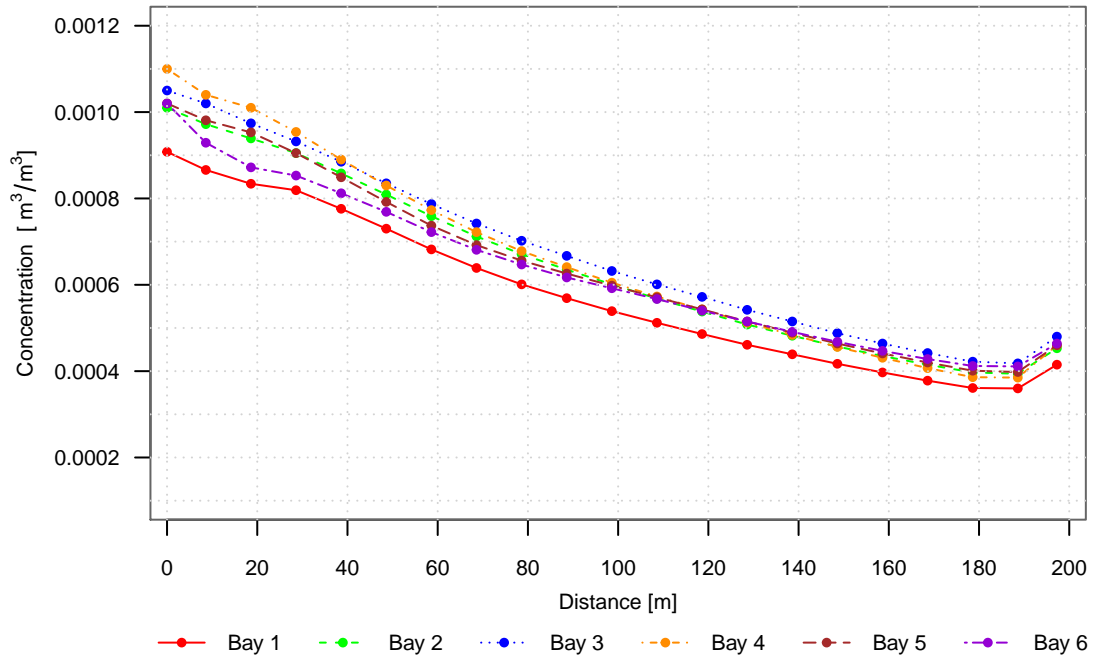


Figure E.6: Computed sum of depth-averaged concentration along the mid-way of each bay from intake to basin outlet for water temperature at 10°C .

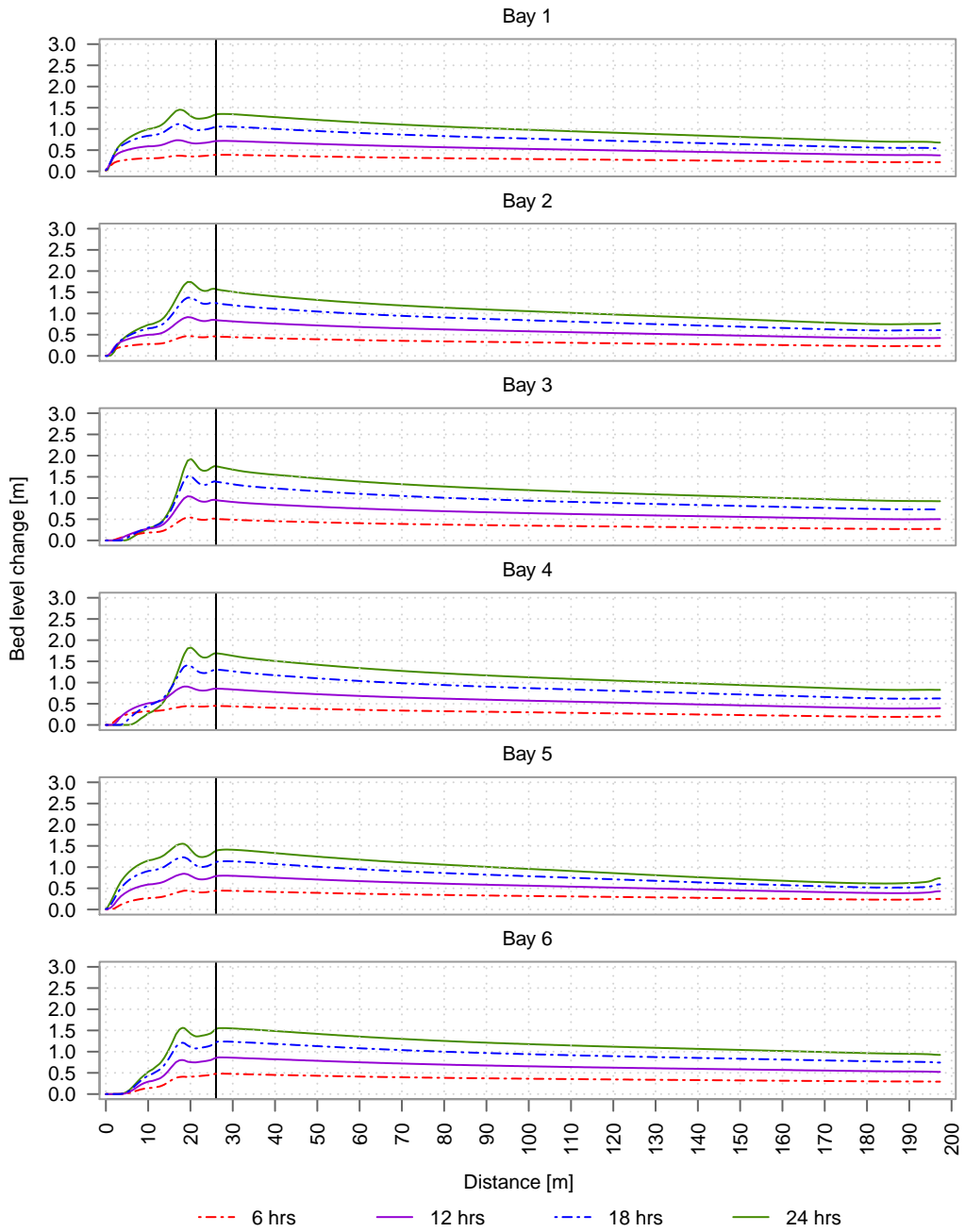


Figure E.7: Computed bed level changes along the mid-way in each bay at an interval of 6 hours for simulation with water temperature at 10°C. The distances are taken with reference to the intake indicated by 0 and the vertical line between 20 and 30 represents the end of the inlet transition.

Appendix F: Agreement

Master`s Agreement

Faculty	IV - Fakultet for ingeniørvitenskap
Institute	Institutt for bygg- og miljøteknikk
Programme code	MSB1
Course code	194_TVM4915_1

Personal information	
Family name, first name	Shrestha, Sanjaya Dhonju
Date of birth	02.05.1990
Email address	sanjayas@stud.ntnu.no

The Master`s thesis	
Starting date	15.01.2020
Submission deadline	11.06.2020
Thesis working title	Numerical Modelling of Hydraulics and Sediment at the Headworks of Kali Gandaki A Hydropower Plant, Nepal
Thematic description	<p>1. Background The 144 MW Kali Gandaki A Hydropower Plant (KGA), owned and operated by Nepal Electricity Authority (NEA), is a Peaking Run-of-River type project located in Western Nepal. The headworks has been facing problems related to unfavorable hydraulics at intake and settling basins and frequent choking of intake trashrack. Recirculation flows are observed in both sides of the forebay. Also, flow is not evenly distributed in the intake. The effect of concentrated approach flow, due to very short transition between intake and settling basin, extends even inside the settling basins creating recirculation flow and formation of eddies, which are unfavorable to settle suspended sediments. Pertaining to uneven distribution of flow into the settling basins, the recirculating flow and formation of eddies, settling basins are not performing at their best. These have caused excessive sediment induced turbine erosion far more than expected. With an intention to improve the overall headworks hydraulic performance along with the flow patterns in settling basins, a physical hydraulic model was built at 1:40 scale and tested at Hydro Lab, Nepal. The study was primarily focused on hydraulics within and nearby the intake area to achieve a satisfactory performance in terms of improved approach flow and flow distribution at intakes, handling of floating debris, flow patterns at inlet, main basin and outlet of the settling basins through modifications to existing headworks arrangement. The study has recommended design modifications based on hydraulic performance and qualitative flushing test with sediments. However, the performance</p>

	<p>improvement in terms of suspended sediment handling is still unknown. This study will investigate the performance of the headworks with the proposed modification from physical hydraulic modelling with respect to suspended sediments. The modelling of sediments will be performed numerically. The general work plan will be to validate the numerical model against the physical model in terms of hydraulics in model scale and then carry out study regarding suspended sediments to test the performance of modified structure in prototype scale.</p> <p>2. Work description The thesis shall cover, though not necessarily be limited to the main tasks listed below. The candidate must collect available documents such as reports, relevant studies and maps. Based on the available documentation the following shall be carried out:</p> <ol style="list-style-type: none"> 1 Literature review of sediment handling techniques at the headworks of Run-of-River hydropower project and numerical modelling of suspended sediments 2 Numerical modelling of hydraulics at the intake and settling basin in model scale 3 Numerical modelling of hydraulics and fine suspended sediment transport at the intake and settling basin in prototype scale 4 Discussion of the results 5 Conclusions 6 Proposal for future work 7 Presentation of the work <p>The literature review should outline the previous contributions in condensed manner and result in the motivation for the current study.</p>
--	---

Supervision and co-authors	
Supervisor	Nils Ruther
Any co-supervisors	Diwash Lal Maskey, Siri Stokseth
Any co-authors	

Topics to be included in the Master`s Degree (if applicable)				
Course code	Course name	Credits	Level	Term

Guidelines – Rights and Obligations

Purpose

Agreement on supervision of the Master's thesis is a cooperation agreement between the student, supervisor and the department that governs the relationship of supervision, scope, nature and responsibilities.

The master's program and the work of the master's thesis are regulated by the Act relating to universities and university colleges, NTNU's study regulations and current curriculum for the master's program.

Supervision

The student is responsible for

- Agree upon supervision within the framework of the agreement
- Set up a plan of progress for the work in cooperation with the supervisor, including the plan for when the guidance should take place
- Keep track of the number of hours spent with the supervisor
- Provide the supervisor with the necessary written material in a timely manner before the guidance
- Keep the institute and supervisor informed of any delays

The supervisor is responsible for

- Explain expectations of the guidance and how the guidance should take place
- Ensure that any necessary approvals are requested (REC, ethics, privacy)
- Provide advice on the formulation and demarcation of the topic and issue so that the work is feasible within the standard or agreed upon study time
- Discuss and evaluate hypotheses and methods
- Advice on professional literature, source material / data base / documentation and potential resource requirements
- Discuss the presentation (disposition, linguistic form, etc.)
- Discuss the results and the interpretation of them
- Stay informed about the progression of the student's work according to the agreed time and work plan, and follow up the student as needed
- Together with the student, keep an overview of the number of hours spent

The institute is responsible for

- Make sure that the agreement is entered into
- Find and appoint supervisor(-s)
- Enter into an agreement with another department / faculty / institution if there is a designated external supervisor
- In cooperation with the supervisor, keep an overview of the student's progress, an overview of the number of hours spent, and follow up if the student is delayed by appointment
- Appoint a new supervisor and arrange for a new agreement if
 - supervisor will be absent due to research term, illness, travel, etc., and if the student wishes
 - student or supervisor requests to terminate the agreement because one of the parties does not follow it
 - other circumstances make the parties find it appropriate with a new supervisor
- Notify the student when the guidance relationship expires.
- Inform supervisors about the responsibility for safeguarding ethical issues, privacy and guidance ethics
- Should the cooperation between student and supervisor become problematic for one of the parties, a student or supervisor may ask to be freed from the Master's agreement. In such case, the institute must appoint a new supervisor

This Master`s agreement must be signed when the guidelines have been reviewed.

Approved by

Sanjaya Dhonju Shrestha
Student

15.01.2020
place and date

Nils Ruther
Supervisor

15.01.2020
place and date

Carine Louise Nilsen
Institute

06.02.2020
place and date

